OPTO-ELECTRONICS REVIEW 8(3), 201–239 (2000)

III-Nitride wide bandgap semiconductors: a survey of the current status and future trends of the material and device technology

P. KUNG and M. RAZEGHI*

Center for Quantum Devices Department of Electrical and Computer Engineering
Northwestern University, Evanston, IL 60208, USA

During the past decade, group III-Nitride wide bandgap semiconductors have become the focus of extremely intensive reearch because of their exceptional physical properties and their high potential for use in countless numbers of applications. Nearly all aspects have been investigated, from the fundamental physical understanding of these materials to the development of the fabrication technology and demonstration of commercial devices. The purpose of this paper is to review the physical properties of III-Nitrides, their areas of application, the current status of the material technology (AlN, AlGaN, GaN, GaInN) including synthesis and processing. The state-of-the-art of III-Nitride material quality, as well as the devices which have been demonstrated, including electronic devices, $Al_xGa_{1-x}N$ ultraviolet photoconductors, ultraviolet photodiodes, visible light emitting diodes (LEDs) and ultraviolet-blue laser diodes, will also be presented.

Keywords: III-Nitrides, AlN, GaN, $Al_xGa_{1-x}N$, $Ga_{1-x}In_xN$, visible, ultraviolet, violet, blue, green, heterostructures, n-type doping, p-type, doping, etching, metal contacts, electronic devices, photodetectors, light emitting diodes, laser diodes.

1. Introduction

Aluminium nitride (AlN), gallium nitride (GaN), indium nitride (InN) and their alloys are commonly known as "III-Nitride materials" or "III-Nitrides". These materials have exceptional physical properties, chiefly their wide energy bandgap, which make them the ideal building blocks for numerous optical and electronic devices to be used in many applications. The III-Nitrides have existed for many years: AlN was synthesised by 1907 [1], InN by 1910 [2], and GaN by 1932 [3]. However, because the material was polycrystalline, it was not useful for semiconductor devices. Only limited research had been conducted on III-Nitrides until the 1980-1990's when two major breakthroughs led to renewed interest in III-Nitrides: the development of a buffer layer technique to obtain smooth and non-polycrystalline films and the demonstration of p-type doping. This opened the door to the control of the material structural, electrical and optical quality. Now, research in III-Nitrides has become a field of its own, whereas it used to be part of the "wide bandgap semiconductor" field, and commercial devices have become availble.

This paper will first review the physical properties of III-Nitride materials, followed by a non-exhaustive description of the areas of applications. Technological details will then be discussed, including the material growth and the substrates used. The current state-of-the-art in III-Nitride thin films and heterostructures will be presented. The technology for the material processing will also be reviewed, including etching and metal contacts. Finally, the state-of-the-art for III-Nitride based devices will be presented, including electronic devices, ultraviolet photodetectors, visible light emitting diodes (LEDs) and ultraviolet-blue laser diodes.

2. Physical properties of III-Nitride materials

Unlike more conventional semiconductors, such as silicon (Si) or gallium arsenide (GaAs) which have a diamond or zinc-blende structure with a cubic symmetry, III-Nitride crystals are wurtzite in their stable form with a hexagonal symmetry, belonging to the point group 6mm. III-Nitrides are thus polar crystals because they do not have a centre of symmetry [4]. They thus possess many other potentially useful properties such as piezoelectricity, pyroelectricity [5] and second harmonic generation [6,7]. The large difference in electronegativity between the group III and group V elements (Al = 1.18, Ga = 1.13, In = 0.99, N = 3.0) results in very strong chemical bonds in the III-Nitride material system, which are at the origin of most of the interesting III-Nitride physical properties.

A direct result of this is the wide bandgap. III-Nitrides have a bandgap energy ranging from 6.2 to 1.9 eV, corresponding to a wavelength from 200 to 650 nm. This spectral range covers the visible spectrum (blue, green, yellow and red) as well as the near ultraviolet region in which the

*e-mail: razeghi@ece.nwu.edu

atmosphere transmits, as shown in Fig. 1. The bandgap is direct, which is most appropriate for optical devices. Because the intrinsic carrier concentration is an exponential function of the energy gap and the temperature, a wider bandgap semiconductor has much lower intrinsic carrier concentrations over a large temperature range

$$n_i(cm^{-3}) = 4.9\times10^{15}\left(\frac{m_{de}m_{dh}}{m_0^2}\right)^{3/4} T^{3/2}e^{-E_g/2kT},$$

where all the parameters have conventional meaning. This results in lower leakage and dark currents in devices, which is especially important in photodetectors and high temperature electronics. Another consequence of the strong chemical bonding is the physical (high melting points, mechanical strength) and chemical stability of these materials. These also enjoy high thermal conductivity. Their effective masses are higher than conventional semiconductors, thus leading to lower carrier mobilities, but this is made up for by the high saturated electron drift velocities predicted for this material system. The refractive indices of III-Nitrides are lower compared to narrower gap semiconductors, which results in a lower reflectivity at the interface. This is an advantage for photodetector efficiency, but a disadvantage when trying to achieve lasers with low threshold currents.

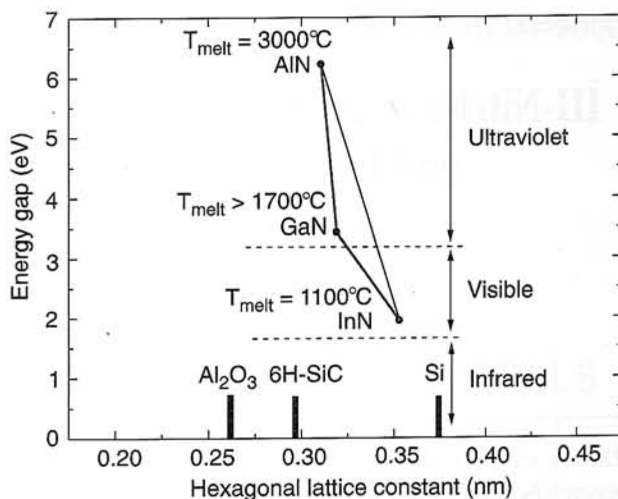

Fig. 1. Energy gap versus hexagonal lattice constant for III-Nitride and selected substrate materials.

All these properties yields III-Nitrides a very high potential for operation in the visible-to-ultraviolet spectral region as well as in harsh environments (radiation, heat) such as those typical of space applications, high frequency, high power and high temperature electronics. Details of the physical properties of III-Nitrides are summarised in Table 1.

Although III-Nitride based devices are being rapidly demonstrated and commercialised, there are many barriers that must be overcome before the full potential of these materials can be realised as reliable devices. First,

Table 1. Physical properties of III-Nitrides (from Refs. 8, 9, except[a] from Ref. 10).

	GaN	AlN	InN
Room temperature energy gap (eV)	3.34	6.2	1.9
Lattice constant, a (Å)	3.189[a]	3.112	3.545
Lattice constant, c (Å)	5.186[a]	4.982	5.703
Thermal expansion coefficient, α_a (10^{-6} K^{-1})	4.3(17–477°C)[a]	5.27(20–800°C)	5.6(280°C)
Thermal expansion coefficient, α_c (10^{-6} K^{-1})	4.0(17–477°C)[a]	4.15(20–800°C)	3.8(280°C)
Electron effective mass, m_e (m_0)	0.2		0.11
Hole effective mass, m_h (m_0)	0.8		0.5 (m_{hh}, calculated) 0.17 (m_{lh}, calculated)
Refractive index, n	2.35 (1.0 μm) 2.60 (0.38 μm)	2.2 (0.60 μm) 2.5 (0.23 μm)	2.56 (1.0 μm) 3.12 (0.66 μm)
$\varepsilon_0(0)$	10.4(E‖c), 9.5(E⊥c)	9.14	
$\varepsilon_\infty(0)$	5.8(E‖c), 5.4(E⊥c)	4.84	9.3
Thermal conductivity, κ (W/cmK)	1.3	2.0	
Bulk modules (GPa)	207[a]		
TO (meV)	69.3 (TO⊥) 66.1(TO‖)	82.6	59.3
LO (meV)	92.5 (TO⊥)	112.8	86.1
Melting point (°C)	>1700	3000	1100
Nitrogen partial pressure at melting point (atm)	3000	100	$>10^5$
ΔG^0 (kcal/mol)	–33.0	–68.2	–23
Heat capacity, C_p (cal/molK)	9.7	7.6	10.0

 © 2000 COSiW SEP, Warsaw

the high melting point of III-Nitrides and the extremely high nitrogen partial pressures near the melting point make their bulk growth very difficult. Therefore, high quality III-Nitride substrates do not exist. The synthesis of nitride crystals has thus to be carried in the form of thin films on a non-native substrate. The dissimilarity between the substrate material and III-Nitrides generally lead to poor structural quality as a result of the lattice and thermal mismatch. Moreover, nitride alloys with different compositions are also lattice mismatched, which leads to dislocations in III-Nitride heterostructures. Finally, high free electron and hole concentrations are often difficult to achieve because most dopant elements form deep levels in wide bandgap, nitride semiconductors. The addition of more dopant source during the growth process frequently results in degradation of the structural and optical properties [8–10].

3. Areas of application

The driving force behind the exceptional interest in III-Nitride materials has been their potential for numerous significant device applications, both civilian and military. The majority of such devices can be divided into two categories: electronic and optoelectronic (photodetectors and light emitters) devices.

Electronic devices using III-Nitrides are needed for both high power and high temperature applications. High power and high temperature devices are in demand by the automotive, aerospace, and power industries. Power electronics have potential applications in the power industry and in any equipment which uses significant power, such as all electric vehicles, ships and aircraft. High temperature electronics would allow control directly in harsh environments, such as in engines, making them important in the automotive and aerospace industries. Because III-Nitride devices are expected to better withstand high temperatures while at the same time operate adequately, these electronics could be operated uncooled, thus reducing the cost and weight of systems.

Solar-blind UV photodetectors are devices which are sensitive to UV radiation while being (ideally) insensitive to longer wavelength radiation. Such devices have applications where there is a need to detect or control the source of UV radiation in an existing background of visible or infrared radiation [11]. Examples of such applications include flame detection, furnace and engine monitoring for the automotive, aerospace and petroleum industry, undersea communications, UV astronomy [12], space-to-space communications secure from Earth, early missile threat warning and airborne UV countermeasures, and portable battlefield reagent/chemical analysis systems. Thanks to their wide energy gap, III-Nitrides have been successfully used in UV photodetectors with very promising characteristics. Because of their theoretical intrinsic solar blindness and low dark currents, III-Nitride based devices are expected to work without optical filters and complex electronics, thus significantly reducing the launch weight for space and airborne applications.

Thanks to their ideally suited bandgap energy range, III-Nitrides have been successfully used in commercial bright blue and green light emitting diodes (LEDs). When used with the already available red AlGaAs based LEDs, these new LEDs complete the primary colours (red, green, blue) for large, high brightness, outdoor full-colour displays. Traffic lights are starting to use green LEDs because of their superior efficiency and reliability in comparison to incandescent light sources. Solid state white light sources using a combination of red, green, and blue LEDs or using phosphors excited by blue or ultraviolet (UV) LEDs may soon replace conventional light bulbs with better efficiency and reliability. UV LEDs could also replace the inefficient and hot "black" lights that are used in fun houses, tanning salons, and in more mundane applications such as killing bacteria in water.

The main thrust in recent III-Nitride research has been the fabrication of a reliable, short-wavelength (ultraviolet to green spectral region) laser diode. The primary advantage of shorter wavelengths is the ability to focus the beam to smaller spot sizes which scale as λ^{-2}, thus quadrupling the storage density of optical media by reducing the laser wavelength in half. The objective will be to achieve a digital video disk (DVD) system capable of storing 15 gigabytes by the year 2000. A DVD-RAM system would require a laser diode operating in continuous wave (CW) at 60°C, with an output power of 30–40 mW, and an operating voltage of 3 V at 100 mA. The requirements for a DVD-ROM system would only be a 4–5 mW CW laser. In both cases, the laser should have a wavelength of 400–430 nm. It must not be too short to avoid transmission losses in air. Visible laser diodes are also expected to be used in projective displays, optical communications and chemical analysis because the wavelength could be tuned to correspond to absorption lines of specific airborne chemicals to be detected. For example, a 55-inch large display needs a luminosity of 500 cd/m^2, which requires at least a 6.6 W, 1.8 W and 1.2 W red, green and blue lasers. Finally, laser printing is also an important application for short wavelength laser diodes. These would need to emit at a wavelength higher than 430 nm to avoid the decomposition of the toner components, with a single mode CW output power higher than 6 mW for fast printing.

Theoretical calculations have been conducted to compare the lasing threshold characteristics of GaN and GaAs based semiconductor lasers and the results are shown in Table 2. The theoretical threshold current densities were calculated using the formula

$$J_{th} = edBn_{th}^2 = edB\left(n_o + \frac{\alpha_{tot}}{\Gamma\beta}\right)^2,$$

where the parameters are defined in Table 2, and assuming no non-radiative recombination ($\eta_i = 1$). The threshold for GaN based lasers was found to be 2000 A/cm^2.

Table 2. Comparison of the GaN and GaAs-based laser properties.

Material	GaN (InGaN/GaN MQW)	GaAs (InGaN/GaN MQW)
Transparency carrier density n_0	10^{19} cm^{-3}	2×10^{18} cm^{-3}
Optical confinement factor Γ	5%	5%
Differential gain β	5×10^{-16} cm^2	1×10^{-15} cm^2
Typical total active layer thickness d	300 Å	100 Å
α_i	50 cm^{-1}	2 cm^{-1}
Radiative recombination coeff. B	3×10^{-11} cm^3/s	6×10^{-11} cm^3/s
J_{th}	2000 A/cm^2	40 A/cm^2

4. Substrates and growth techniques for III-Nitrides

Because of their extreme physical properties, bulk III-Nitride single crystals are barely available and their quality is not good enough to be used as substrates. Many non-native substrates have been investigated over the years for the epitaxy or growth of III-Nitride thin films. A non-exhaustive list of potential substrates and their physical properties is given in Tables 3 and 4. Reported values typically vary widely, so these numbers should be treated with caution.

A substrate must satisfy several properties in order to be suitable for epitaxial growth. First, it must be "compatible" with III-Nitrides, i.e., has a crystal structure (bulk and surface arrangement of atoms) which lends to the proper initial nucleation of oriented III-Nitride crystals during growth. The substrate lattice constant and the resulting lattice mismatch with the epilayer are important quantitative measures of this "compatibility" between substrate and epilayer, are useful in predicting the amount of stress for the epilayer. The data is tabulated in Table 3. The thermal expansion coefficient of the substrate is also an important parameter because a mismatch in these coefficients with other materials will result in mechanical stresses and cracks from cooling from the growth temperature and from cycling during processing and operation of the device. An estimate of the mismatch between the epilayer and the substrate caused by cooling 1000°C is given assuming the layer is relaxed at the growth temperature. The substrate must also be stable under the growth conditions typically used for III-Nitrides [13]. This is best quantified by the melting point of the substrate. Other substrate properties, such as thermal conductivity, energy gap and optical transparency in the visible spectrum, possibility to dope, maximum wafer size available and price are also given. All these properties will affect the choice of substrate for III-Nitride epitaxy depending on the application sought for.

To date, three substrates stand out as the most promising for III-Nitride growth: silicon, silicon carbide (SiC) and sapphire (Al_2O_3). Silicon is the most widely available substrate in the semiconductor industry and can come in sizes up to 10-inch diameter. It is also the cheapest one and the highest quality. However, it suffers from a poor "compatibility" with III-Nitride crystals. Also, it has a very narrow bandgap in comparison to nitrides, which makes it ill-suited for optical devices. At the other extreme, SiC offers the closest match with III-Nitrides, in terms of crystal symmetry, lattice and thermal mismatch with the nitrides. The lattice constant is smaller, resulting in compressive strain of the epilayer. On the other hand, the low thermal expansion coefficient of SiC results in tensile strain in the film upon cooling. It is a wide bandgap semiconductor being developed for applications in high power electronics and other demanding applications. Its drawback is its limited availability, small available size, its quality is still not as good as other Si or Al_2O_3 substrates, and its prohibitively high price [14]. Sapphire offers a compromise between the Si and SiC, and has become the most often used substrate for III-Nitride epitaxial growth. The appealing features include the high thermal and chemical stability, the large high quality wafers available, and the reasonable cost. However, there are large lattice and thermal mismatches. The thermal expansion coefficient is much larger than that of the III-Nitrides, resulting in a compressive strain in the epilayer upon cooling. The III-Nitrides generally grow on (0001) sapphire substrates with a 30° rotation about the c-axis with respect to the sapphire lattice, resulting in the alignment of the directions [00.1]||[00.1] and [10·0]||[11·0]. This results in a compressive strain on the III-Nitride layer since the effective lattice constant of the substrate given below is smaller than that of III-Nitride

$$a_{effective} = \frac{a_{Al_2O_3}}{\sqrt{3}}$$

The comparison of Si, SiC and Al_2O_3 as potential substrate for III-Nitride epitaxy is summarised in Table 5. GaN has been included in the table to reflect the properties of the bulk GaN single crystals which are currently being grown at high pressure by a few research groups in Poland [15]. At the present time, sapphire is the most viable substrate material in terms of quality, availability and cost.

Crystallographic models for the growth of III-Nitride thin films on these substrates have been developed to understand the atomic arrangements at the epilayer/substrate interface [16–20]. The comparison of different natures and orientations of substrates has been conducted [21].

 © 2000 COSiW SEP, Warsaw

Table 3. Structural properties of III-Nitride and potential substrate materials.

Formula	Name	Symetry	Point group	Space group	Stacking sequence (Wyckoff)	Lattice constant (Å)	Plane with nearest match to (0001) GaN	Effective a lattice constant (Å)	Δa/a with GaN
GaN	Gallium nitride	Hexagonal	6 mm	$P6_3mc$(186)	AB (HH)	a=3.1891 c=5.1855	(0001)	3.1891	0%
AlN	Aluminium nitride	Hexagonal	6 mm	$P6_3mc$ (186)	AB (HH)	a=3.112 c=4.982	(0001)	3.112	2.47%
InN	Indium nitride	Hexagonal	6 mm	$P6_3mc$ (186)	AB (HH)	a=3.5446 c=5.7034	(0001)	3.5446	–10.03%
4H-SiC	4H silicon carbide	Hexagonal	6 mm	$P6_3mc$ (186)	ABCB (CHCH)	a=3.073 c=10.053	(0001)	3.073	3.77%
6H-SiC	6H silicon carbide	Hexagonal	6 mm	$P6_3mc$ (186)	ABCACB (CCHCCH)	a=3.081 c=15.117	(0001)	3.081	3.51%
15R-SiC	15R silicon carbide	Trigonal	3 m	R3m (160)	$(CCHCH)_3$				
Al_2O_3	Sapphire, corundum	Trigonal	$\bar{3}$ m	R$\bar{3}$C (167)		a=4.758 c=12.991	(0001) rotated 30°	2.747	16.09%
$LiGaO_2$	LGO, lithium gallate	Orthorhombic	mm2	$Pna2_1$ (33)		a=5.402 b=6.372 c=5.007	(001)	3.119 3.186	2.25% 0.10%
$LiAlO_2$	LAO, lithium aluminate	Tetragonal	422	$P42_12$ (90)		a=5.1715 c=6.2840	(100)	2.986 3.142	6.81% 1.50%
$NdGaO_3$	NGO, neodymium gallate	Orthorhombic	mmm	Pbnm (62)		a=5.431 b=5.499 c=7.710 a=5.431 b=5.499 c=7.710	(101) (011)	3.175 3.144 3.136 3.157	0.45% 1.45% 1.71% 1.03%
ZnO	Zinc oxide	Hexagonal	6 mm	$P6_3mc$ (186)	AB (HH)	a=3.253 c=5.213	(0001)	3.253	–1.97%
MgO	Magnesium oxide	Cubic	m$\bar{3}$m	Fm$\bar{3}$m (225)		a=4.216	(111)	2.981	4.93%
Si	Silicon	Cubic	m$\bar{3}$m	Fd$\bar{3}$m (227)		a=5.4310202	(111)	3.8403112	–16.96
GaAs	Gallium arsenide	Cubic	$\bar{4}$3m	F$\bar{4}$ 3m (216)	ABC (CCC)	a=5.65325	(111)	3.99745	–20.22%

Although the growth of III-Nitrides has been conducted on non-native substrates, high quality films have been achieved which led to the demonstration of high performance devices, as will be discussed later in this paper. The dissimilarity between the substrates and nitride materials has been alleviated through the successful development of the growth technology, and more precisely the use of buffer layers [22].

One of the reasons why III-Nitrides have suffered from a lack of interest until the 1980s is because of the lack of suitable growth techniques. For example, because of their higher melting points, these materials required higher growth temperatures than conventional semiconductors, which then resulted in significant buoyancy in the gas flow pattern in chemical vapour deposition techniques.

Table 6 summarises the strengths and weaknesses of the currently most common growth techniques used to grow III-Nitride crystals, including metalorganic chemical vapour deposition (MOCVD), molecular beam epitaxy (MBE), vapour phase epitaxy (VPE), high pressure growth and sublimation sandwich method (SSM).

Currently, MOCVD and MBE are the most widely used techniques. MOCVD is undoubtedly the method of choice for the growth of high quality III-Nitrides films for mass production and particularly for devices. However, recently, VPE growth of III-Nitrides has gained attention for the growth of very thick GaN films for use as substrates after original substrate lift-off [23]. High-pressure growth remains limited to a few research groups in Poland for the direct growth of bulk GaN crystals. Finally, SSM has gained recently interest for the growth of bulk single crystal AlN. The III-Nitride material properties grown using these techniques will be presented in the next section.

Table 4. Other physical properties of III-Nitride and potential substrate materials.

Formula name	$\alpha_a(10^{-6}K^{-1})$ 0 to 1000°C	Mismatch with GaN by cooling 1000°C $(TEC_{GaN}-TEC_{sub})\times$ (–1000K)	Thermal conductivity (W/cmK)	Melting temperature °(C)	Energy gap (eV)	Transparent in visible?	Doping?	Maximum diameter (cm)	Low end price (to 1 significant figure ($/cm^2))
GaN	5.6 (0 to 600°C)	0%	1.3	>1700	3.44	Yes	n, p	–	–
AlN	5.7	0.01%	2.0	3000	6.2	Yes	Extremely difficult	–	–
InN	5.7(300°C)	0.01%		1100	1.9	No	n	–	–
4H-SiC	4.46	–0.11%	4.9		3.20	Impurity absorption	n, p	3.5	100
6H-SiC	4.44	–0.12%	4.9		2.86	Impurity absorption	n, p	3.5	100
15R-SiC			4.9			Impurity absorption	n, p	–	–
Al_2O_3	8.6	0.30%	0.3	2015	>8.5	Yes	Insulator	10	6
$LiGaO_3$	~7	0.14%		~1600		Yes		5	20
$LiAlO_2$				~1700		Yes		2	60
$NdGaO_3$ (101)	6.6 7.8	0.10% 0.22%	~1600					5	
$NdGaO_3$ (011)	11.9 6.1	0.63% 0.05%	~1600						
ZnO	7.8	0.22%		~2000	3.44(1.6K)	Yes	No?	2	300
MgO	13.85	0.83%	0.36	2800	7.9	Yes	Insulator	5	20
Si	3.90	–0.17%	1.3	1412	1.1242	No	n, p	30	
GaAs	6.7	0.11%	0.5	1240	1.424	No	n, p	5	4

All these growth techniques make use of precursors which are the source materials for each element (Al, Ga, In, N). These can come in the form of solid, liquid or gas depending on the growth technique used. A non-exhaustive list is tabulated in Table 7. It is worth noting that all group III element precursors are commonly used for the growth of other more conventional III-V semiconductors. Different group III sources have been compared for the growth of GaN [24]. The group V (nitrogen) sources are much more common than AsH_3 or PH_3 which makes them much safer to use, more available and much cheaper. However, there is still intense research to develop a better group V source, in terms of ease of cracking, purity and efficiency [25].

5. State-of-the-art of III-Nitride thin films

5.1. Aluminium nitride (AlN)

Aluminium nitride thin films have been synthesised for many years for use as a ceramic for coating because of their high physical strength. These films were all amorphous and were generally grown using RF sputtering.

It is only after the growing interest in GaN that more monocrystalline AlN films have been synthesised. Bulk AlN single crystals are being investigated using the sublimation sandwich method. Bulk AlN represents a future direction for the research on this material. However, AlN thin films are generally grown on basal plane Al_2O_3 or SiC substrates, without a buffer layer. This is due to the fact sapphire and AlN share a common element; aluminium, which makes the bonding at the interface much easier. Epitaxial

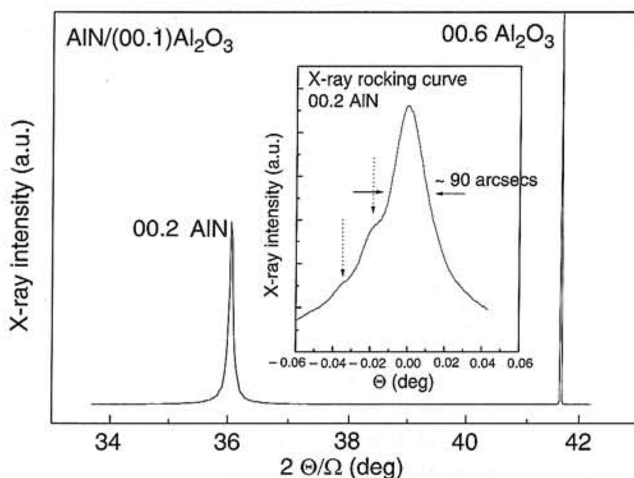

Fig. 2. Symmetric X-ray diffraction spectra of an AlN film on basal plane sapphire (after Ref. 27).

 © 2000 COSiW SEP, Warsaw

Table 5. Comparison of the most promising substrates for III-Nitride growth.

Substrate issues for III-Nitride growth	GaN	Si	6H-SiC	Al_2O_3
Crystal symmetry	++	–	+	+
Compatibility of process	++	–	+	+
Lattice mismatch	+	– –	–	– –
Thermal mismatch	+	–	–	–
High quality	+	++	–	+
Availability	– –	++	–	+
Size (large area)	– –	++	–	+
Cheap ($)?	n/a	+	–	+

films are rarely thicker than 1–1.5 µm. High crystalline quality films have been achieved on Al_2O_3 and SiC substrates with open detector symmetric X-ray rocking curve linewidths as low as 90 and 60 arcsecs respectively, as shown in Fig. 2 [26,27].

As grown AlN films are almost always insulating. The origins of this behaviour are still controversial and much research work is needed to understand the insulating behaviour of AlN. Negative electron affinity (NEA) has also been reported from AlN films [28]. This effect has been used to demonstrate cold cathode structures using AlN films [29]. The piezoelectric properties of AlN has been investigated for a number of years for Surface Acoustic Wave (SAW) applications [30]. The optical properties of AlN are assessed through optical absorption (Fig. 3) and cathodoluminescence.

The nonlinear optical properties of AlN are an interesting field for future research which has been little touched, although second harmonic generation from AlN films were conducted and yielded the non linear coefficients

$$\chi^{(2)}_{zzz} = 10 pm/V \text{ and } \chi^{(2)}_{zxx} = 0.5 pm/V$$

Table 6. Strengths and weaknesses of most common growth technologies for III-Nitride.

Growth technology	Strengths	Weaknesses	Frontier for 21st Century
Metal-organic chemical vapour deposition MOCVD MOVPE	• Well developed technology • Atomically sharp interfaces • *In-situ* thickness monitoring • High growth rates (<4 µm/hr) • Easily scaleable for mass production • Short run cycles (heat+growth+cool) • Possibility to use plasma or laser assisted growth	• Lack of precise *in-situ* characterization • Large quantities of NH_3 are needed	Mass production of high quality III-Nitride thin films and devices
Molecular beam epitaxy MBE, GSMBE, MOMBE	• Well developed technology • Atomically sharp interfaces • Precise *in-situ* characterization • High purity growth environment • Hydrogen free environment • Scalable for mass production	• Need for ultra-high vacuum (cryogenics) • Long run cycles (heat+growth+cool) • Growth temperature is limited on the high end • Efficiency of nitrogen source or cracker (ECR, RF) is limited • Low growth rates [<1–1.5 µm/hr] • Not as high throughput as MOCVD	Growth in hydrogen-free environment
Vapor phase epitaxy VPE, HVPE	• Simple growth technique • Very high growth rate (<100 µm/hr) • Reasonably good quality films	• No sharp interfaces • Long run cycles (heat+growth+cool) • Small area growth • Better films are obtained for lower growth rates	Thick GaN films for substrates
High pressure growth	• Bulk GaN single crystals	• Only for GaN single crystals • Small size crystals (few mm^2 area) • Extreme temperature and pressure conditions	Bulk GaN single crystals for substrate use
Sublimation sandwich method SSM	• Very simple growth technique • Extremely high growth rate (<300 µm/hr)	• Poor qualty of films • Need a GaN powder source • Small area growth	Bulk AlN single crystals for substrate use

Table 7. Most common chemical precursors for the growth and doping of III-Nitride.

Element group	Chemical formula	Chemical name	Chemical family	Physica state at 20°C	Growth technique	Toxicity
III	$(CH_3)_3$–, $(C_2H_5)_3$–Al	Trimethy, triethyl-alumimum (TMAI, TEAl)	Organometallic	Liquid	MOCVD, MBE	Pyrophoric
	$AlH_3N(CH_3)_3$	Alane trimethylamine	Organometallic	Solid	MOCVD, MBE, VPE	
	$(CH_3)_3$–, $(C_2H_5)_3$–Ga	Trimethy-, triethyl-gallium (TMGa, TEGa)	Organometallic	Liquid	MOCVD, MBE	Pyrophoric
	$GaCl_3$	Gallium chloride	Metal chloride	Solid	VPE	
	$(CH_3)_3$–In	Trimethy-indium (TMIn)	Organometallic	Solid	MOCVD, MBE	Pyrophoric
	$(C_2H_5)_3$–In	Triethyl-indium (TEIn)	Organometallic	Liquid	MOCVD, MBE	Pyrophoric
	$InCl_3$	Iodium chloride	Metal chloride	Solid	VPE	
	Al, Ga, In	Aluminum, gallium, indium	Metal	Solid	MBE, VPE	No
V	N_2	Nitrogen	Inorganic gas	Gas	MOCVD, MBE	No
	NH_3	Ammonia	Nitrogen hydride	Gas	MOCVD, MBE, VPE, sublimation	Corrosive
	N_2H_4	Hydrazine	Nitrogen hydride	Gas	MOCVD	
	$(CH_3)_3CNH_2$	Tertiarybutylamine	Organometallic	Liquid	MOCVD	
	$C_6H_5NHNH_2$	Phenylhydrazine	Organometallic	~Liquid	MOCVD	
III-V	AlN	Aluminum nitride	Powder	Solid	Sublimation	No
	GaN	Gallium nitride	Powder	Solid	Sublimation	No
II (p-type dopant)	Cp_2Mg	Biscyclopentadienyl-magnesium	Organometallic	Solid	MOCVD, MBE, VPE	Pyrophoric
	Mg	Magnesium	Metal	Solid	MBE	No
	DEZn	Diethyl-zinc	Organometallic	Liquid	MOCVD, MBE, VPE	Pyrophoric
	DMZn	Dimethyl-zinc	Organometallic	Liquid	MOCVD, MBE, VPE	Pyrophoric
	Zn	Zinc	Metal	Solid	MBE	No
VI (n-type dopant)	SiH_4	Silane	Hydride	Gas	MOCVD	Pyrophoric
	Si_2H_6	Disilane	Hydride	Gas	MOCVD	
	Si	Silicon	Metal	Solid	MBE	No
	GeH_4	Germane	Hydride	Gas	MOCVD	Toxic
	H_2S	Hydrogen sulfide	Nonmetal hydride	Gas	MOCVD	Toxic
	H_2Se	Hydrogen selenide	Nonmetal hydride	Gas	MOCVD	

5.2. Gallium nitride (GaN)

GaN is by far the most studied III-Nitride material. A thin AlN, GaN or AlGaN buffer layer is generally used for the growth. Basal plane Al_2O_3 and SiC substrates are most commonly used. Films as thick as 100 μm have been reported, depending on the growth technique utilised. In face of the growing interest in these materials, there has been an effort to grow bulk GaN single crystals using high-pressure growth or hydride VPE followed by substrate lift-off. This is undoubtedly a promising topic for future research.

High crystalline quality GaN thin films have been achieved, with open detector X-ray rocking curve linewidths as low as 30 arcsecs (Fig. 4) and asymmetric X-ray rocking curve linewidths as low as 400 arcsecs [27]. The thermal stability of GaN has been reported [31].

Undoped GaN films are usually either highly resistive or exhibiting n-type conduction with a residual carrier concentration ~ 10^{16} cm^{-3} at room temperature and an electron mobility as high as 900 cm^2/Vs. Theoretical calculations

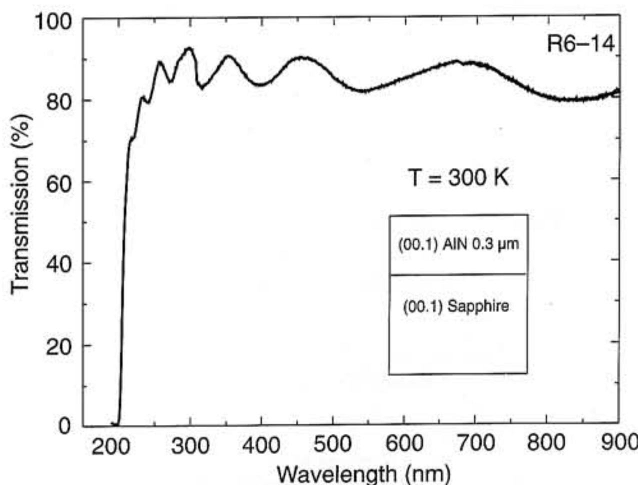

Fig. 3. Room temperature optical absorption of AlN film on basal plane sapphire (after Ref. 27).

 © 2000 COSiW SEP, Warsaw

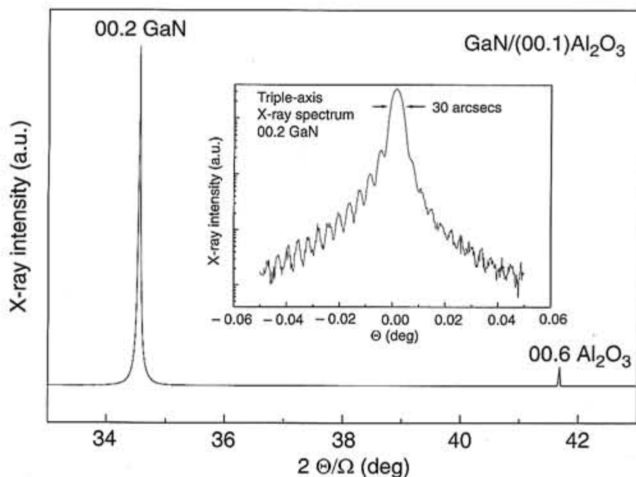

Fig. 4. Symmetric X-ray diffraction spectrum of an GaN film on basal plane sapphire (after Ref. 27).

showed that the maximum 300 K electron mobility in GaN was 2350 cm²/Vs. The pyroelectricity properties of GaN have been measured and yielded a pyroelectric voltage coefficient of ~ 10^4 V/mK.

The optical properties of GaN are usually assessed through optical transmission and photoluminescence (PL), as shown in Fig. 5. Free excitons A, B, and C have been observed with peak linewidths of ~ 1–3 meV at 2 K using photoluminescence (PL). The room temperature PL linewidths are typically as low as ~ 30 meV, as shown in Fig. 5. Residual acceptor and donor related luminescence transitions are often observed as well. A broad "yellow" luminescence is sometimes observed and has been attributed to defects in GaN (see Section 7). Transition metals (e.g., Fe, V) have been observed by infrared spectroscopy. Second harmonic generation from GaN films have yielded the non linear coefficients; $\chi^{(2)}_{xzx} = \chi^{(2)}_{zxx}$ which was 11 times the $\chi^{(2)}_{xxx}$ of quartz, and $\chi^{(2)}_{zzz}$ which was –22 times the $\chi^{(2)}_{xxx}$ of quartz [6].

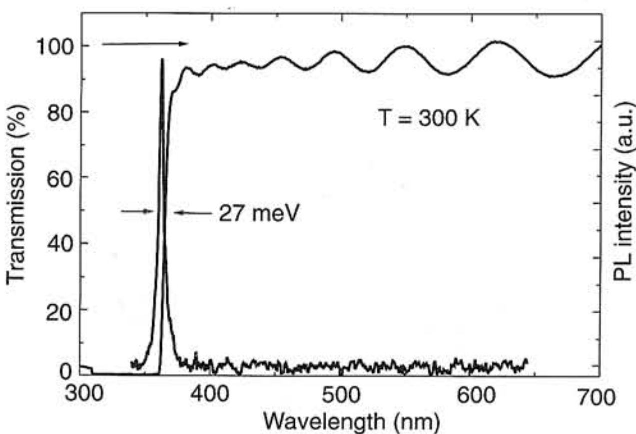

Fig. 5. Room temperature optical transmission and photoluminescence from an GaN film on Al_2O_3 substrate (after Ref. 27).

5.3. Ternary $Al_xGa_{1-x}N$

Ternary $Al_xGa_{1-x}N$ has been grown over the entire compositional range. Generally an AlN or GaN buffer layer is used, although there are some reports of AlGaN buffers. Here again, basal plane Al_2O_3 and SiC are the preferred substrates. The films are typically thinner than 1–1.5 µm. High crystallinity AlGaN films have been achieved on sapphire substrates, with open detector symmetric X-ray rocking curve linewidths as low as 100 arcsecs [32].

The resistivity of $Al_xGa_{1-x}N$ was found to increase exponentially with Al concentration (x) [32]. This behaviour still needs to be understood and is an important area of future research. Low Al concentration alloys sometimes show limited n-type conduction due to residual donors as in the case of GaN. $Al_xGa_{1-x}N$ are reported to exhibit negative electron affinity for x > 0.75 and have been used in cold cathode applications [29].

The optical properties of $Al_xGa_{1-x}N$ have been assessed using cathodoluminescence and optical absorption, in particular to determine the bandgap energy as shown in Fig. 6. A bandgap bowing parameter has been measured to be between –1.0 and 1.0 eV, as shown in Fig. 7 [33]. Calculations (for zinc blende $Al_xGa_{1-x}N$) have predicted this parameter to be 0.53 eV. There is some uncertainty on the ex-

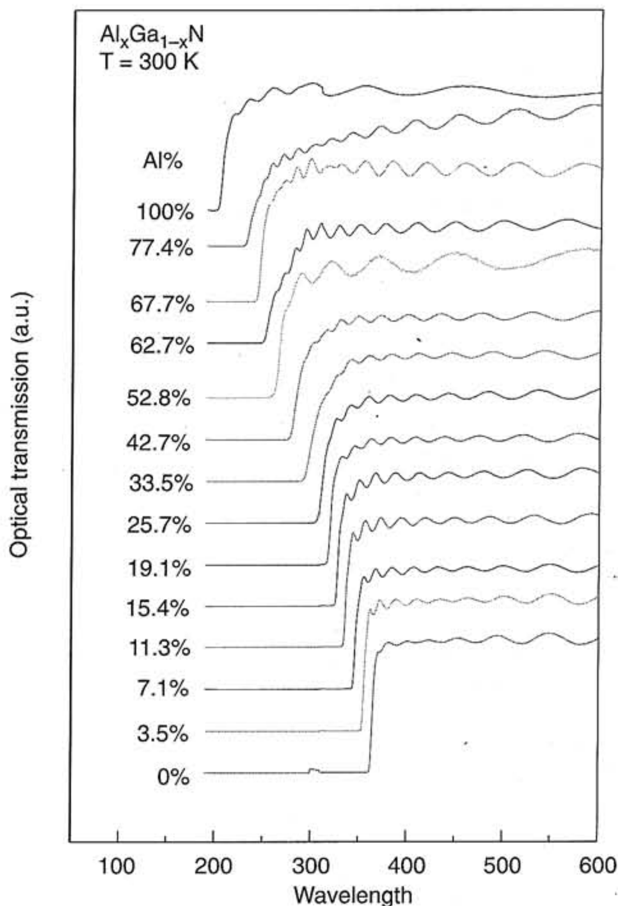

Fig. 6. Room temperature optical transmission of $Al_xGa_{1-x}N$ for $0 \le x \le 1$ (after Ref. 32).

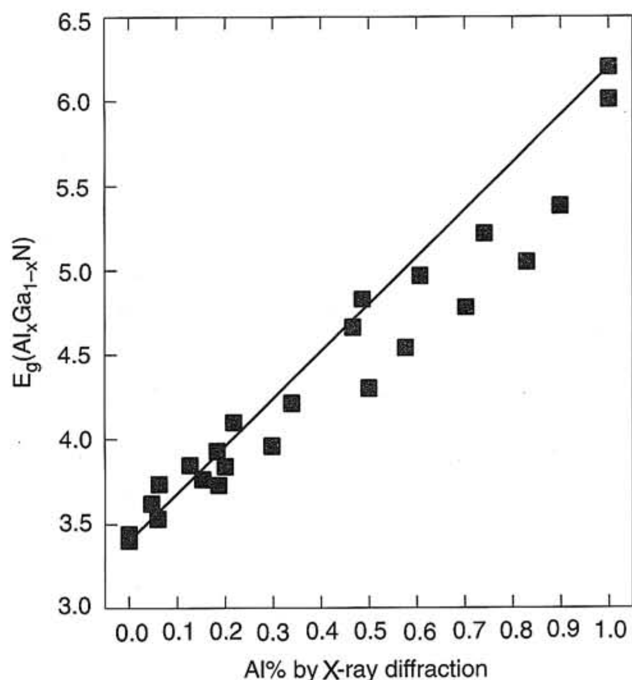

Fig. 7. Room temperature energy gap of $Al_xGa_{1-x}N$ determined by optical absorption as a function alloy composition as determined by X-ray diffraction (after Ref. 33).

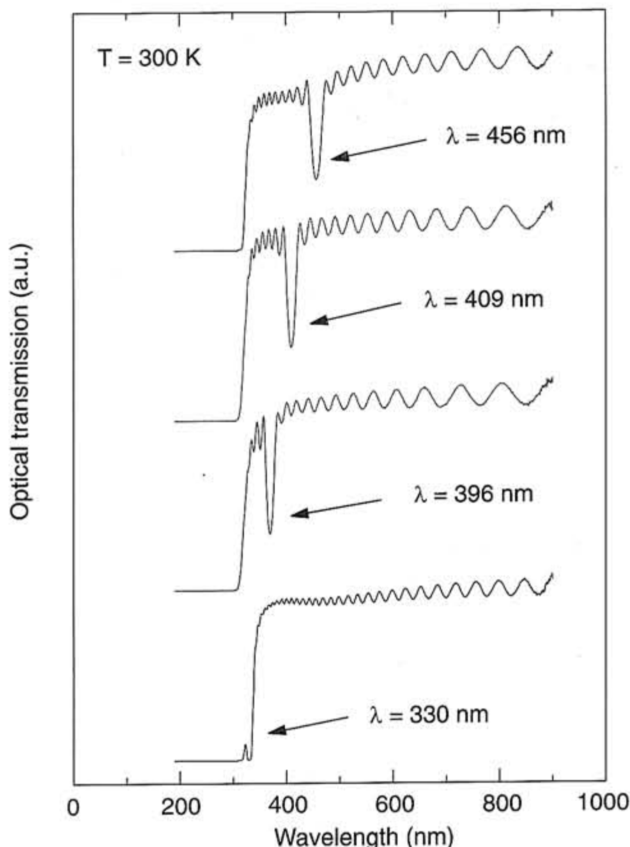

Fig. 8. Room temperature optical transmission of $Al_xGa_{1-x}N$/$Al_yGa_{1-y}N$ multilayer Bragg reflectors (after Ref. 32).

act alloy composition due to the presence of strain in the thin films. Ellipsometry and photoreflectance measurements have been conducted and yielded the refractive index of a few $Al_xGa_{1-x}N$ alloys (e.g., 0.1 lower than GaN for x = 0.1).

5.4. AlGaN/GaN heterostructures

One of the main advantages of the III-Nitrides over other wide bandgap materials such as SiC is the potential to fabricate heterostructures and achieve bandgap engineering within the same material system. However, AlGaN/GaN heterostructures are still in their infancy and much remains to be done.

Two dimensional electron gas (2DEG) has been demonstrated at the AlGaN/GaN interface. Room temperature electron mobilities as high as 2000 cm^2/Vs have been measured for a sheet carrier density of 10^{13} cm^{-2}. At 20 K, the electron mobilities were as high as 5700 cm^2/Vs and 7500 cm^2/Vs for structures on sapphire and SiC substrates for a sheet carrier of 5×10^{12} cm^{-2} [34]. Theoretical modellings showed that piezoelectric scattering, as well as polar optical and ionised impurity scattering, played an important role in the mobility of 2DEG in GaN [35].

Calculations of the strain induced piezoeffect at lattice mismatched III-Nitrides have been carried out. The piezoelectrically induced charge in GaN/AlGaN has been measured in the field effect transistor structures [36].

Band alignments in the III-Nitride material system have been investigated and remain a controversial issue. Theoretical calculations estimated that the valence band offsets of (wurtzite) AlN, GaN and InN to be; AlN/GaN = 0.7–0.81 eV and GaN/InN = 0.3–0.48 eV. Experimental measurements of the valence band offsets yielded: AlN/GaN = 0.70–1.36 eV, GaN/InN = 1.05 eV and AlN/InN = 1.81 eV [37].

Bragg reflectors using $Al_xGa_{1-x}N/Al_yGa_{1-y}N$ multilayers have been demonstrated. The peak reflectivity could be tuned by varying the periods of the multilayer structures, as shown by the sudden decrease in the optical transmission spectrum in Fig. 8 [32].

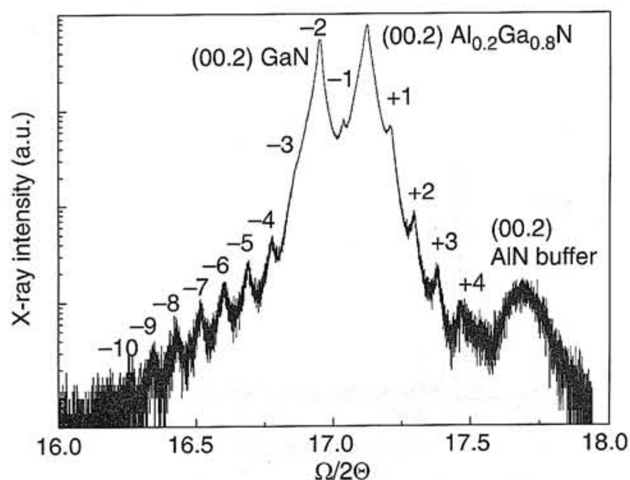

Fig. 9. Open detector x-ray diffraction spectrum of a 13 period (500Å $Al_{0.2}Ga_{0.8}N$/50Å GaN) superlattice (after Ref. 32).

 © 2000 COSiW SEP, Warsaw

X-ray diffraction from AlGaN/GaN superlattices have revealed clear satellite peaks, as shown in Fig. 9. This confirms that high structural quality interfaces can be achieved in this material system.

5.5. Ternary $Ga_{1-x}In_xN$

Ternary $Ga_{1-x}In_xN$ have been grown in the entire composition range. However, the material quality significantly deteriorates as the In concentration increases. It was shown that the $Ga_{1-x}In_xN$ alloy composition and material quality very strong depended on the growth conditions, in particular the growth temperature, growth pressure, V/III ratio, growth rate. To grow alloys with higher In concentration, it is generally necessary to lower the growth temperature, raise the growth pressure, increase the V/III ratio and growth rate [38].

Moreover, it has been reported that GaN and InN have a miscibility gap [39]. $Ga_{1-x}In_xN$ films are generally thin (< 0.5 μm) and are grown on thick GaN films (> 1 μm) on basal plane Al_2O_3 or SiC substrates. The X-ray rocking curve linewidths can be as low as 480 arcsecs (for 14% In) [40].

As grown $Ga_{1-x}In_xN$ films generally show n-type conduction ($n > 10^{17}$ cm^{-3} at 300 K). Room temperature photoluminescence measurements showed that $Ga_{1-x}In_xN$ can have a linewidth as low as 70 meV (for 14% In). The bandgap bowing parameter has been measured to be between 1.0 and 3.2 eV, as shown in Fig. 10 [33]. Theoretical calculations (for zinc-blende $Ga_{1-x}In_xN$) predicted a value of 1.02 eV. Ellipsometry has yielded the refractive index of $Ga_{1-x}In_xN$ to be ~ 0.05 higher (for x = 0.06) than that of GaN.

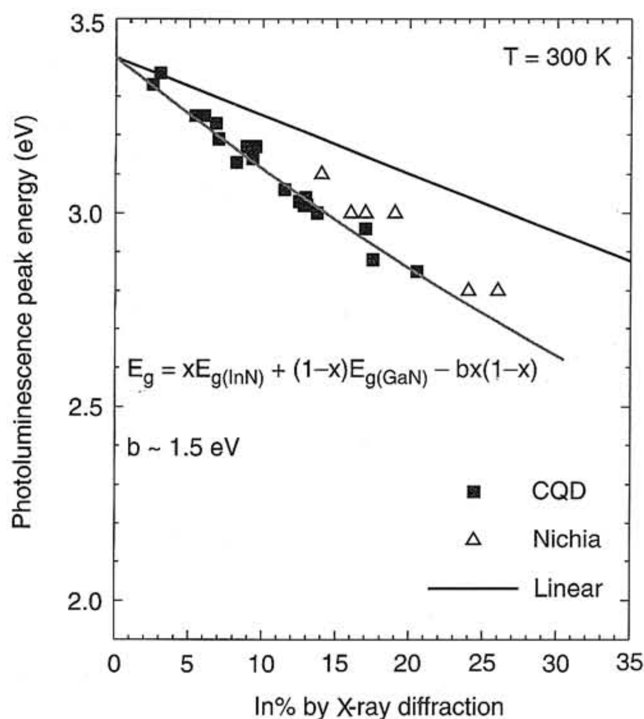

Fig. 10. Room temperature energy gap of $Ga_{1-x}In_xN$ determined by photoluminescence as a function alloy composition as determined by X-ray diffraction (after Ref. 33). Data points labeled "Nichia" are taken from reference (after Ref. 40). Data points labeled "CQD" are taken from reference (after Ref. 33).

Improving the quality of $Ga_{1-x}In_xN$ compounds for x > 0.5, as well as enhancing the uniformity of the growth over large areas remain a challenge for the future.

5.6. GaInN/GaN heterostructures

GaInN/GaN heterostructures and quantum wells have been reported, although they have been more often characterised in actual devices [41,42].

The cathodoluminescence intensity was shown to increase by several orders for GaInN/GaN multi-quantum wells compared to bulk GaInN films [43]. There have been reports of "composition pulling effect" in thin GaInN films grown on GaN [44]. It was shown that the lattice mismatch between the growing GaInN layer and the underlying GaN prevented the incorporation of indium into the lattice. This can have significant effect in the control of the emission wavelength from GaInN/GaN quantum wells. Finally, quantum confined Stark effect in GaInN/GaN multiquantum wells due to piezoelectric effects has been recently reported to influence the optical properties of these structures [45]. This effect can be minimised by adequately doping the structures with Si.

6. Doping of III-Nitrides

In order to fabricate devices, it is necessary to control the doping of III-Nitrides. The n-type doping in these materials has generally been much easier than the p-type doping. This is mainly because III-Nitrides have the tendency to exhibit n-type conductivity as grown. Like other III-V semiconductors, the n-type doping can be achieved using group VI elements, while the p-type doping is achieved by incorporating group II elements. Group IV elements, such as Si and Ge, act as donors in III-Nitrides, whereas C seems to act as an acceptor. This is due to the fact that Si and Ge have an electronegativity closer to Al, Ga, and In than N, and thus would be more likely to replace Al, Ga, and In than N. The electronegativity of C is closer to N than to the group III elements, and thus would more likely to replace N in the III-Nitride lattice.

6.1. n-type doping

There have been a few reports of Ge doped AlN films which exhibited n-type conductivity, although not much information is available.

The n-type doping of GaN films has been much more investigated using Si, Ge [46], Se, sulfur [47] and oxygen. The most successful dopants have been Si and Ge. Doping control has been achieved up to a carrier concentration of 10^{20} cm^{-3}. The Si level in the bandgap was estimated to be

~ 22 ±4 meV below the bottom of the conduction band [48]. Impurity band conduction is usually observed at low temperatures.

The n-type doping of $Al_xGa_{1-x}N$ compounds has been successfully carried out using Si and Ge [49]. n-type conduction has been observed up to an Al concentration of $x < 0.6$. Future research will be oriented towards enhancing the n-type conductivity for alloys with $x > 0.6$. The n-type doping of $Ga_{1-x}In_xN$ alloys using Si has also been conducted, although this has not been done to enhance the electrical properties of the films but rather the optical properties. It was shown that Si doping of $Ga_{1-x}In_xN$ significantly increased the photoluminescence intensity [50].

6.2. p-type doping

There have been only very few reports of doping of AlN films by incorporating unusually high amounts of C into the lattice [51].

The p-type doping of GaN films has been achieved using Mg. The doping control is at all not easy, as it is very sensitive to dopant flow rate. As doped films are generally insulating (except a few reports of as grown p-type GaN by MBE) and require post-growth treatment such as thermal annealing (> 600°C under nitrogen or vacuum) or low energy electron beam irradiation (LEEBI) to activate the p-type dopant [52,53]. The mechanism by which this happens has been identified as the breaking of Mg-H bond [54]. The concentration of Mg atoms in the lattice is typically 10^{19} cm^{-3}, but the room temperature free hole concentrations are generally 5×10^{18} cm^{-3} for a mobility 20 cm^2/Vs. The activation energy of Mg has been estimated to be 150–200 meV. Impurity band conduction is also observed at low temperatures in p-type GaN films.

The p-type doping of $Al_xGa_{1-x}N$ has been carried out using Mg and the alloys showed p-type conductivity up to $x < 0.3$ [32]. $Ga_{1-x}In_xN$ alloys have also been p-type doped using Mg for $x < 0.09$ [55].

Much more research work in the p-type doping of III-Nitrides is necessary in the future, in particular for GaN and for $Al_xGa_{1-x}N$ for $x > 0.3$. Research directions include new doping sources, new doping scheme involving co-doping [56].

7. Defects in III-Nitrides

7.1. Investigation of defects in III-Nitrides

Because nearly all III-Nitride films used in devices are grown on a foreign substrate, defects will necessarily form at the epilayer/substrate interface. The high densities of defects generally lead to much confusion and has made it difficult to separate the effects due to one type of defect from those due to another.

The GaN films grown on sapphire exhibit a limited coherence length which is at the origin of the GaN X-ray diffraction peak broadening, as determined through reciprocal space maps of GaN films on Al_2O_3. This was consistent with transmission electron microscopy (TEM) measurements [57].

Threading dislocations and stacking faults are one of the most common defects in III-Nitrides and are visualised using TEM. AlN films on sapphire generally exhibit threading dislocation densities ~ 10^{10} cm^{-2} with Burgers vectors of the type 1/3 <11–20> [58]. Threading dislocations densities in GaN are generally higher than 10^8 cm^{-2}, even for GaN on limited bulk GaN substrate. The Burgers vectors are of the type 1/3 <11–20> (pure edge) and 1/3 <11–23> (mixed screw-edge) [59].

Some of these defects can be visualised through etch pit revelation after wet chemical etching. Etch pits have been studied and compared in GaN grown using different Ga precursors [24]. Different etch pit sizes and shapes were observed. An etch pit density of ~ 10^4 cm^{-2} could be determined. Atomic force microscopy and TEM have also been used to reveal pits in GaInN [60].

Point defects are usually experimentally observed indirectly using optical methods such as photoluminescence or cathodoluminescence. For example, Ga vacancies have been shown, both experimentally and theoretically, to be one cause for the yellow photoluminescence in GaN films [61]. Spatially resolved cathodoluminescence also revealed that this yellow luminescence was stronger at grain boundaries [62].

Obviously, the ultimate objective will be to achieve defect-free III-Nitride films. Unless high quality bulk III-Nitride substrates become available, other approaches have to be developed to reach this goal. The first will be to use of compliant substrates with wafer bonding and substrate lift-off [63]. This has been achieved for InSb on GaAs. However, several issues, such as the stiffness of III-Nitride materials, Al_2O_3 or SiC substrates are likely to limit the applicability of this technique for III-Nitrides. Lateral epitaxial overgrowth, followed by substrate lift-off as well, is a promising technique to achieve nearly dislocation free films. This requires the capability to apply a dielectric pattern onto a template layer, followed by single or multiple-step regrowth [64]. Because of its fast increasing importance, the lateral epitaxial overgrowth of GaN will be discussed in more details in the following subsection. Finally, multilayer techniques can also be used to minimise the propagation of threading screw dislocations to a density below 10^7 cm^{-2} [65].

7.2. Lateral epitaxial overgrowth of GaN

Lateral epitaxial overgrowth (LEO) is a promising growth method to achieve quasi defect free GaN-based materials, a goal of which has thus far eluded the research community, on potentially any type of substrate [64]. To the date, basal plane sapphire substrates, (00.1) Al_2O_3, have been mostly used for the LEO of GaN because high quality GaN

 © 2000 COSiW SEP, Warsaw

films can already be grown by conventional epitaxial growth techniques. LEO was successfully used to reduce dislocations in GaN-based laser diodes on (00.1) Al_2O_3 and enhance the lifetime of these devices [66]. Because LEO can be applied to any substrate, it is also important to investigate the potential of GaN LEO on silicon (Si) substrates because of their current commercial and technological significance.

In the following paragraphs, the LEO growth and characterisation of Si doped GaN on (00.1) Al_2O_3 and (111) Si substrates by MOCVD will therefore be discussed [67]. The LEO growth on Si substrates was made possible only after achieving high quality GaN "template" films on (111) Si (i.e., GaN on plain Si) which will also be described here.

The substrates were chemically cleaned prior to loading into the MOCVD reactor. The GaN template layers on sapphire were 1–2 μm thick, whereas those on silicon were only 0.2–1 μm thick. Next, a 2000Å thick SiO_2 film was deposited. Standard photolithography and etching were used to define a 15-μm period pattern consisting of 3 μm-wide stripe openings. The crystallographic orientation of the stripes will be discussed later in the paper. The samples were then loaded back into the reactor for regrowth of Si doped GaN.

The characteristics of the GaN template layers on sapphire substrates has already been in subsection 5.2. Several parameters need to be optimised in order to achieve high quality LEO GaN. First, is the orientation of the stripes with respect to the crystallographic directions of the underlying GaN template. In earlier work on the LEO of GaN, it was shown that for stripes parallel to <10.0> of GaN a rectangular cross section is obtained, whereas for stripes parallel to <11.0> of GaN a truncated or complete pyramidal shape is obtained [68]. In the former case, a higher lateral-to-vertical (L/V) growth rate ratio than in the later case is observed. The origin of this behaviour is attributed to the slow growth rate of the $\{1\bar{1}.1\}$ planes of GaN [69]. In the literature, there has been some confusion on the labelling of crystallographic directions for hexagonal symmetry crystals such as GaN and Al_2O_3 [64,69]. Here, it is chosen to use a four-digit notation for crystallographic directions. The conversion between a three digit, i.e. <uvw>, and a four digit notation, i.e. <UVTW> or <UV.W>, is not a one-to-one direct identification of digits but is given by the set of equations [17]

$$U = \frac{(2u - v)}{3} \qquad u = 2U + V,$$

$$V = \frac{(2v - u)}{3} \qquad v = U + 2V,$$

$$T = -\frac{(u + v)}{3} \qquad w = W,$$

$$W = w.$$

Because it is easier to align the stripes with respect to the sapphire substrate than to the epilayer, knowledge of the crystallographic relationships between a GaN film and a basal plane Al_2O_3 substrate is necessary and is summarised in Table 8 [17].

In the early stages of GaN regrowth, it is necessary to avoid nucleation on the masked areas in order to confine the growth in the open windows. Secondly, it is desired to achieve as high a L/V growth rate as possible (thus with the stripes parallel to $<10.0>_{GaN}$) in order to minimise the amount of time needed to cover the wafer surface. In both cases, this means one needs to enhance the surface diffusion of adatoms. One method to do so is by decreasing the growth rate, however it must not be so low that growth durations become impractical. Another method is to increase the growth temperature. However, it was found that at very high temperatures, the SiO_2 mask deteriorates as their edges start "eroding", the underlying GaN starts decomposing, and a non uniform mushroom shape cross section for the LEO grown GaN resulted instead of the desired rectangular shape.

Under optimised growth conditions, Fig. 11(a) shows an SEM micrograph of the LEO grown GaN, showing a rectangular cross section. The duration of the growth was only 10 minutes. The GaN grew ~ 2600 nm laterally and ~ 475 nm vertically above the SiO_2 mask, which corresponds to a L/V growth rate ratio close to 5.5. By pursuing the growth, the LEO film coalesced as show in the SEM cross section and surface micrographs in Figs. 11(b) and (c). Small void areas can be observed in the cross section at the junction between two lateral growth fronts, and seamlines can be seen on the surface at that location. Figures 12(a) and (b) show the X-ray diffraction and 300 K photoluminescence spectra from these coalesced films. The X-ray and PL peak linewidths were 7 arcmins and ~ 95 meV, respectively. The X-ray linewidth is on the same

Table 8. Crystallographic relationships between GaN grown on sapphire and silicon substrates.

Epilayer/substrate	Four digit notation	Three digit notation
(00.1) GaN/(00.1) Al_2O_3	$[10.0]_{GaN} \parallel [11.0]_{Al2O3}$ $[\bar{1}\,2.0]_{GaN} \parallel [\bar{1}\,1.0]_{Al2O3}$	$[210]_{GaN} \parallel [110]_{Al2O3}$ $[010]_{GaN} \parallel [\bar{1}\,10]_{Al2O3}$
(00.1) GaN/(111) Si	$[10.0]_{GaN} \parallel [\bar{1}\,\bar{1}\,2]_{Si}$ $[\bar{1}\,2.0]_{GaN} \parallel [1\,\bar{1}\,0]_{Si}$	$[210]_{GaN} \parallel [\bar{1}\,\bar{1}\,2]_{Si}$ $[010]_{GaN} \parallel [1\,\bar{1}\,0]$Si

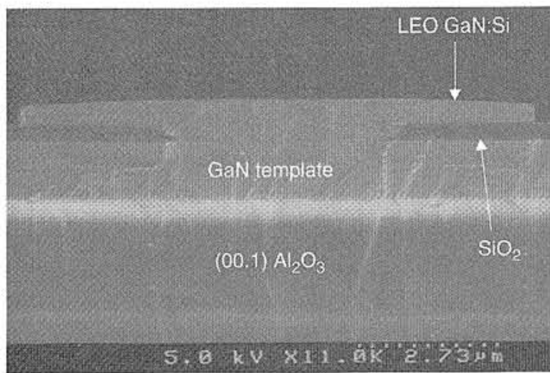

(a)

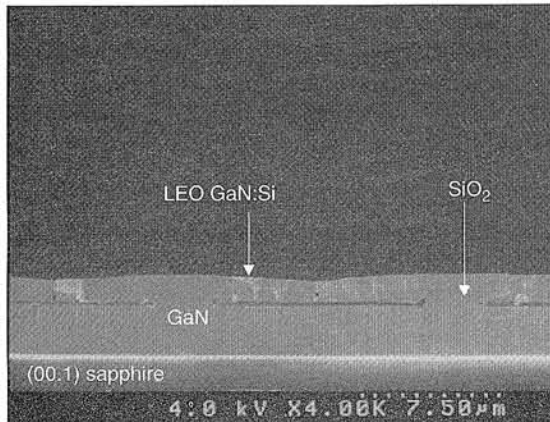

(b)

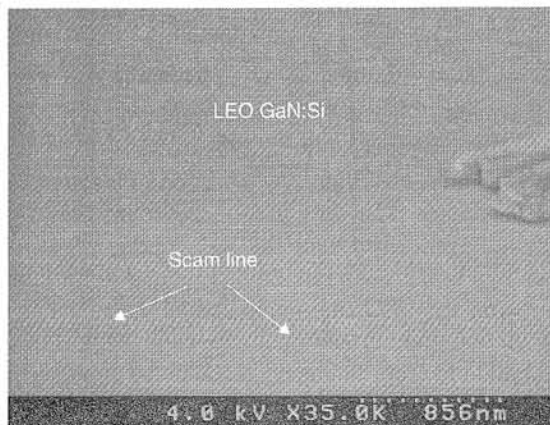

(c)

Fig. 11. SEM micrograph of the cross section of a non-coalesced LEO grown GaN:Si on (00.1) Al_2O_3 substrate (a), of the cross section (b) and surface (c) of a coalesced LEO grown GaN:Si film on (00.1) Al_2O_3 substrate (after Ref. 67).

order as the template layer used in these experiments. The PL peak is broader than for a same thickness GaN grown under similar conditions on plain sapphire and doped with the same amount of Si, which usually has a linewidth of ~ 60 meV. This suggests that there is additional impurities incorporated during LEO growth which enhance and broaden the PL. The most probable candidates for such impurities are silicon and oxygen from the SiO_2 mask which may be slightly decomposing at such high temperatures.

These LEO results were then applied to the LEO of GaN on silicon substrates. However, prior to carrying the LEO of GaN on silicon, it was necessary to achieve as high crystalline quality GaN template films on silicon as possible. ~ 1.2 µm thick undoped GaN films were grown and characterised on (111) silicon substrates. A typical X-ray diffraction and 300 K PL spectra is shown in Fig. 13. The linewidths of the X-ray and PL peaks were ~ 10.5 arcmins and 30 meV, respectively for a GaN grown on nearly on-axis Si substrate. These show that the GaN thus grown on Si have a high structural and optical quality, close to some of the early GaN epilayers on sapphire [70]. It was observed that the characteristics of these GaN layers depended on the quality of the (111) Si substrates used. The 1.2-µm thick films were heavily cracked as a result of the difference in thermal expansion coefficients between (00.1) GaN and (111) Si [26,68]. Crack free GaN template layers used for LEO were thus chosen with a thickness of ~ 0.2 µm. In order to define a stripe pattern on these templates with stripes parallel to $<10.0>_{GaN}$, it was necessary to know the relationship between the crystallographic directions of (00.1) GaN and (111) Si. Following crystallographic models and asymmetric X-ray diffraction measurements, these relationships are summarised in Table 8 [14].

Under optimised growth conditions, a quasi rectangular cross section is obtained for LEO grown GaN on (111) Si, as shown in Fig. 14. The duration of the growth was 25 minutes. The GaN grew ~ 4900 nm laterally and ~ 950 nm vertically above the SiO_2 mask, which corresponds to a L/V growth rate ratio close to 5.2, which is nearly as high as for the LEO on Al_2O_3 substrates. Figure 14 also shows an AFM image of the surface of the regrown GaN on Si substrates in relation with the SEM cross section. The side of the AFM image corresponds to 10 µm and the vertical scale is 74.4 nm. It can be clearly seen that the GaN grown in the open window has a significant number of pinholes and dislocations. However none of these are seen in the LEO grown regions above the SiO_2 mask, which suggests that these regions are less defective, showing that LEO can be successfully used to reduce defects in GaN on silicon substrates. By further conducting the growth, the LEO film coalesced as shown in the SEM cross section and surface micrographs in Figures 15(a) and (b). Inverted "V" shaped voids can be observed in the cross section at the junction between two adjacent lateral growth fronts and seamlines can be seen on the surface at that location. Figures 16(a) and (b) show the X-ray diffraction from these coalesced films measured with the X-ray beam perpendicular and parallel to the stripes, respectively. In the "perpendicular beam" or (a) case, two distinct peaks for the GaN are observed. The linewidths of these peaks were on the order of 14 arcmins. By contrast, in the "parallel beam" or (b) case, there is only one peak for GaN but both this peak and the Si substrate peak are significantly broader, which is likely due to residual strain in the epilayer/substrate system in the direction parallel to the stripes. The presence of two distinct GaN peaks in the (a) case suggests that the GaN is likely to

 © 2000 COSiW SEP, Warsaw

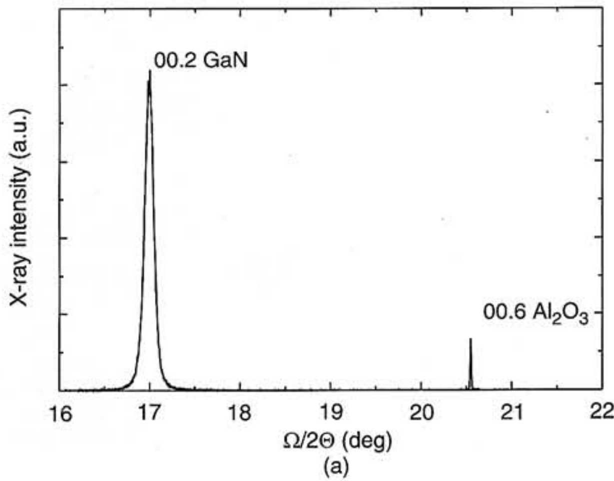

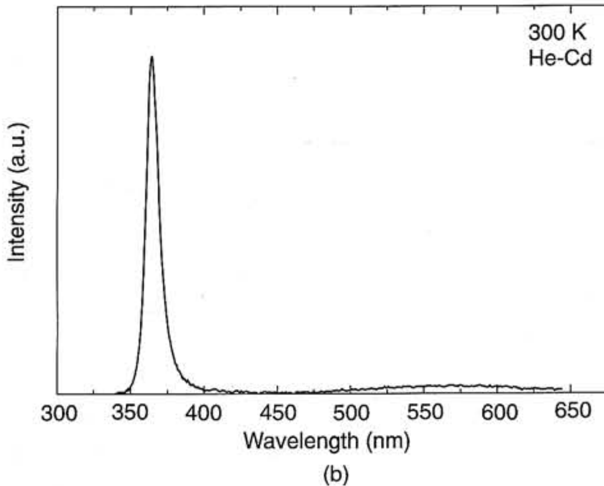

Fig. 12. X-ray diffraction (a) and 300 K PL spectra (b) of a coalesced LEO grown GaN:Si film on (00.1) Al_2O_3 substrate (after Ref. 33).

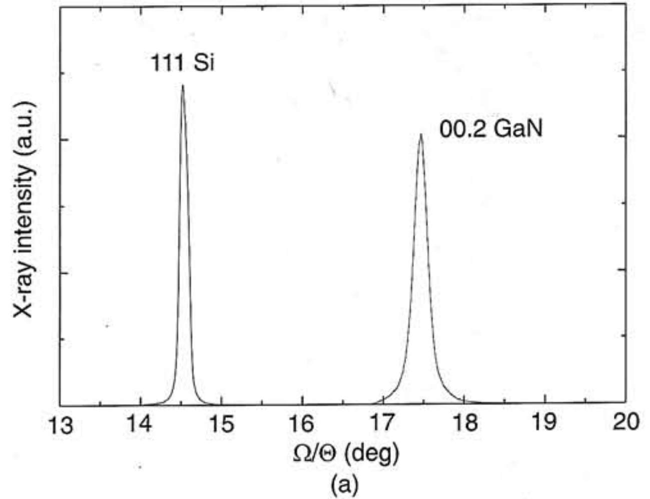

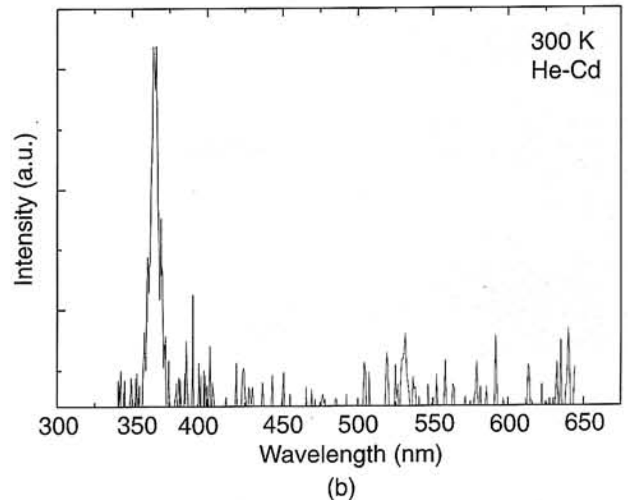

Fig. 13. X-ray diffraction (a) and 300 K PL spectra (b) of a ~ 1.2-μm thick GaN template film on (111) Si substrate (after Ref. 67).

be relaxed in the direction perpendicular to the stripes. Figure 16(c) shows the 300 K photoluminescence spectrum from these films with a linewidth of 90 meV.

8. Processing technologies

The methods of fabrication for III-Nitride devices have always been challenging due to the wide bandgap of the Nitrides which makes them physically and chemically stable and which limits the number of metals that can form good ohmic contacts.

8.1. Etching

Because most devices are grown on sapphire which is insulating, it is not possible to make back electrical contact through the substrate. Etching is therefore a critical and necessary step for the fabrication of most optical and electronic nitride-based devices, in particular to be able to reach both electrical contacts.

Conventional wet chemical etchants have not been successful for use in the fabrication of GaN-based devices due to the low chemical reactivity of the nitrides. Many dry etching techniques have been found to be successful, but ion-induced damage to the etched surface, such as gate recessing for FETs, is unacceptable. Some study has been done using a photoenhanced wet etching technique, which achieved etch rates of 50 nm/min and a surface roughness of 1.5 nm [71]. Unfortunately, this etching method does not seem as efficient for p-type GaN due to the nature of the surface oxidation reaction involved.

A more universal procedure for etching nitride material involves a low ion energy, high density plasma etching technique such as inductively coupled plasma reactive ion etching (RIE), electron cyclotron resonance (ECR), and chemically assisted ion beam etching (CAIBE). These methods offer low energy ion bombardment and smooth, anisotropic etching at high rates. Important parameters in such processes include the chamber pressure, electrode temperature, ion energy, ion density, electromagnet current, gas chemistry, and ion bombardment angle. Several plasma chemistries have been utilised in these high density plasma systems, which provide varying levels of etch rate matching between binary compounds. A few popular chemistries, along with their attributes are listed in Table 9 [72–74].

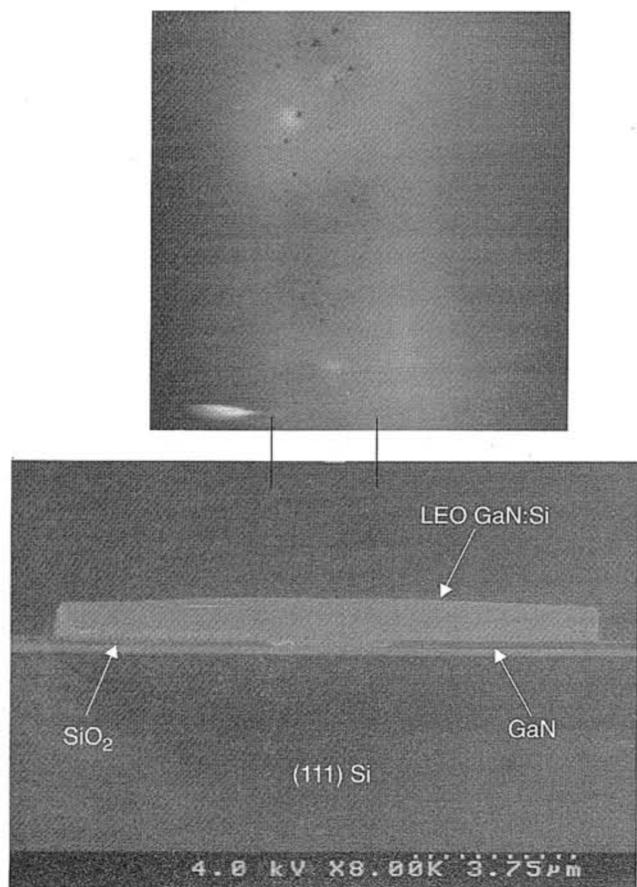

Fig. 14. AFM image of the surface (top) and corresponding SEM micrograph (bottom) of a LEO grown GaN:Si on (111) Si substrate (after Ref. 33).

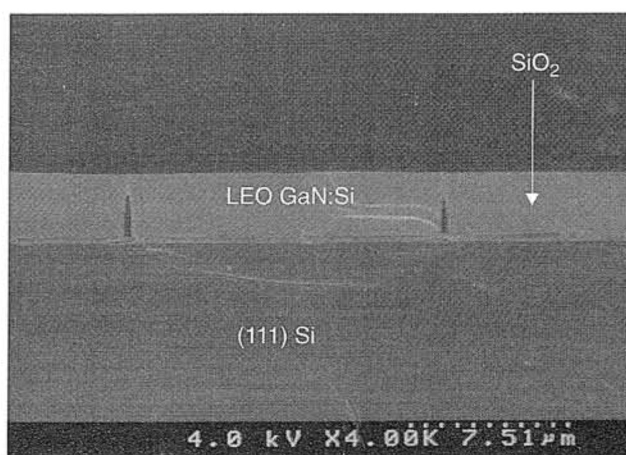

(a)

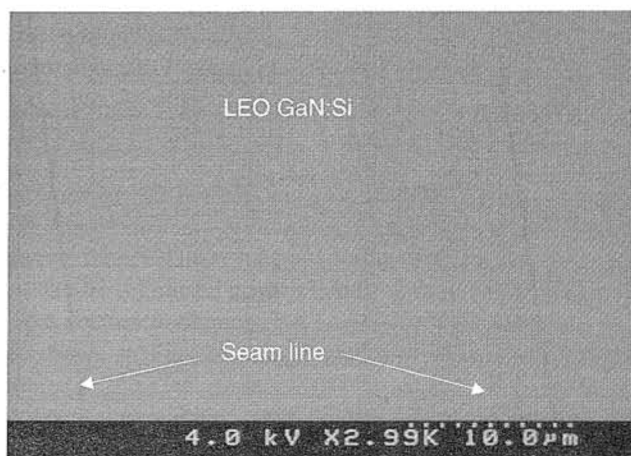

(b)

Fig. 15. SEM micrographs of the cross section (a) and surface (b) of a coalesced LEO grown GaN:Si film on (111) Si substrate (after Ref. 67).

Beside etching the III-Nitride device structure in order to be able to achieve electrical contact, dry etching has also been a promising method to fabricate mirror facets in nitride based lasers.

Indeed, because of the 30-degree rotation between the crystal lattices of III-Nitrides and sapphire substrate, the cleaving planes of the epilayers and substrates do not coincide. Mechanical polishing has been a popular method to achieve mirrors in III-Nitrides, but it is a time-consuming, cumbersome task that rarely achieves the smoothness desired and is not a viable option for mass production.

Dry-etching still is the most popular technique for mirrors in III-Nitrides, because it is easy and fast; although, the cleaving of sapphire after substantial substrate thinning is recently making a growing case. Using dry etching, to attain a smooth vertical mirror, it is important that the etch be non--composition dependent in order to attain similar etch rates for each layer in the laser structure, thus ensuring that there will be no undercutting, protrusions or other significant flaws in the etched vertical plane. Furthermore, with the advances in high density plasma control and directional ion bombardment systems such as CAIBE, the ability to achieve an anisotropic sidewall to the etch is developing rapidly. The standard roughness for these mirrors is about 50 nm. Recent investigations have placed the reflection coefficient at about 15% [75]. Although this value is what is expected for a GaN-air interface, it is not sufficient for high-power, long-lifetime lasers and high reflectivity coatings are usually used in nitride lasers.

Although the dry etching technology of III-Nitride materials has been successfully developed, the results are still not consistent, i.e., there are no standard etch recipes that work universally. This may be due to the fact that the etches are conducted on materials with very dissimilar quality. The future in dry etching of III-Nitrides will be to develop such a standard etch. Important qualities of this ideal etching recipe are high etch rate, minimum structural and electrical damage, and reproducibility.

8.2. Metal contacts

When a metal is applied to a semiconductor, the junction can be ohmic or rectifying, leading to an ohmic or a Schottky contact.

High quality, low-resistance ohmic contacts are a necessary component in the fabrication of nitride based de-

 © 2000 COSiW SEP, Warsaw

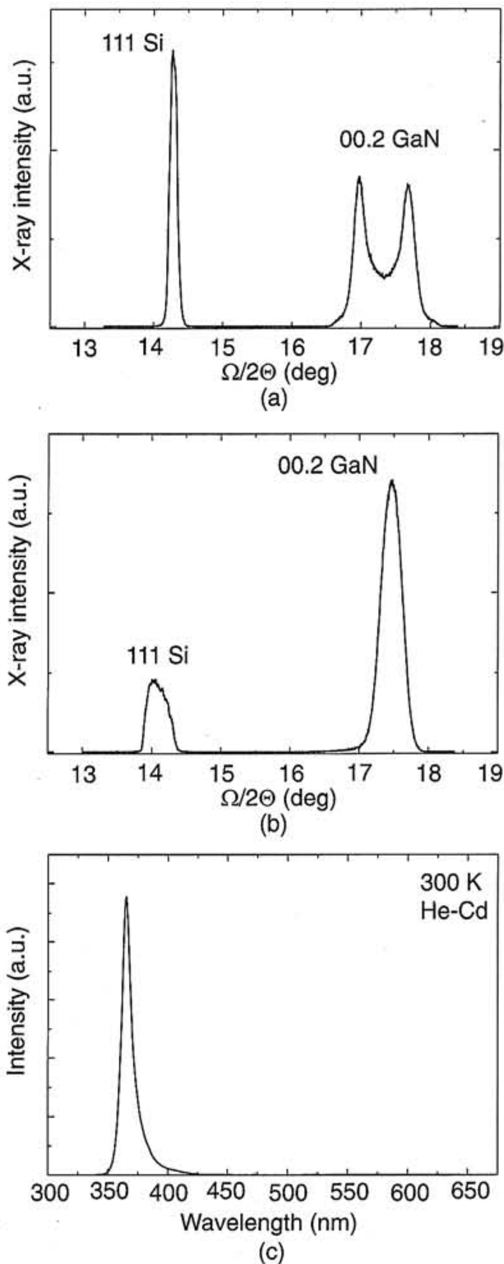

Fig. 16. X-ray diffraction spectra from a coalesced LEO grown GaN:Si film on (111) Si substrate measured with incident the X-ray beam parallel to the stripes (a), perpendicular to the stripes (b), 300 K PL spectrum from a coalesced LEO grown GaN:Si film on (111) Si substrate (c) (after Ref. 67).

vices in order to electrically connect the semiconductor device structure. For example, a high metal-GaN contact resistance would result in a voltage drop and thus hinder the performance of these devices. This is even more important in lasers where high contact resistance is a common cause for the high threshold voltages and Joule heating which leads to early device failure. Low-resistance metal contacts on both p- and n-type III-Nitrides are therefore much sought for, but because of their wide bandgap, not many metals have the adequate work function to form a ohmic contact to III-Nitrides.

Electrical contacts to n-GaN are well-studied, and several different schemes have been found to be acceptable for use. The ohmic/rectifying nature of the metal contact is usually easily predicted because the barrier directly depends on the work function difference between the metal and the semiconductor. Any metal with a work function less than that of n-GaN is expected to form an ohmic contact to it provided that there are no surface states.

However, this is not always the case because of contamination and oxide which can exist on GaN surfaces. These problems can be solved by utilising some surface preparation techniques, which, when performed before the formation of the contact metal, can improve the contact performance greatly. The simplest method of preparing a surface for metal evaporation to prevent either an oxide film or debris on the surface to affect the electrical properties of the junction involves cleaning, including standard degreasing techniques, dipping the wafer into a dilute HCl solution or dry etching. The latter may actually serve a three-fold purpose; cleaning the surface of the wafer by sputtering off any native oxide, increasing the roughness of the surface and increasing the contact area, increasing the number of point defects at the surface due to damage and thus creating an effective n^+ layer near the surface.

All the metals which are in direct contact with the semiconductor surface share the common characteristic of low work function. Bilayers and compound metal structures are carefully designed to utilise the electrical and mechanical properties of the alloys that are formed during their heating, as well as to provide a top contact metal layer on the surface for wire bonding purposes. Ohmic contacts can be fabricated very effectively using either a low or high temperature post-evaporation annealing. For example at low temperatures, between 400 to 600°C, Ti acts as an oxygen getter, thus reducing the native oxide on the surface, and an Ti-Al intermetallic phase can form and come into contact with the GaN [76]. Aluminum alone, when heated, could also reduce the native oxide, but is limited by the formation of an AlN layer which accompanies excessive annealing. At higher temperatures (> 900°C), if Ti is used as the first contact material, it has been found that TiN will form at the junction of Ti and GaN [77]. This semi-metal, coupled with the nitrogen vacancies near the interface, forms a very low resistance ohmic contact.

Some common contact schemes used in attaining ohmic contacts to n-GaN are such as RIE damage and post-evaporation annealing (rapid thermal annealing or RTA) are indicated in Table 10 [76–80].

While much work has been done to achieve the realisation of a low resistance, ohmic contact to n-GaN, the investigation into the p-GaN metal contact has been limited and sparse. Ni/Au is the most popular bilayer contact scheme used currently in many blue laser designs. It is chosen due to the large work function of Ni, as well as its ability to adhere well to the surface of the material, and the thermal quality and wire bonding continuity that Au offers. Some insight into the mechanisms behind p-GaN interaction and

Table 9. Plasma etch chemistries, their etch rates for various Nitride-based binary compounds and advantages.

Chemistry	Material	Typical etch rate*	Comments
$SiCl_4/Ar$	GaN AlN InN	2850 Å/min 1245 Å/min 3840 Å/min	This chemistry does not allow for the incorporation of hydrogen. At high temp, 170°C, InN and GaN are both ~ 2350 Å/min
$Cl_2/H_2/Ar$	GaN AlN InN InGaN	4800 Å/min 1150 Å/min 5850 Å/min 3200 Å/min	If H_2 is used the etch rates will be slightly higher, but the different compounds will have more unequal rates of etching.
$CH_4/H_2/Ar$	GaN AlN InN InGAN	.1450 Å/min 1150 Å/min 3300 Å/min 3500 Å/min	CH_4 provides polymer sidewall protection for additional anisotropy, but coats the chamber walls and requires extensive conditioning of chamber.
$Cl_2/BCl_3/Ar$	GaN AlN InN	6000 Å/min 5000 Å/min 6500 Å/min	Does not introduce hydrogen. Very fast etch rates for all three binary compounds.

* Etch rates are dependent on recipe parameters. These numbers should only be viewed as a comparison index for within each chemistry

Ni/Au is necessary to determine whether this is indeed the best choice of material. Many different metals with high work functions have been investigated, and a definite correlation between resistivity and work function was demonstrated [81]. Unfortunately, no work has been published yet which illustrates achievement of the low contact resistance required for blue lasers.

Also essential for many devices are Schottky contacts. For example, Schottky barrier photodiodes and JFETs make use of a high-quality rectifying contact to the semiconductor material. Thermal stability is very important for use in high temperature applications. A short list of some tested materials is shown in Table 11 [82,83].

Low resistance ohmic metal contacts to n-type GaN are well developed and do not need much work in the near future. By contrast, ohmic metal contacts to p-type GaN will receive the most attention. The development of Schottky contacts is still immature. Although interest in this area of research is growing, the contact quality must be improved to support the evolution of current devices.

9. Devices

9.1. Electronic devices

Not only are III-Nitrides suitable for optical devices, they are also promising for electronic devices. Unlike optical devices which make use of $Ga_{1-x}In_xN$ alloys to span the visible optical spectrum, electronic devices use $Al_xGa_{1-x}N$ compounds to make use of the large breakdown voltage, high saturation velocity and thermal conductivity of these materials, in order to fabricate devices which could operate at high-frequency, high power and high temperature. AlN is also a promising insulating material as an alternative to oxides [84].

Four figures of merit are generally used to characterise materials for electronic devices.

- The Johnson figure of merit (JFM) is related to the electronic properties of materials. It characterises the frequency-power trade-off, since high frequency usually requires small device dimension while high power need large device size. JFM is calculated as $JFM = \left(E_b V_s / 2\pi\right)^2$, where E_m is the breakdown voltage, V_s is the saturation velocity.
- The Keyes figure of merit (KFM) is related to the material thermal properties. It characterizes the device size and thermal resistance trade-off, and is calculated as $KFM = \delta_T \left(c V_s / 2\pi\varepsilon_r\right)^{1/2}$, where δ_T is the thermal conductivity of the materials, c is the speed of light, and ε_r is the material dielectric constant.
- The Baliga figure of merit (BFM) addresses conduction losses of low frequency power devices and is calculated

Table 10. A list of ohmic metal contact schemes for use with n-GaN.

Nitride material	Contact material	Resistivity
n-GaN	Nd/Al Ti/Au Pd/Al Ti/Al Al Ti/Al./Ni/Au	9.8×10^{-6} Ω/cm^2 (RTA) 3×10^{-6} Ω/cm^2 1.2×10^{-5} Ω/cm^2 (650°C anneal) 5×10^{-5} Ω/cm^2 (600°C anneal) 8×10^{-6} Ω/cm^2 8.9×10^{-8} Ω/cm^2 (RTA+RIE)

Table 11. A list of contact material, built in potential, barrier height, and ideality factor for Schottky contacts to p-GaN.

Nitride material	Contact material	Built in potential	Barrier height	Ideality factor
p-GaN	Cr Au Ni Ag Pb	0.52 V 1.00 V 1.12 V	0.55 eV 1.03 eV 1.13 eV 0.82 eV 0.73 eV	1.05 1.15 1.17 1.01 1.01

 © 2000 COSiW SEP, Warsaw

as $BFM = \varepsilon\mu E_b^2$, where μ is the carrier mobility in the material.

- The Baliga high-frequency figure of merit (BHFM) addresses switching losses of high-frequency power devices, due to charging and discharging, and is calculated as $BHFM = \varepsilon\mu E_b^3$.

These figures of merit allow give some type of comparison between III-Nitrides and other semiconductors for high-frequency, high-power and high-temperature electronic devices. The values are generally normalised to Si. The values for the JFM and KFM are listed in Tables 12 and 13, respectively. From these tables, it can be seen that GaN, AlN are promising materials for high-performance electronic devices.

Table 12. Comparison of the Johnson figures of merit of different materials.

Material	E_b (V/cm)	V_s (cm/s)	$[(E_bV_s)/\pi]^2$ (V^2/s^2)	Ratio to silicon
Si	3×10^5	1.0×10^7	9.1×10^{23}	1.0
GaAs	4×10^5	2.0×10^7	64.8×10^{23}	7.1
GaN	50×10^5	2.7×10^7	18466×10^{23}	2029
6H-SiC	40×10^5	2.0×10^7	6485×10^{23}	712
3C-SiC	40×10^5	2.0×10^7	6485×10^{23}	712
Diamond	100×10^5	2.7×10^7	73863×10^{23}	8117

To date, III-Nitrides-based metal-insulator, metal--semiconductor and heterojunction field effect transistors (MISFET, MESFET, HFET), as well as GaN/ SiC hybrid heterojunction bipolar transistors have been demonstrated. More recently, AlGaN/GaN modulation doped field effect transistors (MODFET) with cut-off frequency as high as 50 GHz and maximum frequency of 92 GHz have been achieved. These devices were able to operate up to 500°C.

Piezoelectric effects between AlGaN and GaN interfaces has been investigated to generate two-dimensional electron gas at the interface without doping of the barrier. HFETs based on this piezoelectric effect has been demonstrated with cut-off frequency as high as 62 GHz and a maximum frequency up to 140 GHz.

In spite of these successes, the development of III-Nitride based electronic devices is still in its infancy. Much research work will be necessary to enhance the performance and reliability of these devices and fulfil the expected potential of III-Nitrides for high frequency, high power and high temperature electronic devices. This will mostly rely on improvement of the material quality and metal contact technology.

9.2. Ultraviolet photodetectors: a survey

There are many types of types of photodetectors. Photoconductors, metal-semiconductor-metal (MSM), Schottky barrier, and photovoltaic diodes are the most common. They are all considered useful for certain applications. The advantages and disadvantages of each type of photodetectors are summarised in Table 14 [11].

The development of photodetectors based on III-Nitride material began with the most simple device design, the photoconductor. This device required no p-GaN layer to operate, and therefore simplified not only the growth demands, but also the fabrication steps because etching steps were not needed to define the device or contact two electrically different types of GaN layers. Both single stripe devices and interdigitated contact designs have been pioneered to explore the limits of current responsivity, noise equivalent power (NEP), temporal response, and rejection ratio. The current responsivity depends on two main factors: the quantum efficiency, η, and the photoconductive gain, G, which are assumed to be constant over the volume of the device. The quantum efficiency is a measure of how well the input radiation is coupled to the electrical area of the photodetector. It is usually defined as the number of electron-hole pairs generated for each incident photon.

Table 13. Comparison of the Keyes figures of merit of different materials.

Material	σ_T (300 K) (W/cm)	V_s (cm/s)	ε_r	$\sigma_T(V_s/\varepsilon_r)^{1/2}$ ($W/cm^{1/2}s^{1/2}$)	Ratio to silicon
Si	1.5	1.0×10^7	11.8	13.8×10^2	1.0
GaAs	0.5	2.0×10^7	12.8	6.25×10^2	0.45
GaN	1.3	2.7×10^7	9	22.5×10^2	1.6
6H-SiC	5.0	2.0×10^7	9.7	71.8×10^2	5.2
3C-SiC	5.0	2.0×10^7	9.7	71.8×10^2	5.2
Diamond	20.0	2.7×10^7	5.5	443.1×10^2	32.1

Table 14. Comparison of different types of UV photodetectors.

Photodetector type	Advantages	Disadvantages	Challenges
Photoconductors	• Easy to fabricate • Internal photoelectric gain	• Low speed • Large dark current • Large Johnson noise	• Interdigitated patterns require enhanced resolution
p-n or p-i-n photodiodes	• Low or zero dark current • High-speed • High impedance (good for FPA readout circuitry) • Compatible with planar processing technology (for FPA) • For p-i-n photodiodes, easy optimization of quantum efficiency and speed with i-layer	• Speed is limited by minority carrier diffusion time and storage time • Speed and quantum efficiency trade-off	• Etching is necessary to expose various layers • Ohmic contacts necessary to both n- and p-type material
Schottky photodiodes	• High efficiency • High speed • Easy to fabricate	• Require high absorption coefficient • No-sharp cut-off (below bandgap res.) • Front side illumination needed	• Schottky contact is needed

Photoconductive gain is a concept that simplifies the idea of a photoconductive phenomenon. The responsivity is significantly higher for devices utilising the closely spaced interdigitated contacts due to the photoconductive gain mechanism exploited in the design. The noise equivalent power (NEP) is also a parameter used to measure the performance of a detector. It is the ratio of the current noise to the responsivity of the device. Another popular metric used to quantify the performance of a UV detector is the UV-to-visible rejection ratio, which is the ratio of the photoresponse of UV light to the photoresponse of visible light. These parameters are outlined with their appropriate values in Table 15 for several types of photodetectors reported in the literature [85–94].

The characteristics of current photoconductor devices include very fast response detectors [87], $Al_xGa_{1-x}N$ detectors over the entire range ($0 \leq x \leq 1$) (see subsection 9.3) [85], and demonstration of gain mechanism in an MSM detector by using interdigitated contact design with a gain over 3000 A/W [88]. GaN detector arrays have also been demonstrated. The kinetics of photoconductivity have also been investigated in GaN photodetectors [95].

Schottky diodes are the most simple detectors to fabricate and are capable of being extremely fast. Several groups have combined efforts to develop Schottky photodetectors with high responsivity and low NEP [89]. They have also fabricated the first GaN-based photodetector grown on a Si substrate rather than the popular c-plane sapphire substrate [90]. Recently, high speed Schottky based MSM photodetectors have been demonstrated and their characteristics will be discussed in subsection 9.6 [96].

The last part of Table 15 highlights the reported results for p-n and p-i-n photodiodes [97]. To date, all the p-n junctions in the photodiodes were formed using GaN, leading to a cut-off wavelength of 365 nm corresponding to the bandgap of GaN. The temporal response for these detector designs led to carrier lifetimes as low as 20 ns, with very low NEP, good responsivities (0.10–0.14 A/W) and rejection ratios of about three orders of magnitude. The latest advancement in this field was a GaN p-i-n photodiode which not only has a high responsivity of 0.15 A/W, but made a jump from the typical rejection ratio of 10^3 to a much larger 10^6, as discussed in subsection 9.4 [94]. Another recent development in this field is the demonstration of AlGaN p-i-n ultraviolet photodiodes for the first time, which will be briefly discussed in subsection 9.5 [98].

The progression to faster response, higher rejection of visible light, lower noise interference, and better response are all indicative of not only improved designs, but also a continued increase in the quality of material. III-Nitride based UV photodetectors remain a very promising field for research and development for the future. In the following few subsections, the characteristics of $Al_xGa_{1-x}N$ photoconductors for the entire alloy compositional range ($0 \leq x \leq 1$), GaN p-i-n photodiodes with high rejection ratio, $Al_xGa_{1-x}N$ p-i-n photodiodes and high speed GaN Schottky based MSM photodetectors will be described in more details.

9.3. Characterisation of $Al_xGa_{1-x}N$ ultraviolet photodetectors with $0 \leq x \leq 1$

The $Al_xGa_{1-x}N$ epitaxial layers on (00.1) sapphire substrates used for the demonstration of UV photodetectors in the entire alloy compositional range were grown on basal plane sapphire by MOCVD (Fig. 6) [49]. The thickness of the films was ~ 1 μm. All the samples were transparent, smooth, free of cracks, and highly resistive. The geometry of the photodetectors was very simple, consisting of two-indium stripe contacts with a separation of 1 mm and a length of 4 mm. The contacts were blocked from illumination so that the influence of any possible photoelectric ef-

 © 2000 COSiW SEP, Warsaw

Table 15. Major accomplishments in Nitride based detectors: photoconductors (PC), MSM and Schottky diodes, and photovoltaic detectors (PD).

Detector	R (A/W)	Gη	NEP (W)	τ	Rejection ratio	Research group
GaN PC	125	600		20 ns		Boston University
$Al_xGa_{1-x}N$	18–300	64–150	$<10^{-8}$	1–2 ms	10^3	APA Optics
AlN, GaN PC $Al_xGa_{1-x}N$ (0<x<1) PC	>10 (single stripe)		$<10^{-9}$	<3 ms	10^3	CQD-Northwestern University
GaN MSM	0.3				$>10^2$	University of Texas-Austin
GaN MSM	3200 (interdigitated)			300 μs	$>10^2$	NASA-Goddard Space Flight Center
n-GaN Schottky PD	0.18	0.65	5×10^{-9}	120 ns	10	APA Optics Texas Tech. Univ.
n-GaN Schottky on Si (111)	0.10		4×10^{-9}		10^2	APA Optics, Texas Tech. Univ., NC State Univ.
GaN p-i-n PD	0.11	0.48		8.2 μs		SVT Associates, Univ of Minnesota
GaN p-π-n PD	0.10		4×10^{-11}	18 ns	10^3	APA Optics, Texas Tech. Univ.
AlGaN/GaN p-i-n PD	0.14	0.5	8×10^{-12}	12 ns	10^3	University of Illinois-Wright Laboratory
GaN p-i-n PD	0.15	0.5		2.5 μs	10^6	CQD-Northwestern University

fect would be minimised. Optical response measurements were conducted using a synchronous detection scheme utilising a Xe lamp chopped at 14 Hz and focused into a monochromator at the exit of which the photoconductors were placed. The spectrum of the Xe lamp was measured using a calibrated Si detector. The rest of the biasing circuit was contained in an electrically isolated box to eliminate any electromagnetic interference. The photoconductor was in series with a load resistor, RL. Because of the large resistance of the photoconductors, they were operated in the constant-voltage mode.

The responsivity linearly increases with bias voltage. It eventually saturates at high voltages due to the sweep out effect. The normalised spectral response from these $Al_xGa_{1-x}N$ is shown in Fig. 17. It demonstrates for the first time that a continuously tunable cutoff wavelength can be achieved from 200 to 365 nm by adjusting the alloy composition.

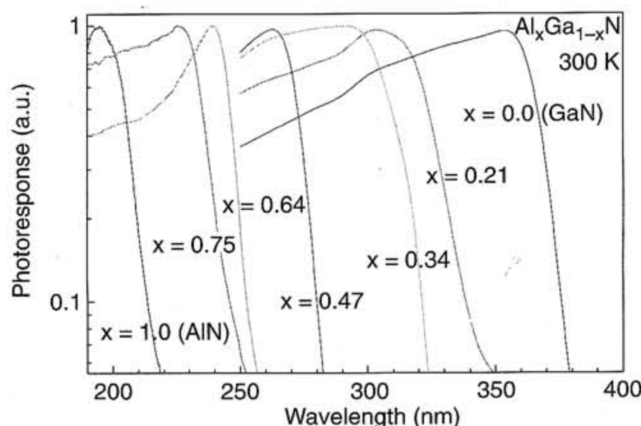

Fig. 17. Normalised 300 K spectral response from $Al_xGa_{1-x}N$ photoconductors (after Ref. 68).

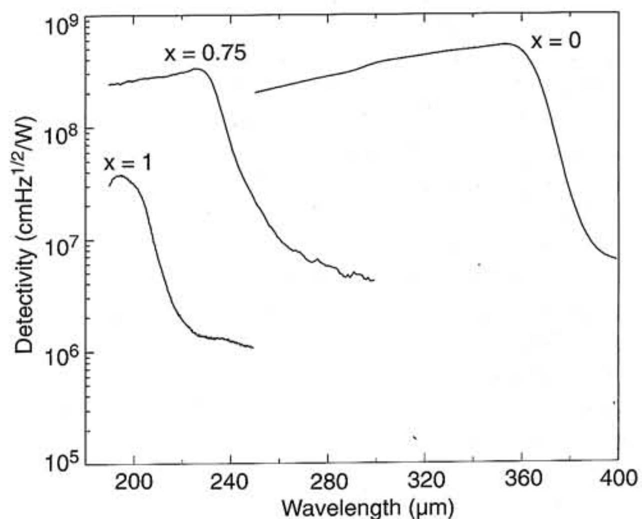

Fig. 18. Detectivity of $Al_xGa_{1-x}N$ ($0 \le x \le 1$) photodetectors at a modulating frequency of 14 Hz (after Ref. 86).

Noise measurements were taken with a SR760 FFT Spectrum Analyser (Stanford Research Systems) at room temperature using the same setup and conditions as for photoresponse measurements with the exception of the placement of the sample. During the noise measurements, the sample was kept inside the electrical isolation box with the rest of the biasing circuit so that it would be shielded from any light. The noise was found to decrease with increasing frequency, while levelling off around 30 kHz and remaining flat at high frequencies. For low Al-composition $Al_xGa_{1-x}N$ photodetectors, the high-frequency noise is limited by Johnson noise. The noise of the AlN photodetectors is higher than their Johnson noise. Based on the

Table 16. The detectivity and majority carrier lifetime of $Al_xGa_{1-x}N$ ($0 \le x \le 1$) photoconductors.

Detector active layer $Al_xGa_{1-x}N$	λ_c (nm)	D^*_{peak} (cmHz$^{1/2}$/W)	τ_{eff} (ms)
x = 0	365	5.54×10^8	6
x = 0.75	230	3.33×10^8	25
x = 1	200	3.81×10^7	35

responsivity and noise measurements, the detectivities were calculated using the following equation

$$D^* = \frac{R_i(A\Delta f)^{1/2}}{i_n}$$

where R_i is the responsivity, $i_n/\sqrt{\Delta f}$ is the power spectral density of the noise signal, and A is the area of the detector. Figure 18 shows the detectivity of $Al_xGa_{1-x}N$ ($0 \le x \le 1$) UV photodetectors at a modulating frequency of 14 Hz. The peak detectivities are in the range of 3.81×10^7–5.5×10^8 cmHz$^{1/2}$/W, as displayed in Table 16 with the corresponding Al content and cutoff wavelength. Below the bandgap wavelength, the detectivity linearly increases with increasing wavelength, whereas near the bandgap, it exhibits a sharply decreasing responsivity. This indicates that the detector has high quantum efficiency up to the cut-off wavelength.

In an attempt to correlate the detectivity with the carrier lifetime the kinetics of photoconductivity was done by measuring the frequency-dependent photoresponse, as done in Ref. 95. The responsivities for all $Al_xGa_{1-x}N$ photodetectors decrease dramatically with increasing frequency at low frequencies and reach a constant at high frequencies. Figure 19 shows a typical frequency-dependent photoresponse of an $Al_xGa_{1-x}N$ photodetector. Taking the chopper modulation into consideration, which can be approximated as a square modulation, the frequency-dependent response can be described by the following equation

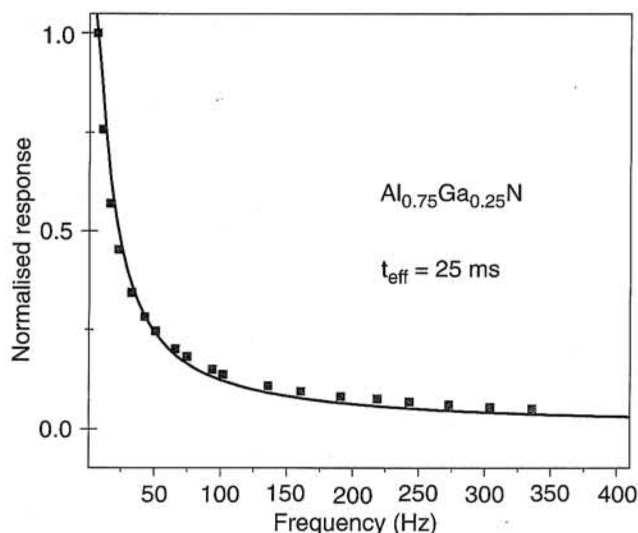

Fig. 19. Frequency-dependent response of $Al_{0.75}Ga_{0.25}N$ photodetector (after Ref. 86).

$$R_v(f) = \left(\frac{q\lambda\eta}{hc}\right)R_L\left(\frac{\mu_e\tau_{eff}V_b}{\ell^2}\right)\tanh\left(\frac{1}{4\tau_{eff}f}\right)$$

where η is the quantum efficiency, μ_e is the electron mobility, λ is the wavelength of the incident light, ℓ is the electrode spacing, V_b is the DC bias voltage across the photoconductor, f is the modulation frequency and τ_{eff} is the effective majority carrier lifetime. The latter, obtained from the frequency-dependent photoresponse, is between 6 ms and 35 ms, as shown in Table 16. It increases with increasing Al-composition in $Al_xGa_{1-x}N$ materials. This may be attributed to the influence of deep-level traps in higher Al-composition samples. One mechanism that has been proposed to occur in high Al-content ternary materials involves the appearance of a trapping layer as the Al concentration is increased [99].

9.4. GaN p-i-n photodiodes with high visible-to-ultraviolet rejection ratio

A typical GaN p-i-n ultraviolet photodiode characterised in this subsection is shown in Fig. 20 and was grown by low pressure MOCVD [94]. It consists of a 2000 Å Mg-doped GaN layer ($p \sim 10^{17}$ cm^{-3}), on a 1000 Å undoped GaN layer on a 1 μm n-type Si-doped GaN ($n \sim 5\times10^{18}$ cm^{-3}) on (00.1) sapphire substrate. After post-growth annealing to achieve low-resistivity p-type GaN:Mg, the surface of the sample was partially removed using ECR-RF dry etching until the n-type GaN was exposed to form 400×400 μm square mesa structures. Ni/Au and Ti/Au metals were evaporated onto the p-type and n-type GaN, respectively. The spectral responses of photodiodes were measured using a Xe arc lamp, a monochromator, an optical chopper, and a lock-in amplifier in a synchronous detection scheme. The sample was uniformly illuminated from the front side. To obtain the absolute spectral responsivity, the power of the Xe lamp as a function of wavelength was factored out after measuring its spectrum using a calibrated Si detector.

The absolute spectral responsivity of the GaN p-i-n photodiode without bias is plotted in Fig. 21 (solid line). The device area used in the calculations was the exposed surface area of the mesa (400–150 μm^2). A peak responsivity of 0.15 A/W at 363 nm was achieved. The theoretical current responsivity for a p-i-n photodiode is given by

$$R_i(\lambda) = \frac{q\lambda}{hc}\eta$$

 © 2000 COSiW SEP, Warsaw

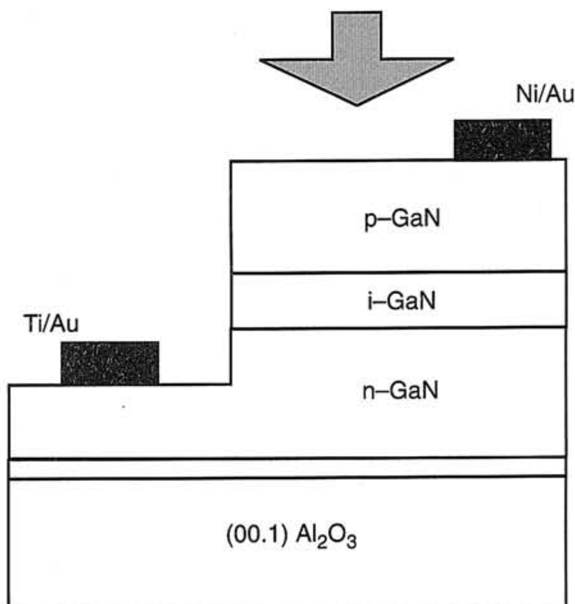

Fig. 20. Schematic of a typical photodiode mesa structure (after Ref. 94).

where λ is the photon wavelength and η is the external quantum efficiency [100]. This external quantum efficiency includes the internal quantum efficiency and reflectivity losses. Using the value obtained for the responsivity at 363 nm, an external quantum efficiency of η ~ 0.51 is estimated for these p-i-n photodiodes.

Using the Xe lamp, it was not possible to detect any photogenerated signal for wavelengths longer than about 390 nm. A high power argon laser (514 nm) was then used to obtain a photoresponse in the visible spectral region and the value of the responsivity is shown in Fig. 21 as a triangle. By dividing the values of the responsivity at 363 nm and at 514 nm, a value of 10^6 was obtained for the UV-to--visible rejection ratio, which is about three orders of magnitude higher than other reports on III-Nitride based UV

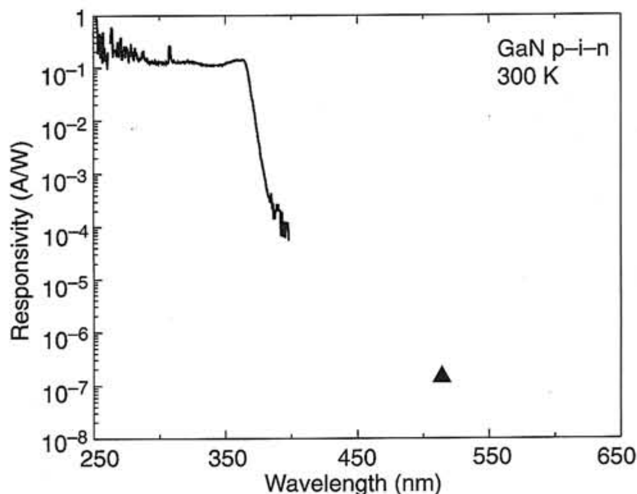

Fig. 21. Room temperature spectral response of a typical GaN p-i-n photodiode. The responsivity at 514 nm was measured using a high power argon laser, while the rest of the spectrum was measured using a Xe lamp (after Ref. 94).

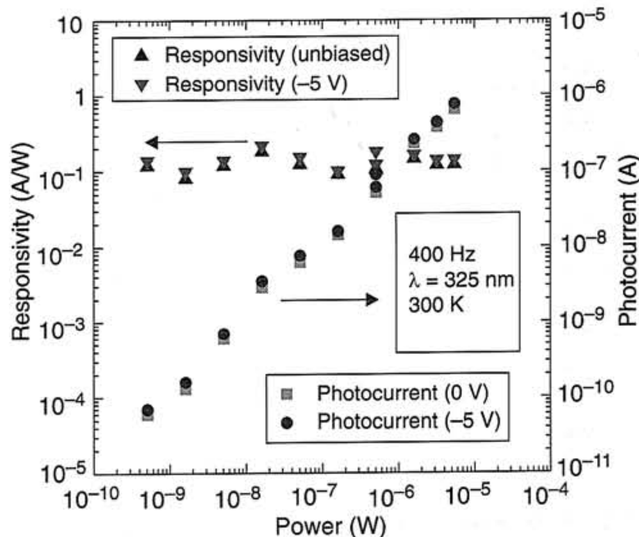

Fig. 22. Responsivity and photocurrent measured with increasing optical power (after Ref. 94).

photodetectors. Because GaN has a wide bandgap, crystal defects or impurities in the material may easily create energy levels within the gap. These levels form recombination centres that harm the performance of UV photodetectors, in particular their visible blindness. The improvement of the visible blindness for our GaN based UV detectors can be partly attributed to better control of the material growth technology (reduction of impurity and defect densities). Further improvements in rejection ratio may be achieved by optimising the device geometry and structure design.

The responsivity and photocurrent of the photodiode is shown in Fig. 22 for optical power levels across many orders of magnitude. The photocurrent increases linearly for increasing power, thus yielding a constant responsivity. The current-voltage curve of one of these diodes is shown in the inset of Fig. 23. The current at reverse bias is three orders of magnitude less than the current for the same voltage at forward bias. The resistance plotted with respect to bias voltage, as seen in Fig. 23, indicates the turn on voltage at ~ 3 V with a dramatic decrease in resistance of seven orders of

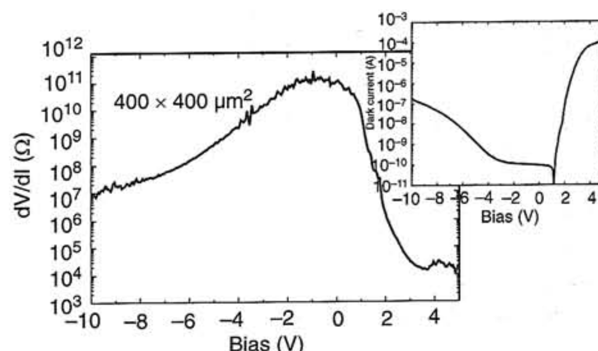

Fig. 23. Room temperature resistance-and current-voltage curves of a p-i-n photodiode (after Ref. 94).

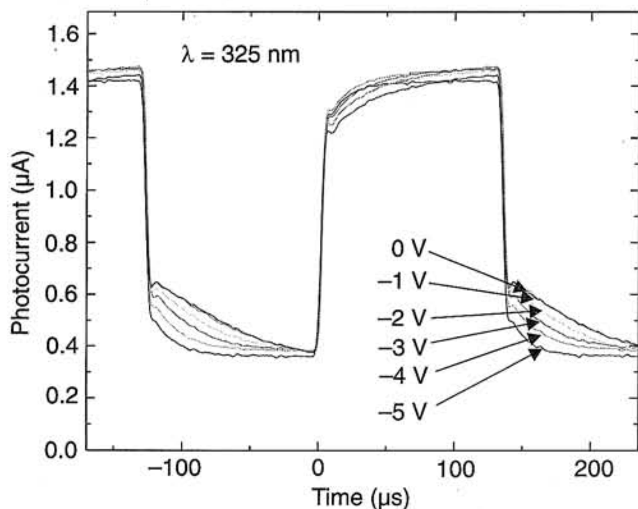

Fig. 24. The temporal response display of rise and fall times for various voltage biases (after Ref. 94).

magnitude. This plot also shows the zero bias resistance of $10^{11}\ \Omega$.

The rise and fall times, which indicate at what speed a device is able to operate, are examined for various bias voltages. The square wave of period 250 μs is created by the optical chopper spinning at a frequency of 4 kHz. One limitation is in the current amplifier itself, which contributes a rise and fall time of 5 μs for a gain of 10^6. As seen in Fig. 24, as the negative bias is increased from 0 to –5 volts the response of the diode is noticeably faster. Both the rise and fall times respond to the higher negative bias and attain the switched level more quickly than their lower biased counterparts. A more accurate estimate of the rise and fall times for this detector was taken with a pulsed nitrogen laser as the optical source so that a chopper and current amplifier, which introduce additional response delays to the measurement, would not be necessary. Figure 25 shows a fall time speed of the photodiode of about 2.5 μsec. This response time, although not as limited as if using the previous setup, is believed to still be limited by the measurement apparatus. The increase in response speed with an increase in voltage bias, as seen in Fig. 24, suggests that the speed of these GaN p-i-n photodiodes is limited by the RC time constant of the detection circuit, where R is the total resistance and C is mainly the capacitance of the depletion layer in the diode. Indeed, the RC time constant can be reduced by increasing the reverse bias, which extends the depletion layer, and thus reduces the capacitance C. A rough estimate of the RC time constant yields a value of $\tau_{RC} \sim 1.4$ μs, assuming the following parameters for GaN; $R \sim 1\times10^4\ \Omega$, $\varepsilon = 10.4\ \varepsilon_0$ (E//c); W = 0.1 μm and A = $(400\ \mu m)^2$ for the width and area of the depletion layer respectively. This value of τ_{RC} is on the same order as our estimate of the response speed from Fig. 25.

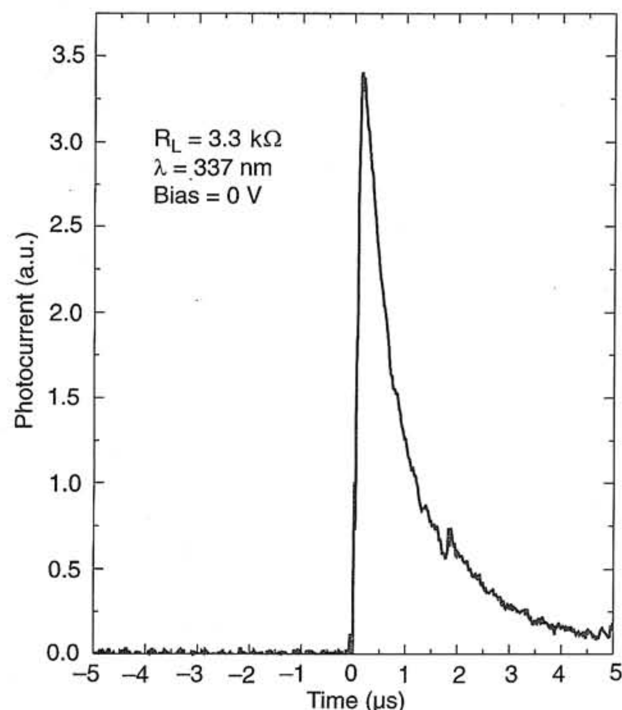

Fig. 25. The temporal response with a pulsed nitrogen laser as the optical source (after Ref. 94).

9.5. $Al_xGa_{1-x}N$ p–i–n ultraviolet photodiodes

Recently, $Al_xGa_{1-x}N$ p-i-n ultraviolet photodiodes grown by low pressure MOCVD have been demonstrated for the first time [98]. They consist of a 2000 Å Mg-doped $Al_xGa_{1-x}N$ layer, on a 1000 Å undoped $Al_xGa_{1-x}N$ layer on a 1 μm n-type Si-doped $Al_xGa_{1-x}N$ on (00.1) sapphire substrate. After post-growth annealing to achieve low-resistivity p-type $Al_xGa_{1-x}N$:Mg, the surface of the sample was partially removed using ECR-RF dry etching until the n-type $Al_xGa_{1-x}N$ was exposed to form 400×400 μm square mesa structures. Ni/Au and Ti/Au metals were evaporated onto the p-type and n-type $Al_xGa_{1-x}N$ respectively. The

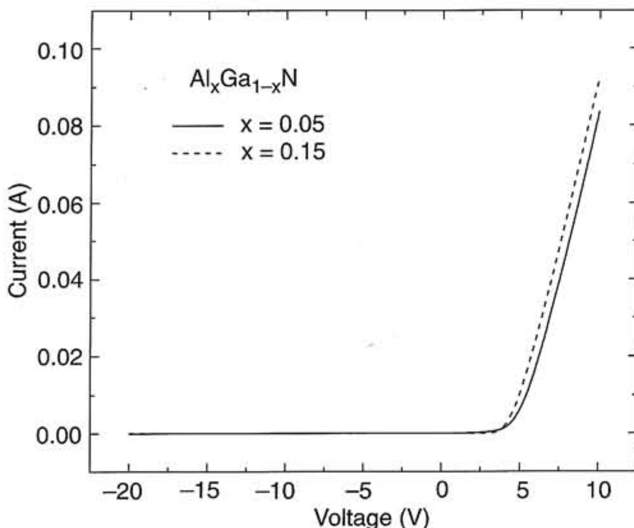

Fig. 26. Room temperature current-voltage characteristics of $Al_xGa_{1-x}N$ p-i-n diodes with different Al concentrations.

 © 2000 COSiW SEP, Warsaw

measurements were conducted using the same experimental setup as described previously for GaN p-i-n photodiodes.

The current-voltage characteristics of two chosen diodes, with ~ 5% and ~ 15% Al concentration, are shown in Fig. 26. The room temperature spectral response yielded peak responsivities at 350 and 335 nm for the two diodes tested, as shown in Fig. 27. These detectors were solar blind with a visible-to-ultraviolet rejection of 10^4 was observed. The photoresponse was linear for more than 4 decades of incident optical power.

These preliminary results represent the first ever reported $Al_xGa_{1-x}N$ p-i-n UV photodiodes and are most promising for solar blind UV photodetectors. More research work is being conducted in improving these devices.

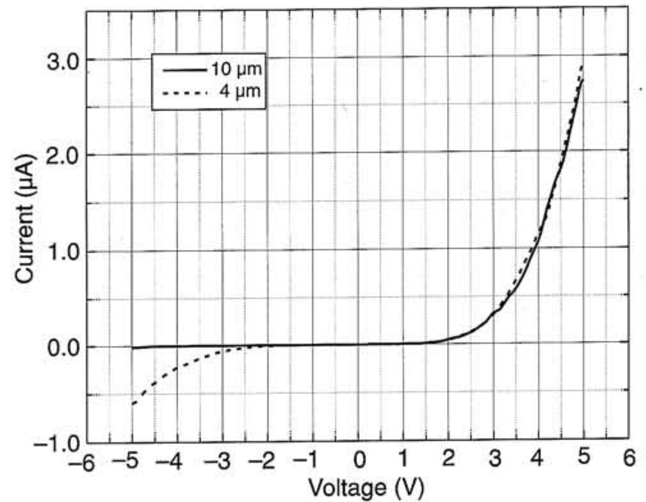

Fig. 28 Current-voltage curve for a GaN Schottky MSM photodetector for two different finger spacing.

9.6. High speed Schottky based metal-semiconductor-metal UV photodetectors

Recently, high speed, Schottky metal-semiconductor-metal ultraviolet photodetectors exhibiting a sharp wavelength cutoff have been demonstrated [96]. The devices consisted of a high quality, undoped GaN films grown by low pressure MOCVD on basal plane sapphire substrates [94]. High quality Pt/Au Schottky contacts were deposited and interdigitated finger patterns were fabricated using standard photolithography techniques.

The current-voltage (I-V) curve for the MSM device is shown in Fig. 28 for two different finger spacings. The asymmetry of the curve is due to the different sizes of the two metal contacts.

The spectral response of the detector was measured using a Xe arc lamp as described in previous subsections and is shown in Fig. 29. The peak responsivity occurs at 359 nm and a very abrupt cutoff is observed above this wavelength, with the signal dropping by more than 3 orders of magnitude until it was no longer measurable. The response with respect to optical power was measured using a He-Cd laser (325 nm) and is shown in Fig. 30. It demonstrates a slightly sub-linear dependence of the response to incident optical power of about $P^{0.9}$. This slight diversion from the norm is most likely due to the heating of the detector at higher power levels.

Most importantly, the most promising feature of this device was its high speed. Initial tests confirmed that the device lifetime was limited by the RC time constant of the instruments and measurement techniques used, in terms of load resistance and capacitance of the electrical wires. The contribution from the load resistance can be factored out as shown in Fig. 31. By extrapolating the curve, it was possible to determine the response speed of the detector to be less than 10 ns, the highest reported for a GaN Schottky MSM photodiode. By factoring out the capacitance of the measurement circuit, the response speed of the device should be even lower.

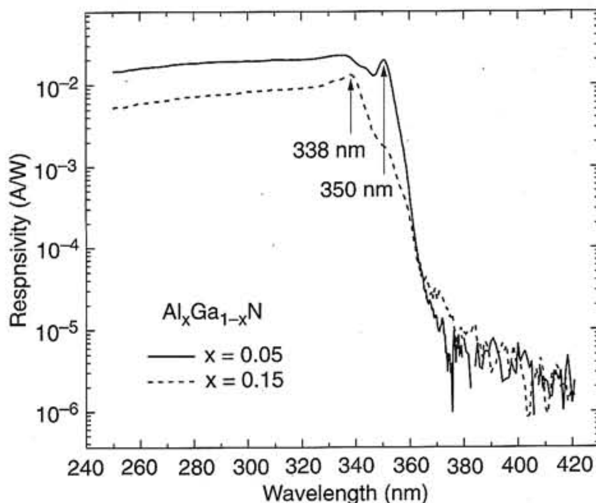

Fig. 27. Room temperature, zero bias spectral response of $Al_xGa_{1-x}N$ p-i-n photodiodes with different Al concentrations.

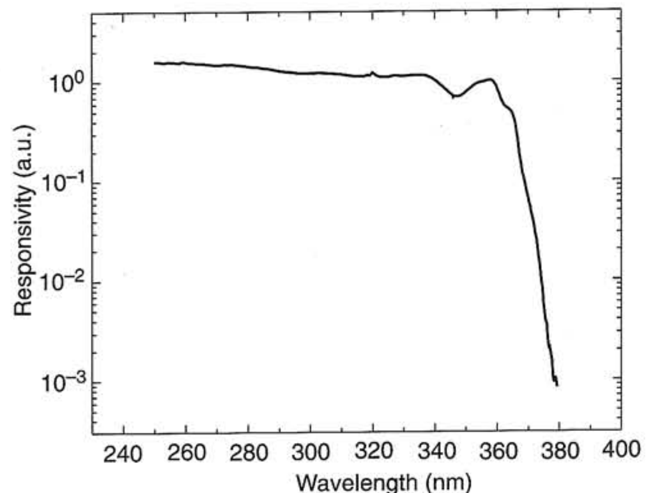

Fig. 29. Room temperature spectral responsivity of the Schottky MSM photodetector.

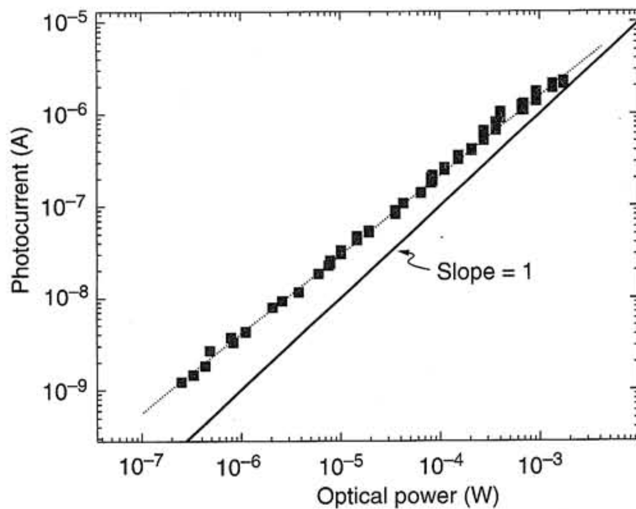

Fig. 30. The responsivity vs. optical power curve.

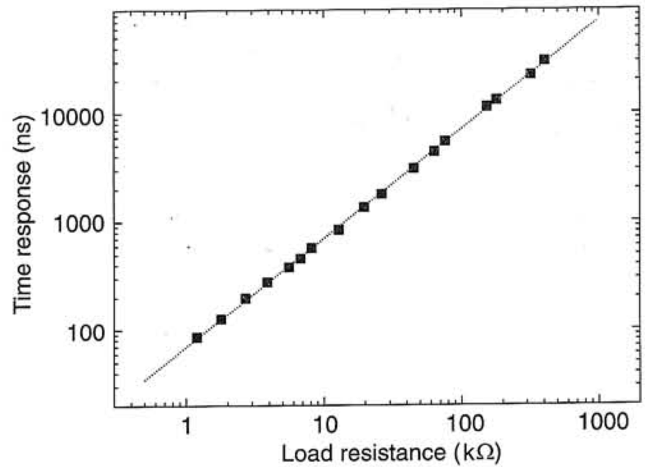

Fig. 31. Device time response versus load resistance plot.

9.7. Visible light emitting diodes

To generate visible light using III-Nitride materials, one has to use $Ga_{1-x}In_xN$ alloys in the active layer. The first generation of blue and blue/green LEDs were fabricated from GaInN/AlGaN double-heterostructures (DH) [101]. Although these provided high optical output, higher than 1 candela (cd), they had a broad spectrum with linewidths typically ~ 70 nm, while the emission spectrum ranged from the violet to the yellow-orange spectral range, making the output appear "whitish-blue" to the human eye. Greatly improved LED performance, in terms of both colour purity and intensity, have been achieved using single quantum-well (SQW) structures [102–104]. The emission peak linewidths for blue LEDs (450 nm) have been reduced to 20 nm, with brightness as high as 2 cd. Green LEDs (520 nm) exhibited an emission peak linewidth of 30 nm and luminous intensity of 12 cd. The latest record has been achieved by using strained single quantum wells of $Ga_{1-x}In_xN$. Violet (405 nm), blue (450 nm) and green (520 nm) LEDs has been demonstrated with efficiencies of 9.2%, 8.7% and 6.3% respectively (see Table 17). These LEDs give better performance than those made from other materials and join the mainstream of LED evolution as shown in Table 18. White LED have also been demonstrated by combining a blue nitride LED with a phosphorescent coating of the LED packaging. All of these LEDs are now commercially available.

Table 17. Nichia LED performances at forward current I_f = 20 mA [102–104] (predicted lifetime ~ 60 000 hrs [105]).

Colour	λ_{peak} (nm)	Peak FWHM (nm)	P_{out} (mW)	η (%)
Violet	405	20	5.8	9.2
Blue	450	20	5	9.1
Green	520	30	3	6.3
Yellow	590	90	0.5	1.2

In addition to these high brightness LEDs, devices with longer emission peak wavelengths, up to 600 nm (orange), have been achieved by increasing the indium composition (Table 17) [105]. However, the performance of these devices are not as satisfactory because the quality of GaInN tends to deteriorate for higher indium compositions due to the dissociation of GaInN at high temperatures, and because of the higher lattice and thermal mismatch between the well and the barrier layers [106].

Despite the successful commercialisation of III-Nitride based LEDs, there remain some important issues.

First, is the reliability of the devices. These LEDs are still fragile and require careful handling. They can be easily damaged by reverse bias greater than 5 V or forward current higher than 100 mA. This is surprising because III-Nitrides are expected to have high breakdown voltages. An improper doping profile or high background carrier concentration in GaInN could be the cause of failure at high reverse bias or large forward current.

Second, is their thermal handling capability. The recommended operation temperature is 80°C to avoid early degradation of the devices. Ideally, III-Nitrides based devices are suitable for much higher temperature operation because of their thermal properties. The unusual low operation temperature could be due to the high defect density in the materials and the thermal instability of GaInN active layer.

Third, is the price. Commercial III-Nitride based LEDs cost more than ~ US$ 6 a piece, which is still too high for large volume applications.

9.8. Violet-blue laser diodes: a survey

The realisation of III-Nitride based laser diodes has eluded the research community for many years. It is only after thorough development of the material, processing and device fabrication technology that such lasers have been made possible.

© 2000 COSiW SEP, Warsaw

Table 18. Comparison of visible III-Nitride LEDs and those fabricated from other semiconductor materials.

Color	Material	Peak wavelength (nm)	Luminous intensity (mcd)	Output power (μW)	External quantum efficiency (%)
Green	AlInGaP	570	1000	400	1.0
	GaP	555	100	40	0.1
	ZnTeSe*	512	400	1300	5.3
	InGaN	520	12000	3000	6.3
Blue	SiC	470	20	20	0.04
	ZnCdSe*	489	700	327	1.3
	InGaN	450	2500	5000	9.1

* At forward current $I_f = 10$ mA, all others $I_f = 20$ mA

There has been outstanding success in GaN-based blue laser diodes in the past few years. To date, nine research groups worldwide have demonstrated GaInN/GaN multiple quantum well based violet-blue laser diodes and some of the device characteristics are summarised in Table 19. Blue laser diodes operating at room temperature and in continuous wave mode with a projected lifetime of 20000 hours have been demonstrated and are nearing commercialisation. Most of the recent nitride lasers share the following characteristics.:

- The active layer consists of a $Ga_{1-x}In_xN/Ga_{1-y}In_yN$ or GaInN/GaN multi-quantum well (MQW) with an emission peak ranging from 400 to 430 nm.
- The MQW is not uniform, but has a quantum dot-like structure. These quantum dots are formed most likely because of indium composition fluctuation and segregation.
- Laser performances are enhanced when Si doping the wells and barriers of the MQW.
- The general structure of the laser consists of a separate confinement heterostructure, using AlGaN as the cladding layers, although there has been report of Al-free III-Nitride lasers which will be discussed in the next two subsections [42].
- The p-type contact layer has a hole concentration in the range of 10^{18} cm^{-3}.

The dislocation density in early generation of III-Nitride based lasers is measured to be higher than 10^7 cm^{-2}, which led to very short lifetime and low output power. It is only recently that much higher output power and longer lifetime have been achieved by reducing the dislocation density through lateral epitaxial overgrowth

Table 19. Current GaN-based blue laser diode players.

Research group	Date	Structure	Operation mode	Threshold	λ_0 (nm) $\Delta\lambda$ (nm)	Output power	Fabrication	Lifetime
Nichia	Nov, 1995	GaInN MQW on sapphire	Pulsed@RT	1.7A@34V 4 kA/cm^2	4.17 1.6	215 mW@ 2.3 A&34V	RIE etching for mirrors with HR coating (60–70%)	Not tested (>24 hrs)
Meijo University	Mar, 1996	GaInN SQW-SCH on sapphire	Pulsed@RT	16 V 2.9 kA/cm^2	376 0.15	Not given	RIE etching for mirrors without coating	Not given
Toshiba	Sept, 1996	GaInN MQW on sapphire	Pulsed@RT	5 A@20 V 50 kA/cm^2	417.5 0.15	Not given	Cleaved along <1120> on c-sapphire	Not given
Cree	1997	no details						
Fujitsu	July, 1997	10 GaInN MQW on SiC	Pulsed@RT(%)	500 mA@22 V 12 kA/cm^2	405–425	80 mW	HR coated	Not given
UCSB	Sept, 1997	GaInN MQW on sapphire	Pulsed, RT	50 V 12.7 kA/cm^2	420	Not given	RIE	Not given
Xerox	Oct, 1997	10 GaInN MQW on sapphire	Pulsed@RT 400 ns @1 kHz	25 kA/cm^2	422–432	Not given	Dry etching	Not given
Sony		5 GaInN MQW on sapphire	Pulsed, RT, 500 ns, 1 kHz	9.5 kA/cm^2	417.5	<0.2 nm	Cleaving	Not given
Northwestern University	Dec, 1997	GaInN MQW	Pulsed, CW, RT	1.4 kA/cm^2@77K	405–410	2 mW/facets (Pulsed)	Mechanical polishing	140 hrs@RT
Nichia	Oct, 1997	GaInN MQW	CW@RT	16 mA 1.5 kA/cm^2	390–420	2 mW	RIE mirror with HR coating	10000 hrs@RT

(LEO). From the above discussion, it can be seen that there are still many fundamental issues that need to be addressed.

First, there is currently no real understanding of the lasing mechanism in III-Nitride lasers. There are experimental evidences that recombination in the MQW active layer is enhanced in these laser diodes by self-formed quantum-dot like structures, or by localisation of excitons by potential fluctuation [107–111]. Theoretical work is necessary to study how these structures are affecting material and modal gain [112], recombination efficiency, emission wavelength (tunable by adjusting the dot or potential feature sizes), and how lasing can be improved by intentionally control the formation of such structures.

Secondly, the mechanism for the formation of the afore-mentioned quantum-dot structure or local potentials is also unknown. Is it due to the intrinsic nature of GaInN ternary alloys since compositional modulation due to phase separation would be energetically favoured in this material system? [39]. Or is it due to compressive strain introduced by lattice mismatch? The understanding of the mechanism would inevitably lead to better devices.

The effect of doping in III-Nitride based lasers is not entirely clear. Generally lasers have intrinsic active layers in order to enhance carrier diffusion and reduce free carrier absorption in the active layer. However, Si doping in III-Nitride lasers enhances the laser diode performance [109]. It is believed that the doping effectively screens the piezoelectric field in the MQW active region [113].

The p-type doping needs to be increased in order to minimise device resistance. Searching for other dopants seems hopeless because of the deep-level nature of acceptor dopants in III-Nitrides, which may be an intrinsic nature of wide bandgap nitride materials, just like ZnSe-based materials. However, new doping schemes such as piezoelectric effect, which can enhance the ionisation of impurities by built-in electrical field, or tunneling-assisted carrier injection should be studied.

Finally, the failure mechanisms in III-Nitride lasers need to be determined and minimised. Potential causes of failure include heat generation due to high series resistance, dislocations and other threading defects, as well as optical damage due to reabsorption of stimulated emission at defects which are formed during growth [114]. Reduction of defects is now rapidly being conducted through lateral epitaxy overgrowth [115]. With the progress of bulk GaN growth either by high-pressure technique or hydride VPE or LEO grown, homoepitaxy of III-Nitride devices may be soon available.

9.9. Low temperature operation of GaInN/GaN multi-quantum well laser diodes

In this subsection and the following one, the characteristics of Al-free GaInN/GaN multi-quantum well lasers at low temperature and room temperature will be discussed.

The epitaxial layers were grown on (00.1) sapphire substrates by low pressure MOCVD [24,42,94] Fig. 32(a) shows a schematic diagram of the laser structure grown, which consisted of a 3 μm-thick Si-doped GaN ($n \sim 2\times10^{18}$ cm^{-3}); followed by a 10 period 33 Å $Ga_{0.89}In_{0.11}N$/66 Å GaN multiple quantum wells; and a 0.25 μm-thick Mg-doped GaN contact layer ($p \sim 2\times10^{17}$ cm^{-3}).

Figure 33 shows the room temperature photoluminescence and optical pumping from the MQW structure described above capped with only a thin GaN layer as measured using a He-Cd laser and a pulsed nitrogen laser respectively. Stimulated emission was collected from a bar with mechanically polished edges and was observed for pumping densities higher than a threshold estimated at 100 kW/cm^2. The peak position was 401 nm and its width of ~ 1 nm (resolution of the measurement equipment).

Light emitting devices were fabricated using ECR-RF dry etching, as well as Ti/Au and Ni/Au metal contacts on the n-type and p-type GaN, respectively, as shown in Fig. 32(b). Figure 34 shows the room temperature electroluminescence spectrum for increasing injected currents under continuous wave operation with the light collected from the

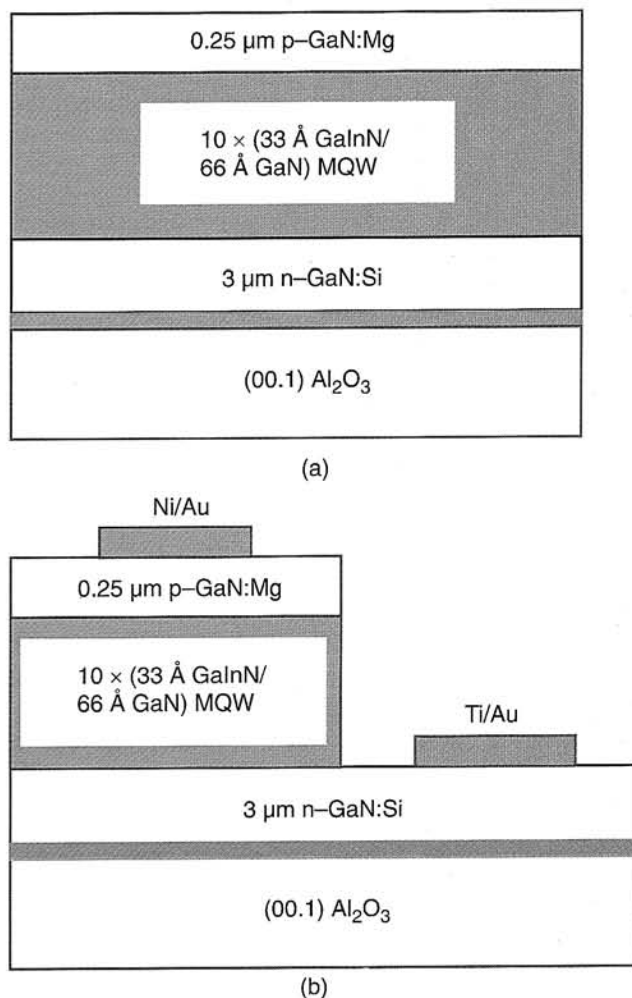

Fig. 32. Schematic diagram of a 10 period 33 Å $Ga_{0.89}In_{0.11}N$/66 Å GaN MQW laser structure (a), and cross-section of a processed broad-area 33 Å $Ga_{0.89}In_{0.11}N$/ 66 Å GaN MQW laser with 100 μm-wide metal contacts (b).

 © 2000 COSiW SEP, Warsaw

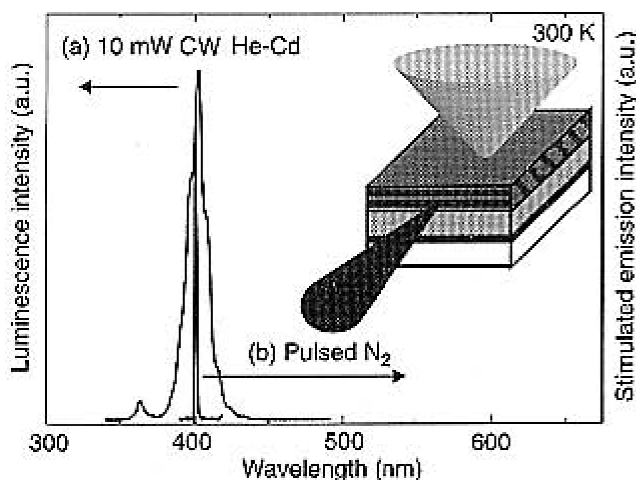

Fig. 33. Room temperature photoluminescence (a) and stimulated emission from a 10 period 33 Å $Ga_{0.89}In_{0.11}N$/66 Å GaN MQW (b).

back of the sample. An intense electroluminescence peak at ~ 416 nm could be observed.

The 79 K photoluminescence from the wells in the light emitter is shown as curve a in Fig. 35. In order to be able to detect photoluminescence from the MQW, the top p-type GaN:Mg layer was partially removed by dry etching to allow penetration of the laser beam. The spectrum exhibited a small peak at ~ 384 nm and an intense peak at 410 nm. The full width at half maximum of the peak at 410 nm is ~ 11 nm. This width and the presence of two peaks in the spectrum strongly suggests that there is some degree of phase separation in the MQW structure, leading to localised regions – e.g. quantum dots – which are In rich and others regions which are In deficient. Curve b in Fig. 35 shows the 79 K electroluminescence spectrum of this laser structure, exhibiting a peak at ~ 403 nm.

Broad-area lasers with 100-µm wide stripes were fabricated. Mirror facets were mechanically polished for various cavity lengths from 700 µm to 1800 µm. The rough-

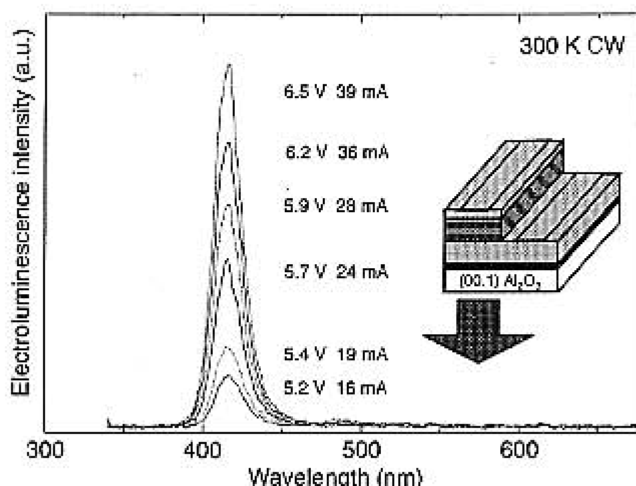

Fig. 34. Room temperature continuous wave electroluminescence from a 10 period 33 Å $Ga_{0.89}In_{0.11}N$/66 Å GaN MQW laser diode.

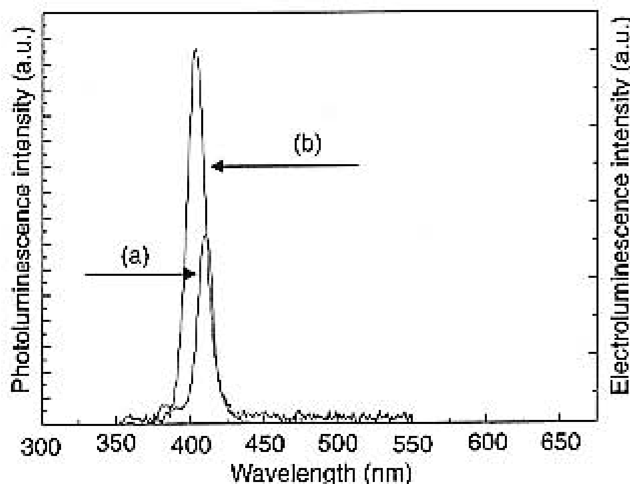

Fig. 35. 79 K photoluminescence from a GaInN/GaN MQW (a) and 79 K electroluminescence from a laser diode with the same active region (b).

ness of the facet surface was in the range of 50 nm. No antireflection or high-reflection coatings were applied on the mirror facets. The laser diodes were bonded with indium to copper heatsinks. Light-current characteristics were recorded in pulse operation (pulse width 2-6 µs, repetition rate 200 Hz) using a silicon detector. From the current versus voltage (I-V) curve, the series resistance of the laser (L ~ 1800 µm) was estimated to be 13 Ω at 300 K (turn-on voltage ~ 3.6 V) and 14 Ω (turn on voltage ~ 6 V) at 79 K, as shown in Fig. 36. When decreasing the sample temperature from 300 to 79 K, the resistivity of the p-type GaN:Mg is expected to increase drastically, by

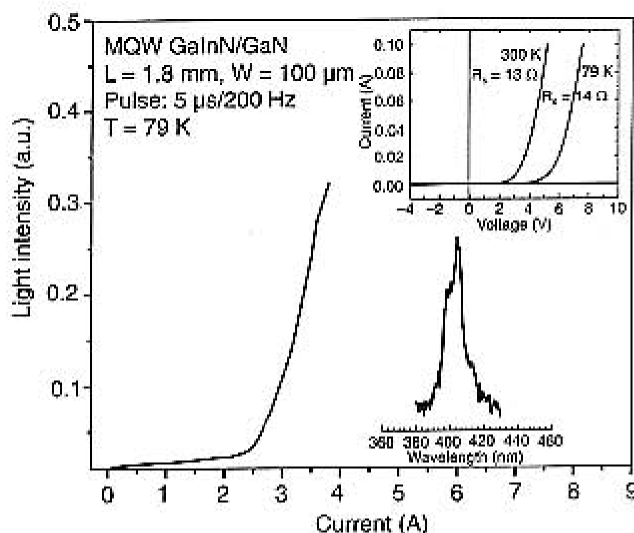

Fig. 36. Output power versus injection current for a MQW GaInN/GaN 405 nm uncoated diode laser measured at 79 K (pulse operation: 5 µs-200 Hz) with cavity length of 1800 µm and 100 µm-wide aperture. Inset: Current-voltage characteristics of the laser diode with series resistance of 13 Ω at 300 K and 14 Ω at 79 K. Spectrum of the laser diode slightly above threshold.

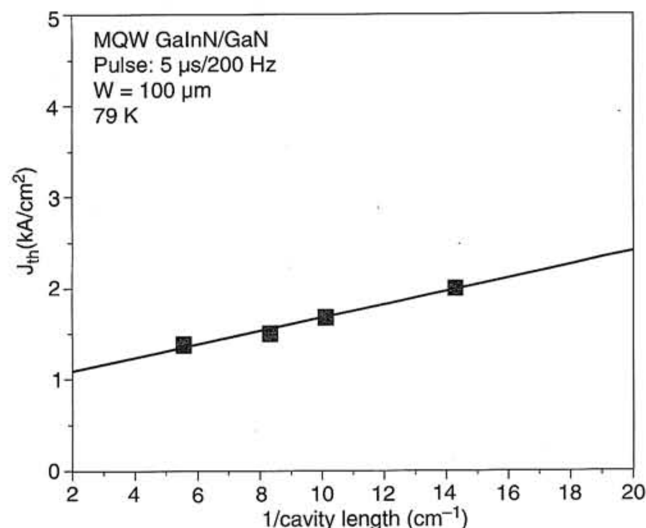

Fig. 37. Threshold current density vs. inverse cavity length for 100 μm wide GaInN/GaN MQW lasers at 79 K.

at least two orders of magnitude, as a result of the relatively high activation energy of Mg levels in GaN [32,116]. The fact that the series resistance does not increase significantly in these diodes may be directly due to the small thickness of the GaN:Mg layer, to the absence of AlGaN cladding layers or to higher p-type doping of GaN:Mg which results in lower device resistances [32].

Figure 36 illustrates the light output power versus injection current of an uncoated 1800 μm-long laser at 79 K. Stimulated emission was observed at currents of 2.5 A, which corresponds to a threshold current density of 1.4 kA/cm^2. Because the laser stripes used in this study are 100 μm wide, the lasing action may occur in filament and the threshold current density may be locally higher than the value measured above. The voltage of this laser at threshold was 25 V. The peak wavelength of the measured lasers was 405 nm at 3.4 A as shown in Fig. 36. At currents lower than 4 A, no degradation was observed for these diodes under pulse operation. The threshold current density for several lasers of different cavity length was measured and the results are plotted in Fig. 37.

Table 20 summarises the emission wavelengths from the same laser wafer measured at low temperature (79 K) by photoluminescence, electroluminescence and current injection stimulated emission. A good agreement between the electroluminescence and current injection stimulated emission is observed.

Table 20. Emission wavelengths from GaInN/GaN MQW and lasers using different measurement techniques at low temperature (79 K).

Measurement technique	Emission wavelength
Photoluminescence	410 ± 2 nm
Electroluminescence	403 ± 2 nm
Current injection stimulated emission	405 ± 2 nm

9.10. Room temperature operation of GaInN/GaN multi-quantum well lasers

MQW lasers comprising 10–15 periods of 33 Å GaInN/66 Å GaN superlattices were grown on (00.1) sapphire substrates in the same manner described in the previous section and characterised at room temperature. A 0.25-μm thick Mg-doped GaN was used as the p-type contact layer. Mirror facets were mechanically polished for various cavity lengths from 650 μm to 1800 μm. The roughness of the mirror facet was estimated to be in the range of 50 nm from SEM measurement. No mirror coating was applied to the facet surfaces.

The P-I and I-V curves of a typical laser diode with 100 μm width and 1200 μm cavity length under pulse operation (5 μs/200 Hz) are shown in Fig. 38(a). The P-I curve of the laser diode at CW operation is shown in Fig. 38(b). The I-V curve (dotted line) in a forward direction shows the series resistance as low as 6 Ω and turn-on voltage of 6.2 V. As shown in Fig. 38(a), the laser showed a sudden increase in the slope of optical output power vs. injection current curve by one or two orders of magnitude at around I ~ 300 mA, indicating the onset of a laser operation. The laser in pulse-operation showed saturation of output power around 2 mW of output power [Fig. 38(a)]. The emission spectrum above and below threshold measured by an interferometer is shown in Fig. 39. For these measurements, the interferometer designed for this wavelength range (400–500 nm) was not available and the one designed for longer wavelengths (> 0.8 μm) was thus used. Because the latter's fibre and other optical components are very lossy in the 400–500 nm wavelength range, an estimation of the collection efficiency indicates that only less than 0.3% of light will actually be analysed. The actual stimulated emission signal-to-noise ratio should thus be 300 times higher than what was measured. As shown in Fig. 39(d), there was a significant background noise even at zero injection current due to this low collection efficiency (low signal to noise ratio). Nevertheless, Fabry-Perot-like peaks could be observed above threshold, as shown in Figs. 39(a), (b), and (c) which correspond to the spectra measured at I = 500, 900 and 1000 mA, respectively. In these measurements, the actual Fabry-Perot longitudinal modes could not be resolved in the monochromator used because of its limited resolution (~ 0.1 nm) at this wavelength (~ 410 nm) and since the Fabry-Perot mode spacing was expected to be only about 0.03 nm for GaN lasers with cavity length of 1000 μm (Fig. 40).

The presence of stimulated emission in these devices was further confirmed by measurements of far-field patterns and polarisation properties of the emitted beam, as these properties have very distinctive features between

 © 2000 COSiW SEP, Warsaw

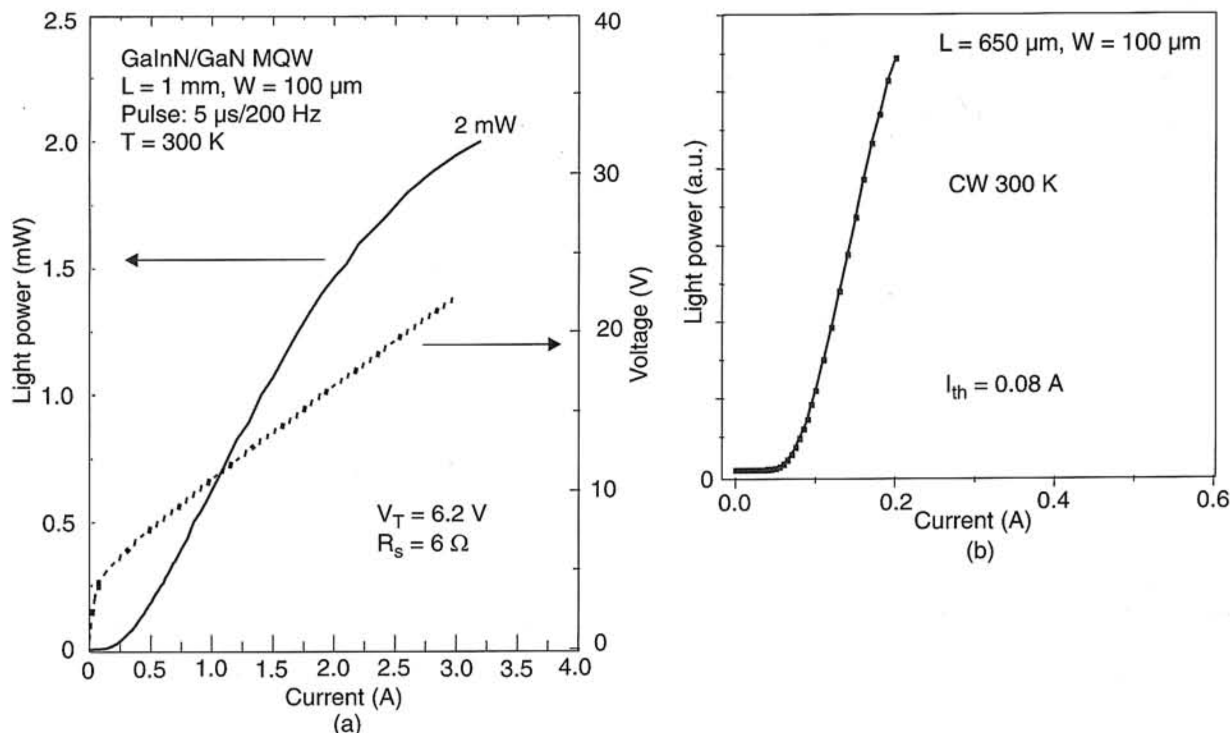

Fig. 38. Light – current (P-I) and voltage-current (I-V) characteristics of GaInN/GaN MQW laser under pulse operation at 300 K (a), light – current (P-I) curve for GaInN/GaN MQW laser under CW operation at 300 K (L = 650 µm, W = 100 µm) (b).

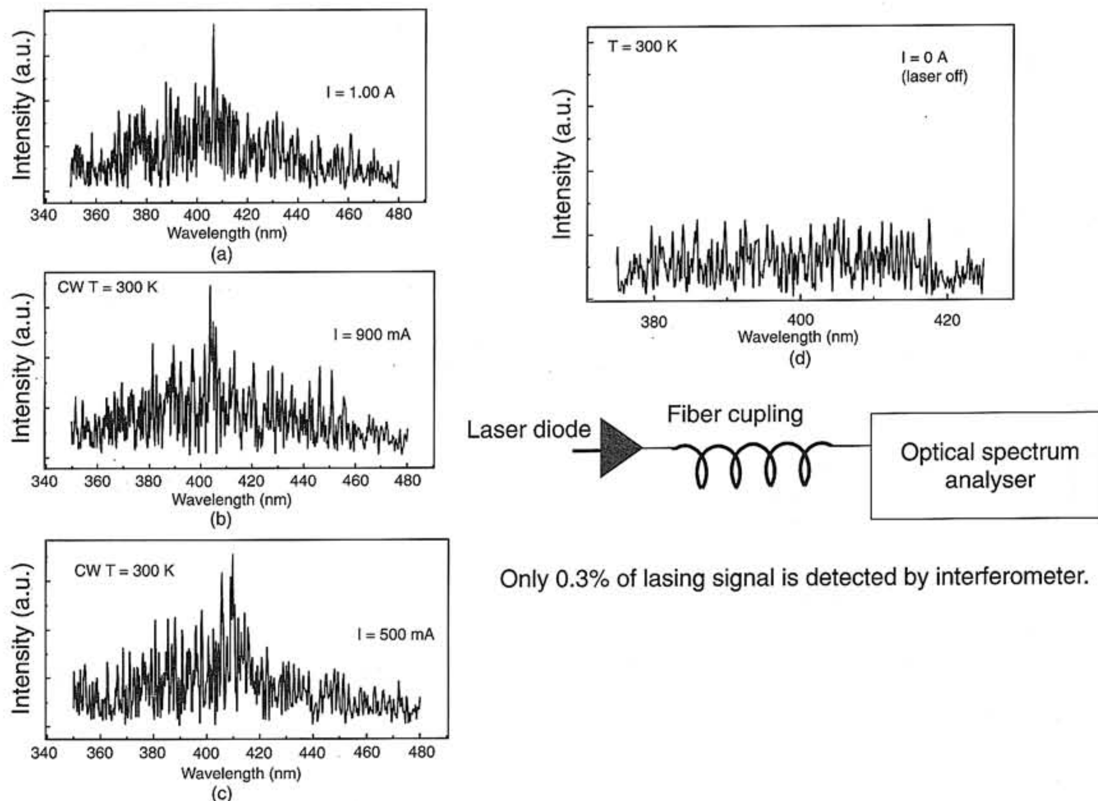

Fig. 39. Emission spectrum of laser diode (L = 1200 µm, W = 100 µm) at 300 K, measured by interferometer at I = 1 A (a), I = 900 mA (b), I = 500 mA (c), and I = 0 (d).

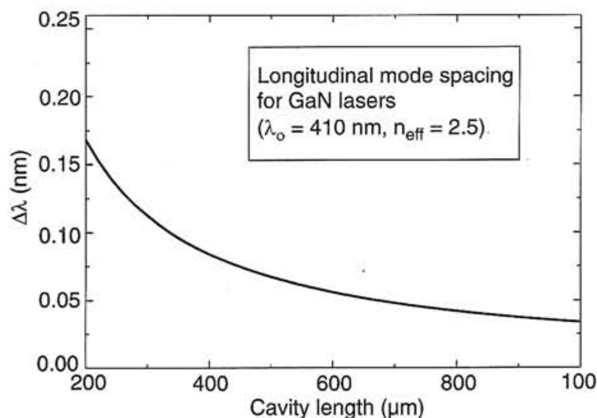

Fig. 40. The longitudinal mode spacing $\Delta\lambda$ of GaInN lasers ($\lambda_o = 410$ nm, $n_{eff} = 2.5$).

stimulated and spontaneous emission beams. Figure 41 shows far-field patterns with beam divergence of 13° and 20° for parallel and perpendicular directions to the epilayer plane, respectively. The perpendicular direction far-field pattern was calculated using a slab waveguide model [117], assuming the refractive index difference between GaN and $In_{0.1}Ga_{0.9}N$ to be 0.025. The calculation showed that the far-field full width at half maximum (FWHM) was about 15°, which is not far from the measured one (20°) considering the inaccuracy of refractive indices for each layer. This comparison strongly indicates that the emission is dominated by a few fundamental optical modes amplified by stimulated emission. If spontaneous emission were the dominant emission (i.e., all optical modes are equally excited), the far-field pattern would have been much broader, ideally approaching FWHM of 180°. The multi-lobed structure in the far-field for perpendicular direction as shown in Fig. 41 has also been observed elsewhere [118] and could be attributed to either excitation of optical modes other than the fundamental one or scattering of the laser beam due to imperfect laser facets [117]. The FWHM of the far-field in the parallel direction is much broader than the diffraction-limit (~ 0.1°), indicating non-uniform injection of current into the diodes, or filamentation in laser diodes. The issue of non-uniform current injection will be further discussed below.

The polarisation of the laser beam was measured as a function of injection current as shown in Fig. 42. The laser beam showed a strong anisotropy in polarisation, with intensity of TE modes being over 70 times higher than that of TM modes. Such a dominance of TE in stimulated emission is consistent with conventional QW laser gain theory [119], which predicts much higher transition matrix and gain for TE modes than TM counterparts [120]. Thus both the narrow far-field and the polarisation anisotropy is consistent with lasing operation of the lasers above threshold.

Figures 43 and 44 shown the dependence of threshold current density J_{th} on cavity length and temperature. As expected from the conventional laser theory [121], the threshold current density increases for short cavity lasers (Fig. 43). Transparency current density is estimated to be 150 A/cm^2 from the cavity length dependence of J_{th}. As shown in Fig. 44, T_o is about 145 K. This result is consistent with theoretical prediction [122] that T_o is ~ 2/3 T for ideal bulk lasers where thermal gain spectrum broadening is the primary reason for the increase in J_{th} with temperature. This also suggests that the temperature dependence of these lasers was primarily determined by thermal gain broadening and not strongly affected by non-radiative recombination or leakage current with increase in temperature.

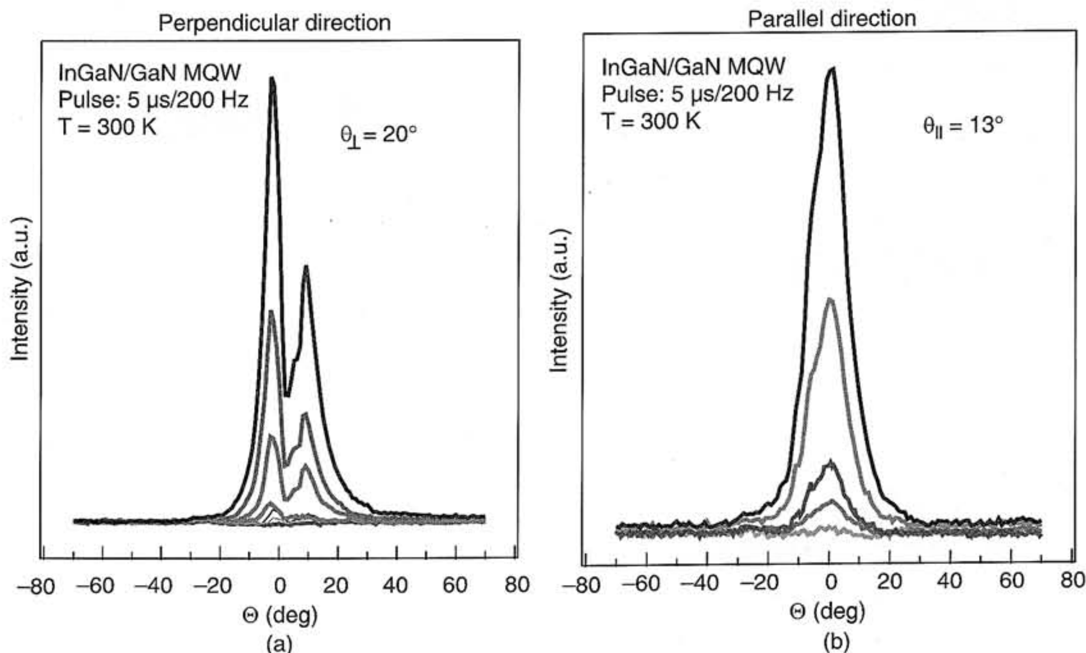

Fig. 41. Far-field in the perpendicular direction of a GaInN/GaN MQW laser diode at 300 K (a), far-field in the parallel direction of a GaInN/GaN MQW laser diode at 300 K (b).

 © 2000 COSiW SEP, Warsaw

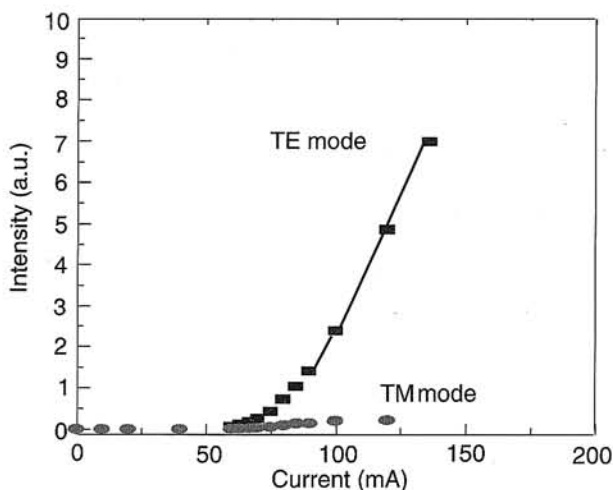

Fig. 42. Dependence of TE- and TM-polarised light intensities on injection current.

If it is assumed that the current is uniformly injected into the diodes, the threshold current (~ 300 mA) of our lasers with stripe area of 100×1200 μm [Fig. 38(b)] corresponds to threshold current density of 250 A/cm^2. This is about one order of magnitude lower than previous both experimental [118] and theoretical results [123,124]. Theoretically predicted values for threshold current density and threshold carrier density are around 1 ~ 2 kA/cm^2 and 1 ~ 2×10^{19} cm^{-3}, respectively [123,124], when using free-electron recombination and Kane's band model. Considering the high effective mass of conduction band electrons (~ 0.2 free electron mass [123,124]), this estimated apparent threshold current density is unlikely to be realistic. All of the measurements of optical power and current were performed in high-speed oscilloscope (400 MHz bandwidth) and no pulsation was observed. This excludes the possibility that the low threshold current may result from the self-pulsation, such as observed in other material systems [125]. It is believed that this low threshold current density may result from the fact that injection current could be non-uniformly distributed, and thus only a fraction of the diode contributes to the lasing operation. In this case, the threshold current density can be grossly overestimated. The non-uniform current distribution could be observed from near-field measurements performed for both LED and laser structures fabricated from the same GaInN/GaN MQW lasers. In these measurements, the near-field patterns of lasers with different aperture widths of 10 and 100 μm were compared. The 10-μm width lasers are expected to have less non-uniformity in current distribution compared to 100-μm width lasers. Figure 45 shows the characteristics of the 10-μm aperture devices. The devices were fabricated in the same manner as the 100-μm width devices except that the 10-μm metal stripes were deposited on the p-GaN cap layers while other parts were covered with a SiO_2 layer, as indicated in the upper right-hand corner of Fig. 45. The most noticeable difference between the P-I curves is that the 10-μm lasers have about 5–10 times higher J_{th}. This means that

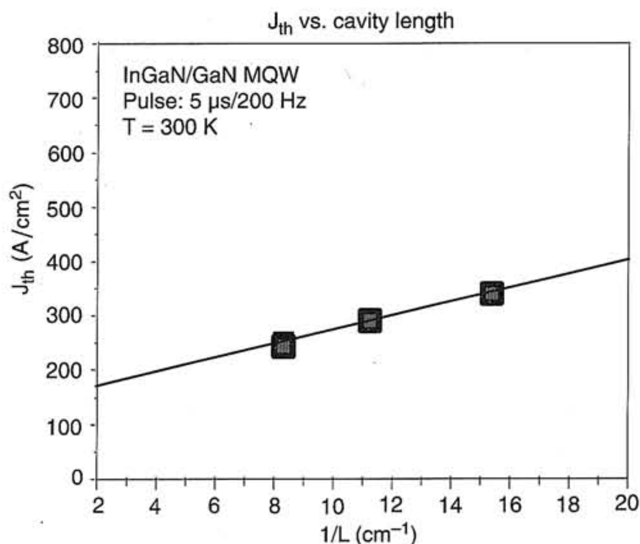

Fig. 43. Threshold current density vs. inverse cavity length of GaInN/GaN laser diodes (W = 100 μm aperture) at 300 K.

the narrow-aperture lasers have a more uniform current injection and consequently that a wider area of the device contributes to lasing than in 100-μm width devices. This observation was further supported by near-field imaging. As shown in Fig. 46, 100-μm width lasers showed strong narrow peak in the mirror, indicating the existence of filamentation resulting from laser instability. By contrast, 10-μm width devices showed a much more uniform near-field emission. For comparison, a LED showed a rather structure-less near-field spectrum without filamentation. Note that filamentation is one of the important characteristics of wide-aperture lasers, and is a good indication of the presence of stimulated emission.

The non-uniform distribution of injection current may result from, for example, indium composition or thickness

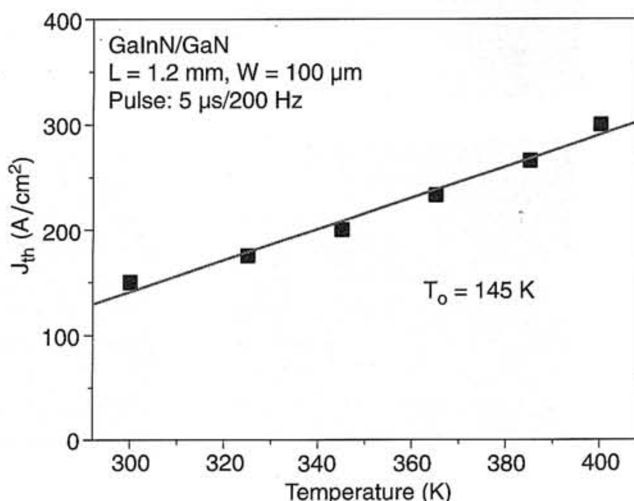

Fig. 44. Threshold current density vs. temperature of an GaInN/GaN MQW laser diode with To ~ 145 K from 300–400 K.

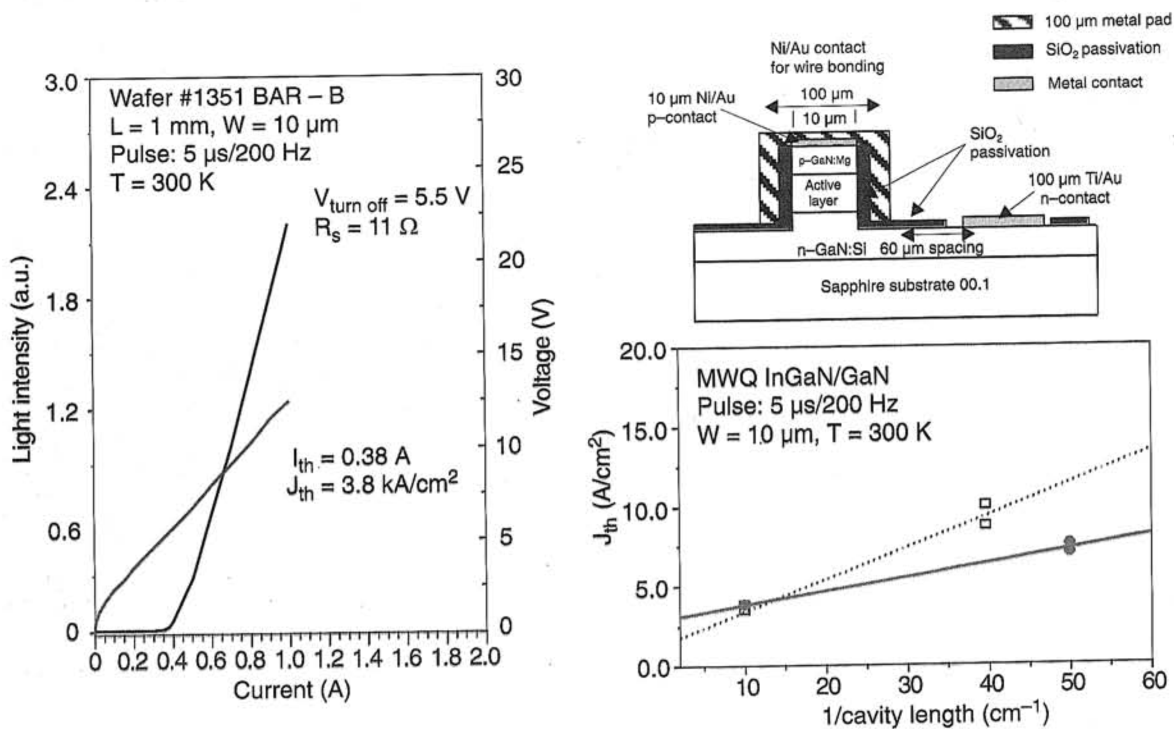

Fig. 45. Light – current (P-I) curve for 10-µm aperture width GaInN/GaN MQW laser under pulse operation at 300 K (L = 1000 µm), and the schematic diagram of the fabricated laser structure (upper right corner). In the bottom right corner, the dependence of J_{th} on cavity lengths for lasers from two wafers were shown.

fluctuations in the quantum wells, formation of quantum dots. These have also been attributed to anomalous emission spectra in other reports [118]. One source of non-uniformity can be explained from the near-field measurements performed for lasers with different contact positions. As shown in Fig. 47, lasers with n-metal contact on left (right) corner yielded a near-field emission much stronger on left (right) side. This indicates that the current does not spread well in the entire area of the lasers, which may be due to the relatively higher resistivity of the p-GaN.

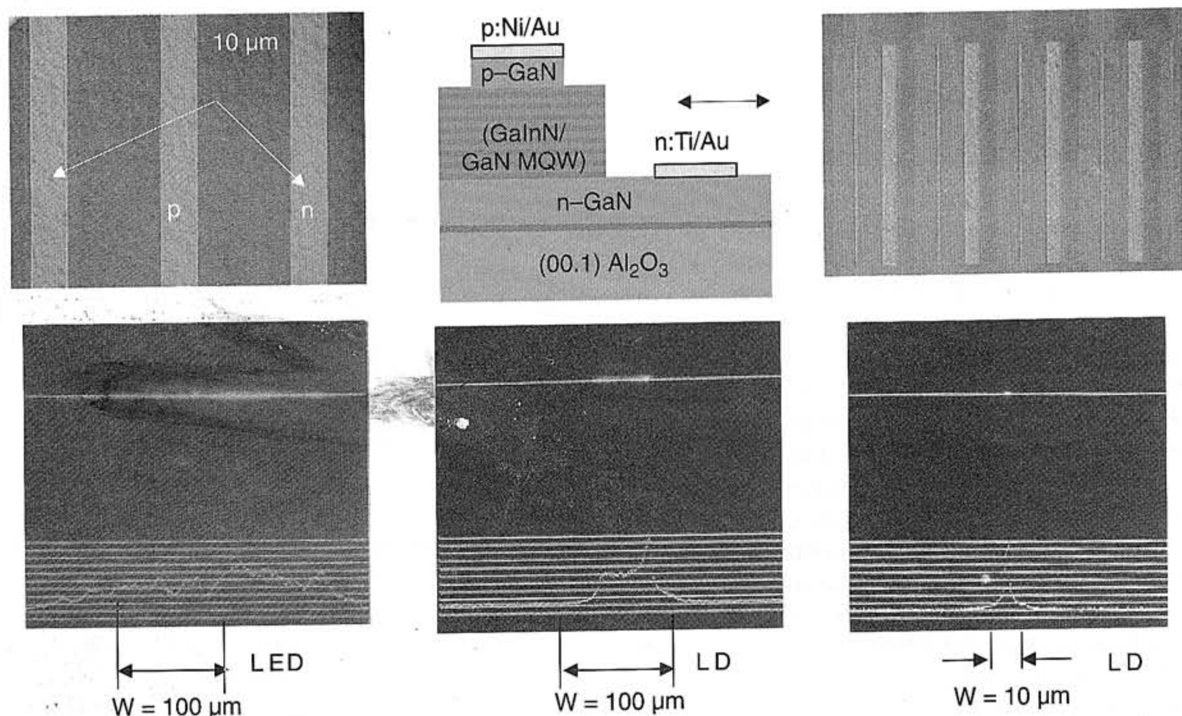

Fig. 46. Near-field patterns of LED, 100-µm aperture laser, and 10-µm aperture laser fabricated from a single wafer.

 © 2000 COSiW SEP, Warsaw

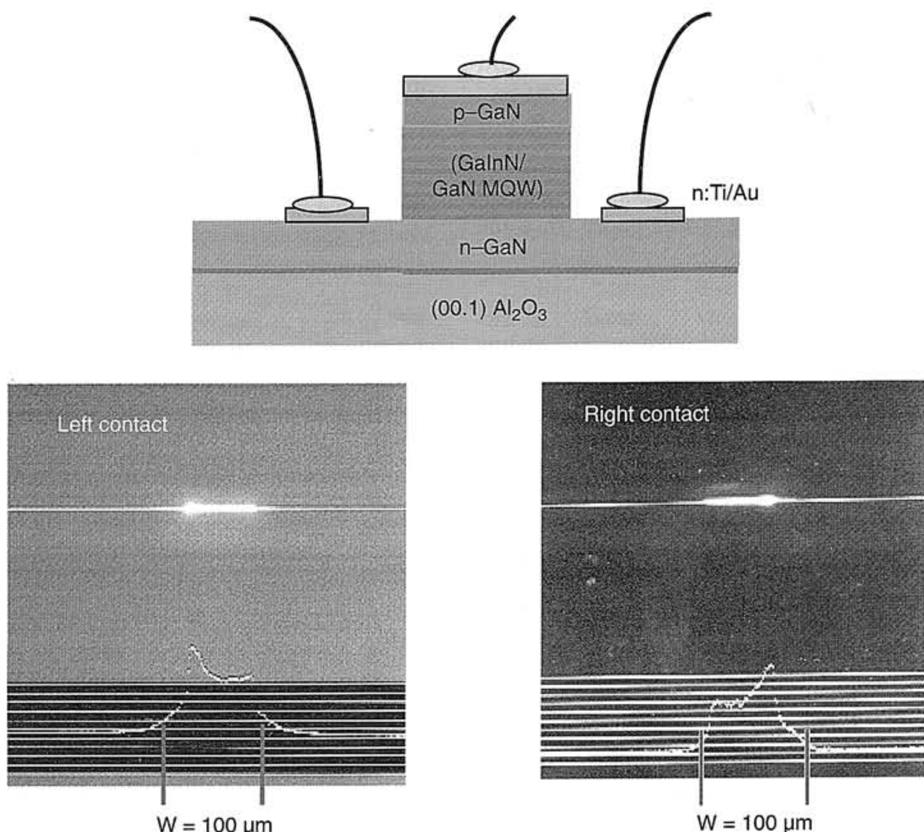

Fig. 47. Near-field patterns of 100-µm aperture lasers with different contact positions (one at left side and the other at right side).

A number devices were randomly selected, and subjected to lifetime testing in CW operation. Figure 48(a) shows the lifetime test results of one of the lasers at room temperature [the CW characteristics of the tested lasers are shown in Fig. 48(b)]. As shown in Fig. 48(a), no significant degradation of laser characteristics was observed for the whole lifetime test (140 hours).

10. Conclusion

This review has showed that indeed much has already been achieved in the III-Nitride material system over the past two decades, in particular the realisation of commercial optical devices. Much more fundamental work still needs to be conducted in order to understand the very rich and unex-

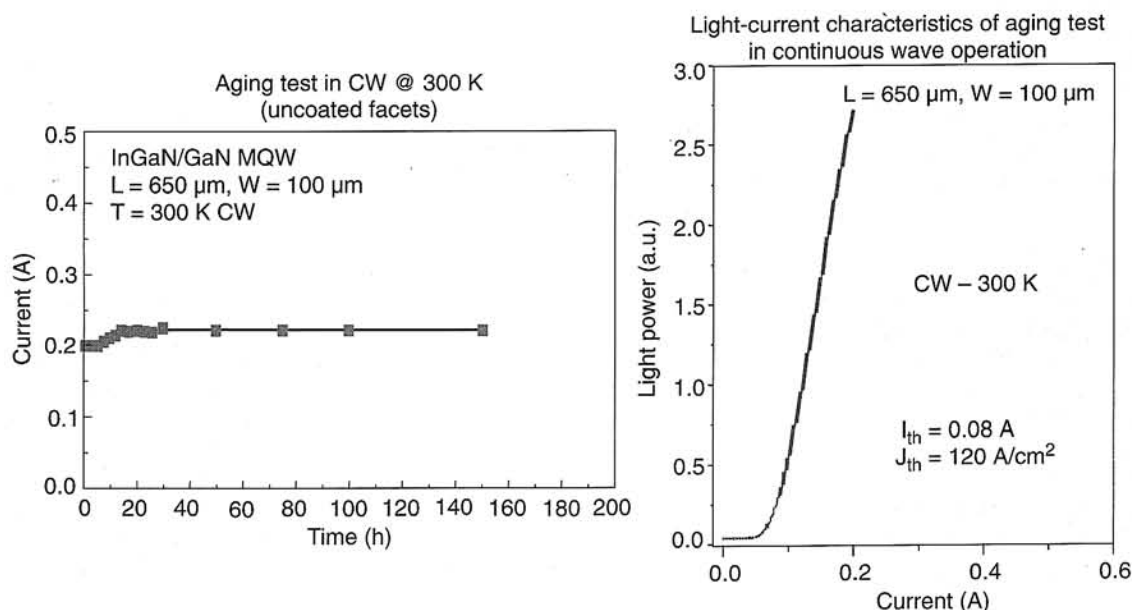

Fig. 48. Lifetime testing result of GaInN/GaN MQW laser diode (L = 650 µm, W = 100 µm) in continuous wave operation at 300 K (a), P-I curve of a tested laser at CW room temperature operation (b).

plored physical properties of III-Nitrides. A better understanding of all the physical parameters would allow in turn a better design of existing devices and the potential discovery of novel devices.

Note to the reader. There have been many developments in the various research areas outlined in this paper since the time of its submission.

References

1. F. Fichter and Z. Anorg, *Chem.* **54**, 332 (1971).
2. F. Fischer and F. Schröter, *Ber. Deutschen Chemischen Gesellschaft* **43**, 1465 (1910).
3. W.C. Johnson, J.B. Parsons, and M.C. Crew, "Nitrogen compounds of gallium III. Gallic nitride," *J. Phys. Chem.* **36**, 2561 (1932).
4. B. Daudin, J.L. Rouviere, and M. Arlery, "Polarity determination of GaN films by ion channeling and convergent beam electron diffraction," *Appl. Phys. Lett.* **69**, 2480 (1996).
5. A.D. Bykhovski, V.V. Kaminski, M.S. Shur, Q.C. Chen, and M.A. Khan, "Pyroelectricity in gallium nitride thin films," *Appl. Phys. Lett.* **69**, 3254 (1996).
6. J. Miragliotta, D.K. Wickenden, T.J. Kistenmacher, and W.A. Bryden, "Linear and nonlinear optical properties of GaN thin films," *J. Opt. Soc. Am.* B **10,** 1447 (1993).
7. H.Y. Zhang, X.H. He, Y.H. Shih, M. Schurman, Z.C. Feng, and R.A. Stall, "Study of nonlinear optical effects in GaN:Mg epitaxial film," *Appl. Phys. Lett.* **69**, 2953 (1996).
8. *Semiconductors: group IV elements and III-V compounds*, edited by O. Madelung, Springer-Verlag, Berlin, 1991.
9. O. Madelung, *Semiconductors – Basic Data*, 2nd edition, Springer-Verlag, Berlin, 1996.
10. M. Leszczynski, T. Suski, P. Perlin, H. Teisseyre, I. Grzegory, M. Bockowski, J. Jun, S. Porowski, and J. Major, "Lattice constants, thermal expansion and compressibility of gallium nitride," *J. Phys.* D **28**, A149 (1995).
11. M. Razeghi and A. Rogalski, "Semiconductor ultraviolet detectors," *J. Appl. Phys.* **79**, 7433 (1996).
12. P. Kung, A. Saxler, X. Zhang, D. Walker, and M. Razeghi, "GaN, GaAlN, and AlN for use in UV detectors for astrophysics: an update," *Proc. SPIE* **2685**, 126 (1996).
13. P. Kung, A. Saxler, X. Zhang, D. Walker, R. Lavado, and M. Razeghi, "Metalorganic chemical vapour deposition of monocrystalline GaN thin films on β-$LiGaO_2$ substrates," *Appl. Phys. Lett.* **69**, 2116 (1996).
14. H. Ohsato and M. Razeghi, "Growth models of GaN thin films based on crystal chemistry: Hexagonal and cubic GaN on Si substrates," *Proc. SPIE* **2999**, 288 (1997).
15. S. Porowski, "High, pressure growth of GaN – new prospects for blue lasers," *J. Cryst. Growth* **166**, 583 (1996).
16. C.J. Sun, P. Kung, A. Saxler, H. Ohsato, K. Haritos, and M. Razeghi, "A crystallographic model of (00·1) aluminium nitride epitaxial film grown on (00·1) sapphire substrate," *J. Appl. Phys.* **75**, 3964 (1994).
17. P. Kung, C.J. Sun, A. Saxler, H. Ohsato, and M. Razeghi, "Crystallography of epitaxial growth of wurtzite-type thin films on sapphire substrates," *J. Appl. Phys.* **75**, 4515 (1994).
18. T. Kato, P. Kung, A. Saxler, C.J. Sun, H. Ohsato, M. Razeghi, and T. Okuda, "Morphology of twinned GaN grown on (11.0) sapphire substrates," *Solid-State Electronics* **41**, 227 (1997).
19. T. Kato, H. Ohsato, T. Okuda, P. Kung, A. Saxler, C.J. Sun, and M. Razeghi, "Simultaneous growth of two different oriented GaN epilayers on (11.0) sapphire, I. Morphology and orientation," *J. Cryst. Growth* **173**, 244 (1997).
20. T. Kato, P. Kung, A. Saxler, C.J. Sun, H. Ohsato, M. Razeghi, and T. Okuda, "Simultaneous growth of two differently oriented GaN epilayers on (11.0) sapphire, II. A growth model of (00.1) and (10.0) GaN," *J. Cryst. Growth* **183**, 131 (1998).
21. C.J. Sun and M. Razeghi, "Comparison of the physical properties of GaN thin films deposited on (00·1) and (01·2) sapphire substrates," *Appl. Phys. Lett.* **63**, 973 (1993).
22. H. Amano, N. Sawaki, I. Akasaki, and Y. Toyoda, "Metalorganic vapor phase epitaxial growth of a high quality GaN film using an AlN buffer layer," *Appl. Phys. Lett.* **48**, 353 (1986).
23. L.T. Romano, B.S. Krusor, and R.J. Molnar, "Structure of GaN films grown by hydride vapour phase epitaxy," *Appl. Phys. Lett.* **71**, 2283 (1997).
24. A. Saxler, D. Walker, P. Kung, X. Zhang, M. Razeghi, J. Solomon, W.C. Mitchel, and H.R. Vydyanath, "Comparison of trimethylgallium and triethylgallium for the growth of GaN," *Appl. Phys. Lett.* **71**, 3272 (1997).
25. A. Beaumont, P. Gibart, and J.P. Faurie, "Nitrogen precursors in metalorganic vapour phase epitaxy of (Al,Ga)N," *J. Cryst. Growth* **156**, 140 (1995).
26. A. Saxler, P. Kung, C.J. Sun, E. Bigan, and M. Razeghi, "High quality aluminum nitride epitaxial layers grown on sapphire substrates," *Appl. Phys. Lett.* **64**, 339 (1994).
27. P. Kung, A. Saxler, X. Zhang, D. Walker, T.C. Wang, I. Ferguson, and M. Razeghi, "High quality AlN and GaN epilayers grown on (00·1) sapphire, (100) and (111) silicon substrates," *Appl. Phys. Lett.* **66**, 2958 (1995).
28. M.C. Benjamin, C. Wang, R.F. Davis, and R.J. Nemanich, "Observation of a negative electron affinity for heteroepitaxial AlN on (6H)-SiC (0001)," *Appl. Phys. Lett.* **64**, 3288 (1994).
29. A.T. Sowers, J.A. Christman, M.D. Bremser, B.L. Ward, R.F. Davis, and R.J. Nemanich, "Thin films of aluminium nitride and aluminium gallium nitride for cold cathode applications," *Appl. Phys. Lett.* **71**, 2289 (1997).
30. K. Kaya, H. Takahashi, Y. Shibata, Y. Kanno, and T. Hirai, "Experimental surface acoustic wave properties of AlN thin films on sapphire substrates," *Jpn. J. Appl. Phys.* **36**, 307 (1997).
31. C.J. Sun, P. Kung, A. Saxler, H. Ohsato, E. Bigan, M. Razeghi, and D.K. Gaskill, "Thermal stability of GaN thin films grown on (00·1) Al_2O_3, (01·2) Al_2O_3 and (00·1)Si 6H-SiC substrates", *J. Appl. Phys.* **76**, 236 (1994).
32. P. Kung, A. Saxler, D. Walker, X. Zhang, R. Lavado, K.S. Kim, and M. Razeghi, "$Al_xGa_{1-x}N$ based materials and heterostructures," in *III-V Nitrides,* Vol. 449, p. 79, edited by F.A. Ponce, T.D. Moustakas, I. Akasaki, and B.A. Monemar, Materials Research Society Symposium Proceedings, Pittsburgh: Materials Research Society, 1997.
33. M. Razeghi, unpublished.
34. J.M. Redwing, M.A. Tischler, J.S. Flynn, S. Elhamri, M. Ahoujja, R.S. Newrock, and W.C. Mitchel, "Two-dimensional electron gas properties of AlGaN/GaN

 © 2000 COSiW SEP, Warsaw

heterostructures grown on 6H-SiC and sapphire substrates," *Appl. Phys. Lett.* **69**, 963 (1996).
35. M. Shur, B. Gelmont, and M.A. Khan, "Electron mobility in two-dimensional electron gas in AlGaN/GaN heterostructures and in bulk GaN," *J. Electron. Mater.* **25**, 777 (1996).
36. E.T. Yu, G.J. Sullivan, P.M. Asbeck, C.D. Wang, D. Qiao, and S.S. Lau, "Measurement of piezoelectrically induced charge in GaN/AlGaN heterostructure field-effect transistors," *Appl. Phys. Lett.* **71**, 2794 (1997).
37. G. Martin, A. Botchkarev, A. Rockett, and H. Morkoç, "Valence-band discontinuities of wurtzite GaN, AlN, and InN heterojunctions measured by X-ray photoemission spectroscopy," *Appl Phys. Lett.* **68**, 2541 (1996).
38. A. Koukitu, N. Takahashi, T. Taki, and H. Seki, "Thermodynamic analysis of the MOVPE growth of $In_xGa_{1-x}N$," *J. Cryst. Growth* **170**, 306 (1997).
39. I.H. Ho and G.B. Stringfellow, "Solid phase immiscibility in GaInN," *Appl. Phys. Lett.* **69**, 2701 (1996).
40. S. Nakamura and T. Mukai, "High-quality InGaN films grown on GaN films," *Jpn. J. Appl. Phys.* **31**, L1457 (1992).
41. A. Sohmer, J. Off, H. Bolay, V. Härle, V. Syganow, J.S. Im, V. Wagner, F. Adler, A. Hangleiter, A. Dörnen, F. Scholz, D. Brunner, O. Ambacher, and H. Lakner, "GaInN/GaN-heterostructures and quantum wells grown by metalorganic vapour-phase epitaxy," *MRS Internet Journal Nitride Semiconductor Research* **2**, 14 (1997).
42. P. Kung, A. Saxler, D. Walker, A. Rybaltowski, X. Zhang, J. Diaz, and M. Razeghi, "GaInN/ GaN multi-quantum well laser diodes grown by low-pressure metalorganic chemical vapour deposition," *MRS Internet Journal Nitride Semiconductor Research* **3**, 1 (1998).
43. M. Koike, S. Yamasaki, S. Nagai, N. Koide, S. Asami, H. Amano, and I. Akasaki, "High-quality GaInN/GaN multiple quantum wells," *Appl. Phys. Lett.* **68**, 1403 (1996).
44. K. Hiramatsu, Y. Kawaguchi, M. Shimizu, N. Sawaki, T. Zheleva, R.F. Davis, H. Tsuda, W. Taki, N. Kuwano, and K. Oki, "The composition pulling effect in MOVPE grown InGaN on GaN and AlGaN and its TEM characterisation," *MRS Internet Journal Nitride Semiconductor Research* **2**, 6 (1997).
45. T. Deguchi, A. Shikanai, K. Torii, T. Sota, S. Chichibu, and S. Nakamura, "Luminescence spectra from InGaN multiquantum wells heavily doped with Si," *Appl. Phys. Lett.* **72**, 3329 (1998).
46. X. Zhang, P. Kung, A. Saxler, D. Walker, and M. Razeghi, "Observation of room temperature surface-emitting stimulated emission from GaN:Ge by optical pumping," *J. Appl. Phys.* **80**, 6544 (1996).
47. A. Saxler, P. Kung, X. Zhang, D. Walker, J. Solomon, M. Ahoujja, W.C. Mitchel, H.R. Vydyanath, and M. Razeghi, "GaN doped with sulfur," in *Defects in Semiconductors ICDS-19*, Vols. 258-263, p. 1161, edited by G. Davies and M.H. Nazaré, Materials Science Forum, Trans Tech Publications, Switzerland, 1998.
48. W. Gotz, N.M. Johnson, C. Chen, H. Liu, C. Kuo, and W. Imler, "Activation energies of Si donors in GaN," *Appl. Phys. Lett.* **68**, 3144 (1996).
49. X. Zhang, P. Kung, A. Saxler, D. Walker, T.C. Wang, and M. Razeghi, "Growth of $Al_xGa_{1-x}N$:Ge on sapphire and silicon substrates," *Appl. Phys. Lett.* **67**, 1745 (1995).
50. S. Nakamura, T. Mukai, and M. Senoh, "Si-doped InGaN films grown on GaN films," *Jpn. J. Appl. Phys.* **32**, L16 (1993).
51. K. Wongchotique, N. Chen, D.P. Zhang, X. Tang, and M.G. Spencer, "Low resistivity aluminium nitride: carbon (AlN:C) films grown by metal organic chemical vapour deposition," in *Gallium Nitride and Related Materials*, Vol. 395, p. 279, edited by F.A. Ponce, R.D. Dupuis, S. Nakamura, and J.A. Edmond, Materials Research Society Symposium Proceedings, Materials Research Society, Pittsburgh, 1996.
52. S. Nakamura, T. Mukai, M. Senoh, and N. Iwasa, "Thermal annealing effects on p-type Mg-doped GaN Films," *Jpn. J. Appl. Phys.* **31**, L139 (1992).
53. H. Amano, M. Kito, K. Hiramatsu, and I. Akasaki, "P-type conduction in Mg-doped GaN treated with low-energy electron beam irradiation (LEEBI)," *Jpn. J. Appl. Phys.* **28**, L2112 (1989).
54. S. Nakamura, N. Iwasa, M. Senoh, and T. Mukai, "Hole compensation mechanism of p-type GaN films," *Jpn. J. Appl. Phys.* **31**, 1258 (1992).
55. S. Yamasaki, S. Asami, N. Shibata, M. Koike, K. Manabe, T. Tanaka, H. Amano, and I. Akasaki, "P-type conduction in Mg-doped $Ga_{0.91}In_{0.09}N$ grown by metalorganic vapour-phase epitaxy," *Appl Phys. Lett.* **66**, (1995) 1112.
56. O. Brandt, H. Yang, H. Kostial, and K.H. Ploog, "High p-type conductivity in cubic GaN/GaAs (113)A by using Be as the acceptor and O as the codopant," *Appl. Phys. Lett.* **69** (1996) 2707.
57. A. Saxler, M.A. Capano, W.C.. Mitchel, P. Kung, X. Zhang, D. Walker, and M. Razeghi, "High resolution x-ray diffraction of GaN grown on sapphire substrates," in *III-V Nitrides*, Vol. 449, p. 477, edited by F.A. Ponce, T.D. Moustakas, I. Akasaki, and B.A. Monemar, Materials Research Society Symposium Proceedings, Materials Research Society, Pittsburgh, 1997.
58. K. Dovidenko, S. Oktyabrsky, J. Narayan, and M. Razeghi, "Aluminium nitride films on different orientations of sapphire and silicon," *J. Appl. Phys.* **79**, 2439 (1996).
59. X.H. Wu, L.M. Brown, D. Kapolnek, S. Keller, B. Keller, S.P. DenBaars, and J.S. Speck, "Defect structure of metal-organic chemical vapour deposition-grown epitaxial (0001) GaN/Al_2O_3," *J. Appl. Phys.* **80**, 3228 (1996).
60. Y. Chen, T. Takeuchi, H. Amano, I. Akasaki, N. Yamada, Y. Kaneko, and S.Y. Wang, "Pit formation in GaInN quantum wells," *Appl. Phys. Lett.* **72**, 710 (1998).
61. X. Zhang, P. Kung, A. Saxler, D. Walker, and M. Razeghi, "Growth of GaN without yellow photoluminescence," in *Gallium Nitride and Related Materials*, Vol. 395, p. 625, edited by F.A. Ponce, R.D. Dupuis, S. Nakamura and J.A. Edmond, Materials Research Society Symposium Proceedings, Materials Research Society, Pittsburgh, 1996.
62. F.A. Ponce, D.P. Bour, W. Gotz, and P.J. Wright, "Spatial distribution of the luminescence in GaN thin films," *Appl .Phys. Lett.* **68**, 57 (1996).
63. F.E. Ejeckam, M. Seaford, Y.H. Lo, H.Q. Hou, and B.E. Hammons, "Dislocation-free InSb grown on GaAs compliant universal substrates," *Appl. Phys. Lett.* **71**, 776 (1997).
64. O.H. Nam, M.D. Bremser, T.S. Zheleva, and R.F. Davis, "Lateral epitaxy of low defect density GaN layers via organometallic vapor phase epitaxy," *Appl. Phys. Lett.* **71**, 2638 (1997).

65. P. Kung, X. Zhang, A. Saxler, D. Walker, M. Razeghi, W. Qian, and V.P. Dravid, "MOCVD growth of high quality GaN-AlGaN based structures on Al_2O_3 substrates with dislocation density less than 10^7 cm^{-2}," *J. European Ceramic Society* **17**, 1781 (1997).
66. S. Nakamura, M. Senoh, S. Nagahama, N. Iwasa, T. Yamada, T. Matsushita, H. Kiyoku, Y. Sugimoto, T. Kozaki, H. Umemoto, M. Sano, and K. Chocho, "InGaN/GaN/AlGaN-based laser diodes with modulation-doped strained-layer superlattices grown on an epitaxially laterally overgrown GaN substrate," *Appl. Phys. Lett.* **72**, 211 (1998).
67. P. Kung, D. Walker, M. Hamilton, J. Diaz, and M. Razeghi, "Lateral epitaxial overgrowth of GaN films on sapphire and silicon substrates," *Appl. Phys. Lett.*, **74**, 570 (1999).
68. A. Saxler, *Exploration of LP-MOCVD Grown III-Nitrides on Various Substrates,* Ph.D. dissertation, Northwestern University, 1998.
69. D. Kapolnek, S. Keller, R. Vetury, R.D. Underwood, P. Kozodoy, S.P. DenBaars, and U.K. Mishra, "Anisotropic epitaxial lateral growth in GaN selective area epitaxy," *Appl. Phys. Lett.* **71**, 1204 (1997).
70. M.E. Lin, B. Sverdlov, G.L. Zhou, and H. Morkoç, "A comparative study of GaN epilayers grown on sapphire and SiC substrates by plasma-assisted molecular-beam epitaxy," *Appl. Phys. Lett.* **62**, 3479 (1993).
71. C. Youtsey, I. Adesida, L.T. Romano, and G. Bulman, "Smooth n-type GaN surfaces by photoenhanced wet etching," *Appl. Phys. Lett.* **72**, 560 (1998).
72. C.B. Vartuli, J.D. MacKenzie, J.W. Lee, C.R. Abernathy, S.J. Pearton, and R.J. Shul, "Cl_2/Ar and CH_4/H_2/Ar dry etching of III-V nitrides," *J. Appl. Phys.* **80**, 3705 (1996).
73. R.J. Shul, C.I.H. Ashby, C.G. Willison, L. Zhang, J. Han, M.M. Bridges, S.J. Pearton, J.W. Lee, and L.F. Lester, "GaN etching in BCl_3/Cl_2 plasmas," in *Wide-Bandgap Semiconductors for High Power, High Frequency and High Temperature,* edited by S. DenBaars, M.S. Shur, J. Palmour, and M. Spencer, Vol. 512, p. 449, Materials Research Society Proceedings, Materials Research Society, Pittsburgh, 1998.
74. M. Razeghi, unpublished.
75. F. Binet, J.Y. Duboz, N. Laurent, C. Bonnat, P. Collot, F. Hanauer, O. Briot, and R.L. Aulomnard, "Realisation and optical characterisation of etched mirror facets in GaN cavities," *Appl. Phys. Lett.* **72**, 960 (1998).
76. B.P. Luther, S.E. Mohney, T.N. Jackson, M.A. Khan, Q. Chen, and J.W. Yang, "Investigation of the mechanism for ohmic contact formation in Al and Ti/Al contacts to n-type GaN," *Appl. Phys. Lett.* **70**, 57 (1997).
77. Z. Fan, S.N. Mohammad, W. Kim, O. Aktas, A.E. Botchkarev, and H. Morkoç, "Very low resistance multilayer ohmic contact to n-GaN," *Appl. Phys. Lett.* **68**, 1672 (1996).
78. C.T. Lee, M.Y. Yeh, C.D. Tsai, and Y.T. Lyu, "Low resistance bilayer Nd/Al ohmic contacts on n-type GaN," *J. Electron. Mater.* **26**, 262 (1997).
79. Y.F. Wu, W.N. Jiang, B.P. Keller, S. Keller, D. Kapolnek, S.P. DenBaars, U.K. Mishra, and B. Wilson, "Low resistance ohmic contact to n-GaN with a separate layer method," *Solid State Electron.* **41**, 165 (1997).
80. T. Ping, M.A. Khan, and I. Adesida, "Ohmic contacts to n-type GaN using Pd/Al metallisation," *J. Electron. Mater.* **25**, 819 (1996).
81. H. Ishikawa, S. Kobayashi, Y. Koide, S. Yamasaki, S. Nagai, J. Umezaki, M. Koike, and M. Murakami, "Effects of surface treatments and metal work functions on electrical properties at p-GaN/metal interfaces," *J. Appl. Phys.* **81**, 1315 (1997).
82. E.V. Kalinina, N.I. Kuznetsov, V.A. Dmitriev, K.G. Irvine, and C.H. Carter, "Schottky barriers on n-GaN grown on SiC," *J. Electron. Mater.* **25**, 831 (1996).
83. T.U. Kampen and W. Mönch, "Metal contacts on α-GaN", *MRS Internet J.* **1**, 41 (1997).
84. X. Zhang, D. Walker, A. Saxler, P. Kung, J. Xu, and M. Razeghi, "Observation of inversion layers at AlN-Si interfaces fabricated by metal organic chemical vapour deposition," *Electron. Lett.* **32**, 1622 (1996).
85. D. Walker, X. Zhang, P. Kung, A. Saxler, S. Javadpour, J. Xu, and M. Razeghi, "AlGaN ultraviolet photoconductors grown on sapphire," *Appl. Phys. Lett.* **68**, 2100 (1996).
86. D. Walker, X. Zhang, A. Saxler, P. Kung, J. Xu, and M. Razeghi, "$Al_xGa_{1-x}N$ ($0<x<1$) ultraviolet photodetectors grown on sapphire by metal-organic chemical-vapor deposition," *Appl. Phys. Lett.* **70**, 949 (1997).
87. J.C. Carrano, P.A. Grudowski, C.J. Eiting, R.D. Dupuis, and J.C. Campbell, "Very low dark current metal-semiconductor-metal ultraviolet photodetectors fabricated on single-crystal GaN epitaxial layers," *Appl. Phys. Lett.* **70**, 1992 (1997).
88. Z.C. Huang, D.B. Mott, P.K. Shu, J.C. Chen, and D.K. Wickenden, "Improvements of metal-semiconductor-metal GaN photoconductors," *J. Electron. Mater.* **26**, 30 (1997).
89. Q. Chen, J.W. Yang, A. Osinsky, S. Gangopadhyay, B. Lim, M. Lim, A. Anwar, M. Asif Khan, D. Kuksenkov, and H. Temkin, "Schottky barrier detectors on GaN for visible-blind ultraviolet detection," *Appl. Phys. Lett.* **70**, 2277 (1997).
90. A. Osinsky, S. Gangopadhyay, J.W. Yang, R. Gaska, D. Kuksenkov, H. Temkin, I.K. Shmagin, Y.C. Chang, J.F. Muth, and R.M. Kolbas, "Visible-blind GaN Schottky barrier detectors grown on Si(111)," *Appl. Phys. Lett.* **72**, 551 (1998).
91. J.M. Van Hove, R. Hickman, J.J. Klaassen, P.P. Chow, and P.P. Ruden, "Ultraviolet-sensitive, visible-blind GaN photodiodes fabricated by molecular beam epitaxy," *Appl. Phys. Lett.* **70**, 2282 (1997).
92. A. Osinsky, S. Gangopadhyay, R. Gaska, B. Williams, M.A. Khan, D. Kuksenkov, and H. Temkin, "Low noise p-i-n GaN ultraviolet photodetectors," *Appl. Phys. Lett.* **71**, 2334 (1997).
93. G.Y. Xu, A. Salvador, W. Kim, Z. Fan, C. Lu, H. Tang, H. Morkoç, G. Smith, M. Estes, B. Goldenberg, W. Yang, and S. Krishnankutty, "High speed, low noise ultraviolet photodetectors based on GaN p-i-n and AlGaN(p)-GaN(i)-GaN(n) structures," *Appl. Phys. Lett.* **71**, 2154 (1997).
94. D. Walker, A. Saxler, P. Kung, X. Zhang, M. Hamilton, J. Diaz, and M. Razeghi, "Visible blind GaN p-i-n photodiodes," *Appl. Phys. Lett.* **72**, 3303 (1998).
95. P. Kung, X. Zhang, D. Walker, A. Saxler, J. Piotrowski, A. Rogalski, and M. Razeghi, "Kinetics of photoconductivity in n-type GaN photodetector," *Appl. Phys. Lett.* **67**, 3792 (1995).
96. D. Walker, E. Monroy, P. Kung, J. Wu, M. Hamilton, F.J. Sanchez, J. Diaz, and M. Razeghi, "High speed, low-noise metal-semiconductor-metal ultraviolet photodetectors based on GaN," *Appl. Phys. Lett.*, **74**, 762 (1999).

 © 2000 COSiW SEP, Warsaw

97. X. Zhang, P. Kung, D. Walker, J. Piotrowski, A. Rogalski, A. Saxler, and M. Razeghi, "Photovoltaic effects in GaN structures with p-n junction," *Appl. Phys. Lett.* **67**, 2028 (1995).
98. E. Monroy, M. Hamilton, D. Walker, P. Kung, F.J. Sanchez, and M. Razeghi, "High-quality visible-blind AlGaN p-i-n photodiodes, " *Appl. Phys. Lett.*, 74, 1171 (1999).
99. D.W. Jenkins, J.D. Dow, and M.H. Tsai, "N vacancies in $Al_xGa_{1-x}N$," *J. Appl. Phys.* **72**, 4130 (1992).
100. A. Rogalski, *Infrared Photon Detector*, SPIE Optical Engineering Press, Bellingham, 1995.
101. A. Saxler, K.S. Kim, D. Walker, P. Kung, X. Zhang, G. Brown, W.C. Mitchel, and M. Razeghi, "Electroluminescence of III-Nitride double heterostructure light emitting diodes with silicon and magnesium doped InGaN," in *Defects in Semiconductors ICDS-19*, Vols. 258-263, p. 1229, edited by G. Davies and M.H. Nazaré, Materials Science Forum, Trans Tech Publications, Switzerland, 1998.
102. S. Nakamura, M. Senoh, N. Iwasa, and S. Nagahama, "High-power InGaN single-quantum-well-structure blue and violet light-emitting diodes," *Appl. Phys. Lett.* **67**, 1868 (1995).
103. S. Nakamura, M. Senoh, N. Iwasa, and S. Nagahama, "High-brightness InGaN blue, green and yellow light-emitting diodes with quantum well structures," *Jpn. J. Appl. Phys.* **34**, L797 (1995).
104. S. Nakamura, M. Senoh, N. Iwasa, S. Nagahama, T. Yamada, and T. Mukai, "Superbright green InGaN single-quantum-well-structure light-emitting diodes," *Jpn. J. Appl. Phys.* **34** L1332 (1995).
105. G. Fasol, oral presentation in ATIP (Asian Technology Information Programme)-seminar, Tokyo, Japan, 1995.
106. Q. Guo, O. Kato, and A. Yoshida, "Thermal stability of indium nitride single crystal films," *J. Appl. Phys.* **73**, 7969 (1993).
107. S. Nakamura, M. Senoh, S. Nagahama, N. Iwasa, T. Yamada, T. Matsushita, Y. Sugimoto, and H. Kiyoku, "Longitudinal mode spectra and ultrashort pulse generation of InGaN multiquantum well structure laser diodes," *Appl. Phys. Lett.* **70**, 616 (1996).
108. S. Nakamura, M. Senoh, S. Nagahama, N. Iwasa, T. Yamada, T. Matsushita, H. Kiyoku, and Y. Sugimoto, "Room-temperature continuous-wave operation of InGaN multi-quantum-well structure laser diodes with a lifetime of 27 hours," *Appl. Phys. Lett.* **70**, 1417 (1996).
109. S. Nakamura, M. Senoh, .S. Nagahama, N. Iwasa, T. Yamada, T. Matsushita, Y. Sugimoto, and H. Kiyoku, "Subband emissions of InGaN multi-quantum-well laser diodes under room-temperature continuous wave operation," *Appl. Phys. Lett.* **70**, 2753 (1997).
110. S. Chichibu, K. Wada, and S. Nakamura, "Spatially resolved cathodoluminescence spectra of InGaN quantum wells," *Appl. Phys. Lett.* **71**, 2346 (1997).
111. Y. Narukawa, Y. Kawakami, M. Funato, S. Fujita, S. Fujita, and S. Nakamura, "Role of self-formed InGaN quantum dots for exciton localisation in the purple laser diode emitting at 420 nm," *Appl. Phys. Lett.* **70**, 981 (1997).
112. Y.K. Song, M. Kuball, A.V. Nurmikko, G.E. Bulman, K. Doverspike, S.T. Sheppard, T.W. Weeks, M. Leonard, H.S. Kong, H. Dieringer, and J. Edmond, "Gain characteristics of InGaN/GaN quantum well diode lasers," *Appl. Phys. Lett.* **72**, 1418 (1998).
113. T. Deguchi, A. Shikanai, K. Torii, T. Sota, S. Chichibu, and S. Nakamura, "Luminescence spectra from InGaN multiquantum wells heavily doped with Si," *Appl. Phys. Lett.* **72**, 3329 (1998).
114. D.A. Cohen, T. Margalith, A.C. Abare, M.P. Mack, L.A. Coldren, S.P. DenBaars, and D.R. Clarke, "Catastrophic optical damage in GaInN multiple quantum wells," *Appl. Phys. Lett.* **72**, 3267 (1998).
115. S. Nakamura, M. Senoh, S. Nagahama, N. Iwasa, T. Yamada, T. Matsushita, H. Kiyoku, Y. Sugimoto, T. Kozaki, H. Umemoto, M. Sano, and K. Chocho, "Continuous-wave operation of InGaN/ GaN/AlGaN-based laser diodes grown on GaN substrates," *Appl. Phys. Lett.* **72**, 2014 (1998).
116. H. Nakayama, P. Hacke, M.R.H. Khan, T. Detchprohm, K. Hiramatsu, and N. Sawaki, "Electrical transport properties of p-GaN," *Jap. J. Appl. Phys.* **35**, L282 (1996).
117. H. Yi, A. Rybaltowski, J. Diaz, D. Wu, B. Lane, Y. Xiao, and M. Razeghi, "Stability of far fields in double heterostructure and multiple quantum well InAsSb/InPAsSb/InAs midinfrared lasers," *Appl. Phys. Lett.* **70**, 3236 (1997).
118. S. Nakamura and G. Fasol, *The Blue Laser Diode*, Springer-Verlag, Berlin, 1997.
119. D. Ahn, S.L. Chuang, and Y.C. Chang, "Valence-band mixing effects on the gain and refractive index change of quantum-well lasers," *J. Appl. Phys.* **64**, 4056 (1988).
120. Polarisation anisotropy would be observed even for spontaneous emission because of higher transition matrix in QW structure. However, the difference should be less than a factor of 3 (Ref. 119).
121. H. Casey and M.B. Panish, *Heterostructure Laser*, Academic Press, New York, 1978.
122. M. Razeghi, H. Yi, and V. Litvinov (unpublished).
123. M. Suzuki and T. Uenoyama, "Biaxial strain effect on wurtzite GaN/AlGaN quantum well lasers," *Jpn. J. Appl. Phys.* **35**, 1420 (1996).
124. P. Rees, C. Cooper, P. Smowton, P. Blood, and J. Hegarty, "Calculated threshold currents of nitride- and phosphide-based quantum-well lasers," *IEEE Photon. Technol. Lett.* **8**, 197 (1996).
125. K.D. Choquette, H. Hou, K. Lear, H. Chui, K. Geib, A. Mar, and B. Hammons, "Self-pulsing oxide-confined vertical cavity lasers with ultralow operating current," *Electron. Lett.* **32**, 459 (1996).